

Louisiana Tech University

## Louisiana Tech Digital Commons

---

Doctoral Dissertations

Graduate School

---

Fall 11-17-2018

### Electromagnetic Wave-Matter Interactions in Complex Opto-Electronic Materials and Devices

Raj Kumar Vinnakota  
*Louisiana Tech University*

Follow this and additional works at: <https://digitalcommons.latech.edu/dissertations>



Part of the [Electromagnetics and Photonics Commons](#), [Engineering Physics Commons](#), [Other Physical Sciences and Mathematics Commons](#), and the [Other Physics Commons](#)

---

#### Recommended Citation

Vinnakota, Raj Kumar, "" (2018). *Dissertation*. 15.  
<https://digitalcommons.latech.edu/dissertations/15>

This Dissertation is brought to you for free and open access by the Graduate School at Louisiana Tech Digital Commons. It has been accepted for inclusion in Doctoral Dissertations by an authorized administrator of Louisiana Tech Digital Commons. For more information, please contact [digitalcommons@latech.edu](mailto:digitalcommons@latech.edu).

Fall 11-17-2018

# Electromagnetic Wave-Matter Interactions in Complex Opto-Electronic Materials and Devices

Raj Kumar Vinnakota  
*Louisiana Tech University*

Follow this and additional works at: <https://digitalcommons.latech.edu/dissertations>

 Part of the [Electromagnetics and Photonics Commons](#), [Engineering Physics Commons](#), [Other Physical Sciences and Mathematics Commons](#), and the [Other Physics Commons](#)

---

## Recommended Citation

Vinnakota, Raj Kumar, "" (2018). *Dissertation*. 15.  
<https://digitalcommons.latech.edu/dissertations/15>

This Dissertation is brought to you for free and open access by the Graduate School at Louisiana Tech Digital Commons. It has been accepted for inclusion in Doctoral Dissertations by an authorized administrator of Louisiana Tech Digital Commons. For more information, please contact [digitalcommons@latech.edu](mailto:digitalcommons@latech.edu).

**ELECTROMAGNETIC WAVE-MATTER INTERACTIONS**  
**IN COMPLEX OPTO-ELECTRONIC**  
**MATERIALS AND DEVICES**

by

Raj Kumar Vinnakota, B.Tech., M.S.

A Dissertation Presented in Partial Fulfillment  
of the Requirements of the Degree  
Doctor of Philosophy

COLLEGE OF ENGINEERING AND SCIENCE  
LOUISIANA TECH UNIVERSITY

November 2018

LOUISIANA TECH UNIVERSITY

THE GRADUATE SCHOOL

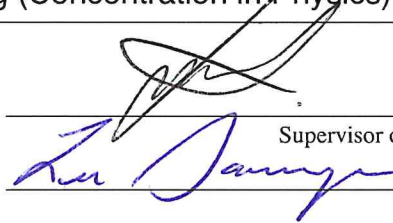
SEPTEMBER 18, 2018

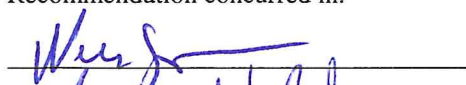
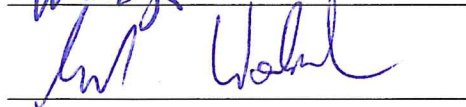
Date

We hereby recommend that the dissertation prepared under our supervision by Raj Kumar Vinnakota B.Tech., M.S.

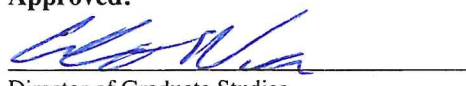
entitled Electromagnetic Wave-Matter Interactions in Complex Opto-electronic Materials and Devices

be accepted in partial fulfillment of the requirements for the Degree of Doctor of Philosophy in Engineering (Concentration in Physics)

  
Supervisor of Dissertation Research  
Head of Department  
Physics  
Department

Recommendation concurred in:  
  
  
  


Advisory Committee

Approved:  
  
Director of Graduate Studies  
  
Dean of the College

Approved:  
  
Dean of the Graduate School

## ABSTRACT

This dissertation explores the fundamentals of light-matter interaction towards applications in the field of Opto-electronic and plasmonic devices. In its core, this dissertation attempts and succeeds in the modeling of light-matter interactions, which is of high importance for better understanding the rich physics underlying the dynamics of electromagnetic field interactions with charged particles. Here, we have developed a self-consistent multi-physics model of electromagnetism, semiconductor physics and thermal effects which can be readily applied to the field of plasmotronics and Selective Laser Melting (SLM). Plasmotronics; a sub-field of photonics has experienced a renaissance in recent years by providing a large variety of new physical effects and applications. Most importantly, plasmotronics promises devices with ultra-small footprints and ultrafast operating speeds with lower energy consumption compared to conventional electronics. One of the primary objectives of this dissertation is to present an optoelectronic switch termed as Surface Plasmon Polariton Diode (SPPD) for functional plasmonic circuits based on active control of Surface Plasmon Polaritons (SPPs) at degenerate  $PN^+$ -junction interfaces.

In this context, the operational characteristics of the proposed plasmonic device are studied by the self-consistent multi-physics model that couples the electromagnetic, thermal and IV characteristics of the device. The SPPD uses heavily doped  $PN^+$ -junction where SPPs propagate at the interface between  $N$  and  $P$ -doped layer and can be switched

by an external voltage. Here, we explore the features of SPPD using three different semiconductor materials; GaAs, Silicon and Indium Gallium Arsenide ( $\text{In}_{0.53}\text{Ga}_{0.47}\text{As}$ ). When compared to Si and GaAs, the  $\text{In}_{0.53}\text{Ga}_{0.47}\text{As}$  provides higher optical confinement, reduced system size and faster operation. For this reason, in our dissertation ( $\text{In}_{0.53}\text{Ga}_{0.47}\text{As}$ ) is identified as the best semiconductor material for the practical implementation of the optoelectronic switch providing high optical confinement, reduced system size, and fast operation. The optimal device is shown to operate at signal modulation surpassing -100 dB and switching rates up to 50 GHz, thus potentially providing a new pathway toward bridging the gap between electronic and photonic devices. Also, the proposed optoelectronic switch is compatible with the current CMOS semiconductor fabrication techniques and could lead to nanoscale semiconductor-based optoelectronics.

Furthermore, we have extended the concept of the above optoelectronic switch to design and study a new type of all-optical switch, referred to as Surface Plasmon Polariton Diode (thermal) (SPPDt). The SPPDt operation is governed by a unique optical nonlinearity that exists only for surface electromagnetic waves, i.e. SPPs, propagating at highly doped semiconductor junction interfaces. This dissertation will address the design and characterization of the SPPDt and will bring new insights into the underlying thermo-optic nonlinearity. The gained understanding will be applied to design practically feasible devices including logic gates which can bridge the temporal and spatial gap between electronics and optics by providing high switching rates and signal input/output (I/O) power modulation.

Enhanced light-matter interactions have further been explored and extended towards tailoring plasmonic resonances due to laser interactions with metal powder beds pertaining to Selective Laser Melting (SLM) processes. This is done by adapting the self-consistent model developed for the plasmonic device to better understand the complex electrodynamic and thermodynamic processes involved in SLM. The SLM is an advanced rapid prototyping or additive manufacturing technology that uses high power density laser to fabricate metal/alloy components with minimal geometric constraints. The fabrication process is multi-physics in nature and its study requires the development of complex simulation tools. In this dissertation, for the first time, the electromagnetic interactions with dense powder beds are investigated under full-wave formalism. Localized gap and surface plasmon polariton resonance effects are identified as possible mechanisms toward improved absorption in small and medium-size titanium powder beds. Furthermore, observed near homogeneous temperature distributions across the metal powders indicates fast thermalization processes and allows for the development of simple analytical models to describe the dynamic interplay of laser facilitated Joule heating and effects of radiation and thermal conduction. The Explicit description is provided for important SLM process parameters such as critical laser power density, saturation temperature, and time to melt. Specific guidelines are presented for improved energy efficiency and optimization of the SLM process deposition rates.

## **APPROVAL FOR SCHOLARLY DISSEMINATION**

The author grants to the Prescott Memorial Library of Louisiana Tech University the right to reproduce, by appropriate methods, upon request, any or all portions of this Dissertation. It is understood that “proper request” consists of the agreement, on the part of the requesting party, that said reproduction is for his personal use and that subsequent reproduction will not occur without the written approval of the author of this Dissertation. Further, any portions of the Dissertation used in books, papers, and other works must be appropriately referenced to this Dissertation.

Finally, the author of this Dissertation reserves the right to publish freely, in the literature, at any time, any or all portions of this Dissertation.

Author Raj Kumar Vinnakota

Date 9/18/2018

## **DEDICATION**

This dissertation is dedicated to my parents, family, and friends who have always been a constant source of support and encouragement throughout my life.

## TABLE OF CONTENTS

ABSTRACT.....	iii
APPROVAL FOR SCHOLARLY DISSEMINATION .....	vi
DEDICATION .....	vii
LIST OF FIGURES .....	xi
LIST OF TABLES .....	xvi
ACKNOWLEDGMENTS .....	1
CHAPTER 1 INTRODUCTION .....	1
1.1 Motivation.....	1
1.2 Previous Work .....	5
1.3 The significance of this Work.....	7
1.4 Organization of this Dissertation .....	9
CHAPTER 2 LIGHT MATTER INTERACTIONS.....	10
2.1 Introduction to Plasmonics .....	11
2.1.1 Theory of Surface Plasmon Polaritons .....	12
2.1.2 The Drude Model and Dispersion Relation .....	15
2.1.3 SPPs in Semiconductors .....	18
2.1.4 SPP Dispersion Relation-Multilayer System .....	20
2.1.5 Propagation Properties of SPP .....	22
2.1.6 SPP Excitation Methods .....	23
2.1.6.1 Grating Coupling .....	23
2.1.6.2 Prism/ATR Coupling.....	24

CHAPTER 3 ACTIVE CONTROL OF CHARGE DENSITY WAVES AT DEGENERATE SEMICONDUCTOR INTERFACES .....	27
3.1 Surface Plasmon Polariton Diode .....	28
3.2 Thermo-electro-optical Model .....	29
3.3 The figure of Merit of SPPD.....	31
3.4 SPPD Operational Characteristics .....	33
3.4.1 Steady State Analysis.....	33
3.4.2 SPPD-Numerical Simulations.....	35
3.4.3 SPPD-Step Response .....	37
3.4.4 SPPD-Response Times and Operation Temperature .....	39
3.5 SPPD Logic Gates .....	42
3.6 SPPD-Temperature Sensor .....	44
3.7 SPPD-Experimental Implementation.....	45
CHAPTER 4 EXPERIMENTAL REALIZATION OF SPPD .....	47
4.1 Fabrication of Si PN <sup>+</sup> -Junction Device.....	47
4.2 SPPD Characterization .....	50
4.2.1 Model for Optical Parameter Extraction.....	50
4.2.2 Reflectivity Measurements and Optical Parameter Extraction.....	54
4.2.3 Reflectivity Modulation and IV Characteristics .....	58
4.2.4 Extraction of Contact resistance .....	59
CHAPTER 5 ALL-OPTICAL SWITCHING OF SPPS USING EXTRAORDINARILY HIGH THERMO-OPTICAL NONLINEARITY .....	61
5.1 Introduction to Thermo-optical Nonlinear Switch.....	61
5.2 Working Principle of SPPDt.....	62
5.3 SPPDt-Steady State Analysis.....	64
5.3.1 Thermo-optic Co-efficient at the doped PN-interface .....	67

5.3.2	Numerical Analysis.....	67
5.3.3	Effect of Doping .....	68
5.3.4	Effect of Operational Frequency.....	69
5.4	SPPDt-Response Times (Transient Analysis) .....	70
5.5	SPPDt Logic Gates .....	71
<b>CHAPTER 6 SURFACE PLASMON ENHANCEMENT IN SELECTIVE LASER MELTING PROCESSES .....</b>		<b>73</b>
6.1	Thermo-optical Model .....	74
6.1.1	Numerical Simulation-Isolated Particle.....	76
6.1.2	Analytical Model .....	78
6.2	Dense Metal Powders .....	80
6.3	Selective Laser Melting-Volumetric Deposition Rate and Energy Efficiency. 85	
<b>CHAPTER 7 CONCLUSION AND FUTURE WORK .....</b>		<b>88</b>
7.1	Concluding Remarks.....	88
7.2	Future Work.....	91
7.2.1	Surface Plasmon Plasmon Diode (SPPD).....	91
7.2.2	Surface Plasmon Polariton Diode (thermal) (SPPDt).....	91
7.2.3	Multiphysics Modelling of SLM Process .....	92
<b>BIBLIOGRAPHY .....</b>		<b>94</b>

## LIST OF FIGURES

<b>Figure 1-1:</b> Past and present trends in Intel Microprocessor technology [1].....	2
<b>Figure 1-2:</b> Temporal and spatial limits of semiconductor electronics, dielectric photonics, semiconductor plasmonics, particle surface plasmons in semiconductors (PSPs), particle surface plasmons in metals (PSP <sub>M</sub> ), surface plasmon polaritons in semiconductors (SPPs), surface plasmon polaritons in metals (SPP <sub>M</sub> ). .....	4
<b>Figure 2-1:</b> Schematic of the surface charges and the electromagnetic field of SPPs propagating on a metal surface in the $x$ -direction. The exponential dependence of the field $E_y$ is seen on the right. $H_z$ shows the magnetic field in the $z$ -direction of the $p$ -polarized wave. ....	13
<b>Figure 2-2:</b> Wave vector of SPPs ( $k_{spp}$ ) propagating on silver/air interface (red curve). The green line represents the wave vector of light in air ( $k_0$ ), while the blue dotted line corresponds to the surface plasmon frequency $\omega_{sp} = \omega_p / \sqrt{\epsilon_d + \epsilon_m}$ . .....	16
<b>Figure 2-3:</b> Plasma frequencies versus the doping concentration. The blue line is n-In <sub>0.53</sub> Ga <sub>0.47</sub> As, the green line is n-GaAs and the red line is n-Si. ....	19
<b>Figure 2-4:</b> Geometry of a three-layer system consisting of a thin layer (1) with permittivity $\epsilon_1$ is sandwiched between two infinite half spaces (2) and (3). ....	20
<b>Figure 2-5:</b> Grating coupler: Matching incident light to SPP wavevector. ....	24
<b>Figure 2-6:</b> Prism coupling and SPP dispersion. Propagation constants between the light lines of air and the prism are accessible, resulting in additional SPP damping due to the leakage radiation into the latter; the excited SPPs have propagation constants inside the prism light cone. ....	25
<b>Figure 2-7:</b> Prism coupling to excite SPPs using the attenuated total internal reflection in the (a) Kretschmann and (b) Otto configurations. ....	26
<b>Figure 3-1:</b> Basic schematic of a Surface Plasmon Polariton Diode (SPPD). ....	29
<b>Figure 3-2:</b> Self Consistent thermo-electro-optic model. ....	30
<b>Figure 3-3:</b> The Surface Plasmon Polaritons (SPPs) Figures of Merit (FOM) vs. frequency and doping for (a,b,c) Si and (d,e,f) In <sub>0.53</sub> Ga <sub>0.47</sub> As. ....	32

**Figure 3-4:** The Surface Plasmon Polaritons (SPPs) dispersion at different external bias voltages for (a) Si with doping concentrations;  $N_A = 1 \times 10^{20}$ ,  $N_D = 4 \times 10^{20} \text{ cm}^{-3}$  (b)  $\text{In}_{0.53}\text{Ga}_{0.47}\text{As}$  with  $N_A = 1 \times 10^{19}$ ,  $N_D = 5 \times 10^{19} \text{ cm}^{-3}$  and GaAs with  $N_A = 5 \times 10^{19}$ ,  $N_D = 5 \times 10^{19} \text{ cm}^{-3}$ . The SPPD transmittance for (d) Si (e)  $\text{In}_{0.53}\text{Ga}_{0.47}\text{As}$  and (f) GaAs, for different  $P$ -doping concentrations, are obtained using the self-consistent Multiphysics model (dots, dashed) and compared to the WKB approximation (solid lines). The corresponding responsivities are shown as inserts of (d, e). In the calculations the operation frequency is set at 30 THz, the thickness of the  $P$ -type layer is  $d = 1.5 \mu\text{m}$ ,  $n_b$  identifies the refractive index of  $P$ -layer and the overall length of the active drift-diffusion region is fixed at  $w = 4 \mu\text{m}$ . ... 35

**Figure 3-5:** (a, b, c) Steady-state minority carrier concentration profiles at different applied voltages. (d, e, f) Surface Plasmon Polariton (SPP) propagation along the length of the device. (g, h, i) Local temperature profile. In the calculations the operation frequency is set at 30 THz, the thickness of the  $P$ -type layer is  $d = 1.5 \mu\text{m}$  and the overall length of the active drift-diffusion region is fixed at  $w = 4 \mu\text{m}$ . ..... 37

**Figure 3-6:** SPPD output signal (solid line) under step-type of input voltage (dashed black line) with magnitude (a) 1.3 V for Si and (b) 0.9 V for  $\text{In}_{0.53}\text{Ga}_{0.47}\text{As}$  and (b) 4 V for GaAs. The signal is repetitively switched following the external voltage. In the calculations, the operation frequency is set at 30 THz, and the donor doping concentration is  $N_D = 4 \times 10^{20} \text{ cm}^{-3}$  for the Si device,  $N_D = 5 \times 10^{19} \text{ cm}^{-3}$  for the  $\text{In}_{0.53}\text{Ga}_{0.47}\text{As}$  device and  $N_D = 5 \times 10^{19} \text{ cm}^{-3}$  for the GaAs device..... 39

**Figure 3-7:** (a, d, g) Dependence of the SPPD OFF times on the applied voltage ( $V > V_C$ ). The device OFF time is dependent on the electron drift into the p-region and is thus inversely proportional to the applied voltage. (b, e, h) Dependence of the SPPD ON times on the applied voltage ( $V > V_C$ ). (h) The SPPD response times as function of the  $P$ -layer doping concentration. (c, f, i) The maximum temperature recorded inside the device vs. the applied voltage. In the calculations the operation frequency is set at 30 THz. The doping concentrations for the Si device are  $N_A = 1 \times 10^{19} \text{ cm}^{-3}$  (blue dots) and  $N_A = 1 \times 10^{20} \text{ cm}^{-3}$  (red dots) with  $N_D = 4 \times 10^{20} \text{ cm}^{-3}$ , for  $\text{In}_{0.53}\text{Ga}_{0.47}\text{As}$  the doping concentrations are  $N_A = 1 \times 10^{19} \text{ cm}^{-3}$  (red dots) and  $N_A = 1 \times 10^{18} \text{ cm}^{-3}$  (blue dots) with  $N_D = 5 \times 10^{19} \text{ cm}^{-3}$  for GaAs  $N_A = N_D = 5 \times 10^{19} \text{ cm}^{-3}$ . The doping influences both the width of the space charge region and the electron mobility thus modifies to a different extent the ON and OFF times. In the figures, the numerical data (dots diamonds) is compared to the analytical drift-diffusion model (solid lines). ..... 41

**Figure 3-8:** (a, d) Schematic of the SPPD logic (NAND and NOR) gates. (c, f) Logic table of the SPP NAND and NOR gates. (b, e) SPP propagation in the SPPD based NAND and NOR gates corresponding to the control voltages  $V_1$  and  $V_2$  as specified in the logic tables. .... 43

**Figure 3-9:** SPPD temperature sensor. Due to the abrupt (exponential) switching of the SPPD output signal, a temperature sensitivity of less than 1.7mV/K is demonstrated. .... 44

<b>Figure 3-10:</b> (a) Schematic of the SPPD with input and output waveguides coupling. (b) Magnetic field intensity for two different input grating $\Lambda_1 = 6 \mu m$ (top) and $\Lambda_1 = 5 \mu m$ (bottom) at constant SPP cavity grating $\Lambda_2 = 2.6 \mu m$ . (c) SPP coupling efficiency for the $\Lambda_1 = 6 \mu m$ (top) grating showing maximum efficiency at operating frequency of 30 THz. (d) SPP coupling efficiency for the $\Lambda_1 = 5 \mu m$ (bottom) grating showing maximum efficiency at operating frequency of 25 THz. ....	46
<b>Figure 4-1:</b> Fabrication process flow for the manufacturing of degenerate semiconductor (Si) PN <sup>+</sup> junctions.....	48
<b>Figure 4-2:</b> (a) Layer structure for the P spin-doped SOI wafer, and device schematic for the spin-doped N <sup>++</sup> P junction diode following wafer-bonding, substrate removal, and device fabrication. (b) Experimental set-up for amplitude modulation step-scan measurement of reflection ( $ R $ ) modulation from the biased devices. ....	49
<b>Figure 4-3:</b> The built-in electrical potential obtained by numerically solving <b>Eq. 4-2</b> (solid lines) is compared to the charge neutrality result <b>Eq. 4-3</b> (dashed line). The doping parameters used are $\lambda = 1$ (blue), $\lambda = 3$ (green), and $\lambda = 10$ (red). In all calculations, we have set $n_i/N_D = 0.01$ and $N_A/N_D = 0.1$ . ....	52
<b>Figure 4-4:</b> Dependence of (a) effective mass and (b) mobility on doping. ....	53
<b>Figure 4-5:</b> (a) Reflectance and (b) Effective permittivity of the <i>P</i> -doped wafer. ....	54
<b>Figure 4-6:</b> (a) Schematic of the un-doped multilayer device. (b) Comparison of the experiment (red solid line) and TMM model (blue and green solid line).....	55
<b>Figure 4-7:</b> (a) Schematic of the SOI wafer after spin on diffusion of <i>N</i> -type impurities, (b) Comparison of reflectance due to experiment (red solid line) and TMM model (blue solid line), (c) plasma frequency, (d) relaxation frequency, (e) electron concentration and (d) permittivity.....	56
<b>Figure 4-8:</b> (a) Schematic of the Si PN-diode with the bottom gold anode. (b) Comparison of the experiment (red solid line) and TMM model (blue and green solid line). ....	57
<b>Figure 4-9:</b> (a) Schematic of the Si PN-diode with top and bottom electrodes. (b) Comparison of the experiment (red solid line) and TMM model (blue) and direct full-wave simulation using the COMSOL software (green dots). ....	58
<b>Figure 4-10:</b> (a) Schematic of the Si PN-diode with top and bottom electrodes. (b) Comparison of the experiment (red solid line) and TMM model (blue) and direct full-wave simulation using the COMSOL software (green dots). ....	59
<b>Figure 4-11:</b> (a) Equivalent circuit for the PN-diode in series with the contact resistance. (b) IV-curve comparison of the experiment (red solid line), analytical model (dashed blue) and ideal diode IV (dashed black).....	60

- Figure 5-1:** Schematic of the SPPDt..... 63
- Figure 5-2:** The Surface Plasmon Polaritons (SPPs) dispersion at constant external bias voltages  $V_a = 1.12 V$  and different lattice temperature for (a) Si with doping concentrations;  $N_A = 1 \times 10^{20}$ ,  $N_D = 4 \times 10^{20} cm^{-3}$ . (b) The SPPDt transmittance for Si at obtained using the self-consistent Multiphysics model (dots) and compared to the WKB approximation (solid lines). In the calculations the operation frequency is set at 30 THz, the thickness of the  $P$ -type layer is  $d = 1.5 \mu m$ ,  $n_b$  identifies the refractive index of  $P$ - layer and the overall length of the active drift-diffusion region is fixed at  $w = 4 \mu m$ ..... 65
- Figure 5-3:** Thermo-optic co-efficient at doped PN-junction..... 67
- Figure 5-4:** (a) Steady-state minority carrier concentration profiles at a constant applied voltages  $V_a = 1.12 V$  and different lattice temperature  $T = (300 K, 350 K, 400 K)$ . (b) Surface Plasmon Polariton (SPP) propagation along the length of the device..... 68
- Figure 5-5:** The SPPDt transmittance for Si at different  $P$ -doping concentrations and different external voltage  $V = (1.1 V, 1.12 V, 1.15 V)$ . are obtained using the self-consistent Multiphysics model (dots) and compared to the WKB approximation (solid lines). In the calculations the operation frequency is set at 30 THz, the thickness of the  $P$ -type layer is  $d = 1.5 \mu m$  and the overall length of the active drift-diffusion region is fixed at  $w = 4 \mu m$ ..... 69
- Figure 5-6:** The SPPDt transmittance for Si at different operational frequencies and different external voltage  $V = (1.1 V, 1.12 V, 1.15 V)$  are obtained using the self-consistent Multiphysics model (dots) and compared to the WKB approximation (solid lines). In the calculations, the thickness of the  $P$ -type layer is  $d = 1.5 \mu m$  and the overall length of the active drift-diffusion region is fixed at  $w = 4 \mu m$ ..... 70
- Figure 5-7:** (a,b) Schematic of the TSPD logic (NAND and NOR) (c,d) Logic table corresponding to the NAND and NOR gates, respectively. .... 72
- Figure 6-1:** Self Consistent thermo-optic model..... 75
- Figure 6-2:** (a) Absorption cross-section of isolated titanium (Ti) particle using the Mie theory. At the chosen operational wavelength  $\lambda = 1.070 \mu m$  (corresponding to Concept Laser Mlab cusing R 3D printer [112]) the refractive index of titanium is  $n_p = 3.4740 + i4.0113$  [113]. (b) The local Joule heating is found to be predominantly along the polarization direction of the impinging radiation and the steady state temperature profile of the particle ( $R = 0.5 \mu m$ ) irradiated with laser power density  $P_0 = 200 W/cm^2$  is found to be remarkably homogeneous. (c, d) The volume-averaged particle temperature as a function of the elapsed time is obtained using the self-consistent multiphysics model (dots) and compared to the analytical result given by **Eq. 6-3** (solid lines). In (c) the size of the particle is fixed at  $R = 0.5 \mu m$  and irradiated with three different laser power densities  $P_0 =$

200, 320, 500 W/cm<sup>2</sup>, while in (d) three different particle sizes are investigated at a fixed laser power density  $P_0 = 500$  W/cm<sup>2</sup>. In the calculations, the operational wavelength is set at 1.070  $\mu$ m, and the particle melting temperature is shown with dashed line. .... 77

**Figure 6-3:** Absorptance versus particle size for closely packed (touching) titanium spheres arranged in a square lattice on top of a titanium substrate (see insert). In the calculations, the laser radiation is normal to the particle bed and the laser wavelength is set at 1.070  $\mu$ m. Morphologically dependence resonances are manifested due to electromagnetic interactions between neighbors and excitation of surface plasmon states (points A, B, and C). .... 81

**Figure 6-4:** (a, b, c) Local electric field profiles due to impinging (from the left) laser radiation showing excitation of standing surface waves associated with surface plasmon polaritons (SPPs). (d, e, f) The SPP modes induce localized Joule heating which is found to be predominantly on the polarization direction of the impinging radiation. (g, h, i) The local steady-state temperature on the particle surface shows a highly homogeneous distribution despite the strongly localized Joule heating. In the calculations, the operational wavelength is set at 1.070  $\mu$ m and the incoming laser beam power density is  $P_0 = 40$  W/cm<sup>2</sup>. .... 82

**Figure 6-5:** The volume-averaged particle temperature as a function of the elapsed time for a periodic array of titanium particles obtained using the self-consistent multiphysics model (dots) and compared to the analytical result (solid line). (a) The size of the particle is set to match the  $n = 1$  SPP resonance (point A) and is irradiated with three different laser power densities  $P_0 = (40, 82, 200)$  W/cm<sup>2</sup>. (b) The temperature versus time calculated for periodic arrays of titanium particles with varying sizes and irradiated with a constant laser power density  $P_0 = 200$  W/cm<sup>2</sup>. In the calculations, the operational wavelength is set at 1.070  $\mu$ m. .... 84

**Figure 6-6:** (a) Volumetric Deposition rate as a function of particle size and incident laser intensity. In the calculations the operational wavelength is set at 1.070  $\mu$ m, incident laser power as  $W_0 = 100$  W. The periodic array of homogenous sized particle array is irradiated with three different laser power densities  $P_0 = (500, 200, 100)$  W/cm<sup>2</sup>. The corresponding maximum volumetric deposition rate (MVDR) is depicted by black dots. (b) Efficiency as a function of incident laser intensity. .... 86

**LIST OF TABLES**

**Table 5-1:** SPPDt characteristic times. .... 71

## **ACKNOWLEDGMENTS**

I would like to acknowledge and express my sincere gratitude to my advisor, Professor Dentcho A. Genov. I was truly fortunate to work with and learn from such a world-class researcher and a wonderful person. I am grateful for his valuable feedback. He is my true inspiration throughout my Ph.D. and I hope will reach his level of expertise in science and work ethics in my future academic pursuits. I would also like to thank Dr. Neven Simicevic for his motivation and being patient with my numerous questions (from teaching to research). Many thanks to Dr. Markus Wobisch, Dr. Sandra R. Zivanovic, and Dr. Arun Jaganathan for agreeing to be on my committee and reviewing this work. I am also thankful and in debt to Dr. Daniel Wasserman from the UT Austin for exciting discussions and inputs. Special thanks to my best buddies Brandon Touchet and Neal Blackman for their highly stimulating discussions, for they have greatly added to the value of this dissertation. I am also thankful to my colleagues Mona Alsaleh and Venkatesh K. Pappakrishnan for their valuable suggestions and discussions.

My deepest gratitude goes to my friend Niranjan Babu Bandla for pushing me with constant support and enthusiasm. I would like to thank my father Appala Raju Vinnakota and my mother Ratna Kumari Vinnakota, without whom my goals would have been incomplete. I express my honest gratitude to my godparents Kalpesh Daya and Rekha Daya for their unconditional love and support. Finally, I would like to thank my wife Madhuri, who is my life.

# CHAPTER 1

## INTRODUCTION

### 1.1 Motivation

The demands for faster data transfer and processing has increased dramatically over the past five decades. This has led to enormous advances in the semiconductor industry and a continuous progression towards smaller, faster, and more efficient electronic devices [1]. The scaling of the electronic devices also brought about a myriad of challenges. The most daunting problems inhibiting the significant further increase in the processor speed are thermal and resistor-capacitor (RC) delay time, associated with the electronic interconnections and scaling of the devices [2]. Because of these scaling issues and excessive heat dissipation, saturation in the microprocessor clock speed has been observed over the past decade (see **Figure 1-1**) [2].

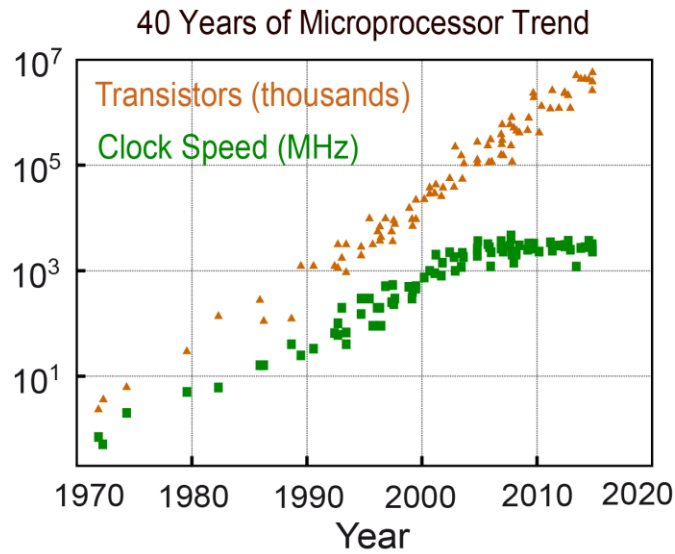


**Figure 1-1:** Past and present trends in Intel Microprocessor technology [1].

Researchers have long realized that photonics could be a key technology for fast data communication and computing [2-6]. It is now well understood that photonic devices have the potential to address some of the present bottlenecks in semiconductor-based electronics such as high-power consumption and interconnects delay times. Also, photonic devices can operate at low transmission losses and provide extremely large bandwidths due to multiplexing capabilities, operating on several channels in parallel. Unfortunately, the implementation of photonic devices within electronic components has been limited predominantly due to size mismatch, i.e. the optical components are diffraction limited to half the wavelength in the optical material. Moreover, it is expected that CMOS foundries will further decrease the feature sizes on silicon chips, ultimately down to 10 nm. This reduction in size would further increase the dimensional mismatch, as the size of the dielectric photonic devices is restricted by the diffraction limit [2]. Furthermore, miniaturizing introduces several problems including a dielectric breakdown, hot carriers and short channel effects, which degrade device reliability [7]. A

possible solution which can facilitate the size and power requirement for future integrated circuits lies in designing photonics components below the diffraction limit.

Due to the dramatic advances in nanotechnology and its applications in the area of photonics, and specifically plasmonics, now it is believed feasible to merge electronics with sub-wavelength optics in a new field of sub-wavelength optoelectronics [2-4]. Plasmonics is the study of Surface Plasmon Polaritons (SPPs), i.e. spatially confined electromagnetic modes propagating at the metal-dielectric interfaces which offer the bandwidths of photonic devices and physical dimensions shared with nanoscale electronics [2-4] [6] [8] [11-23]. One of the most fascinating aspects of SPPs is the way light can be channeled using device geometries much smaller than the free space wavelength. The SPPs propagate at the interface of metals/semiconductors and has been used in wide range of disciplines including bio-sensing [24], super lensing [25-27], nano lasing [10] [28], optical invisibility, and metamaterials [29-30].

Furthermore, the potential of such synergy offered by plasmonics is depicted in **Figure 1-2** where the fundamental limits of the operation speed vs. spatial size for a large variety of optical, optoelectronic and all-electronic devices is shown. The speed and size of the devices rely on the unique material properties of semiconductors (electronics), insulators (photonics), and metals (plasmonics) [8]. Semiconductor electronics is limited in speed by heat generation and interconnect delay time to about 10 GHz [8]. Metal-based plasmonics ( $SPP_M$  and  $PSP_M$ ) can share the dimensions of nano-scale electronics and speeds offered by dielectric photonics. However, metal plasmonics cannot be merged to nano-scale electronics due to the mismatch in the frequency of operation. Semiconductor plasmonics can share both (size and frequency of operation) as that of

nano-electronics in addition to speeds and data rates as that of dielectric photonics. Thus, optoelectronic and all-optical devices based on semiconductor plasmonics can offer a unique solution to merge subwavelength optics with nano-electronics.

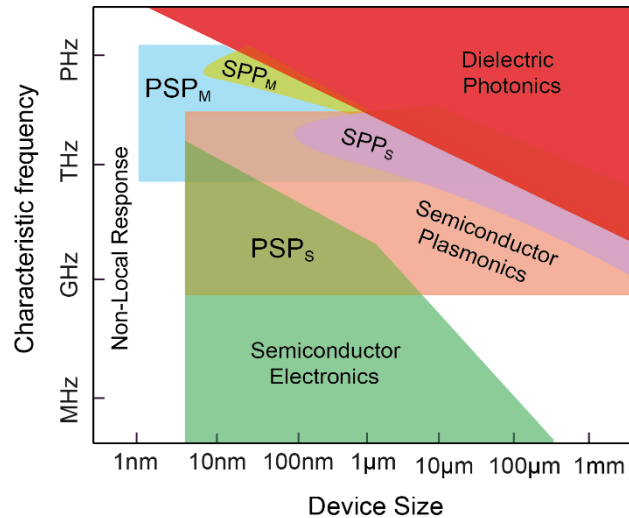


**Figure 1-2:** Temporal and spatial limits of semiconductor electronics, dielectric photonics, semiconductor plasmonics, particle surface plasmons in semiconductors ( $PSP_s$ ), particle surface plasmons in metals ( $PSP_M$ ), surface plasmon polaritons in semiconductors ( $SPP_s$ ), surface plasmon polaritons in metals ( $SPP_M$ ).

Recently, light-trapping layers employing metallic plasmonic microstructures have gained significant attention [31-33], efficient resonant light absorption by several plasmonic nanostructures with microcavities [34], and gap-plasmon resonators [35] [36] have been extensively studied. Regarding metal-based absorbers, absorption enhancement using stacked plasmonic resonators, colloidal microspheres, and their corresponding arrays has been also presented [37-41]. Extensive light trapping through surface plasmon resonances can be applied to the field of three-dimensional (3D) printing with metals and alloys using selective laser melting (SLM). SLM is the most promising and successful additive manufacturing technique to date [42-44]. The SLM is a layer-by-

layer rapid manufacturing technology that uses high power laser beams to melt and fuse metallic powders in a controlled manner [44]. The technology is known for printing high-quality 3D metal-parts with high geometric complexity. A significant feature of the SLM is near-net-shape production without the need for expensive molds or time-consuming post-processing and high production flexibility [45] [46]. Due to the numerous advantages compared to traditional manufacturing technologies, the implementation of SLM in the industry has been rapidly increasing [42] [43] [47] [48]. However, further improvements in productivity and reduction in costs are crucial factors that need to be addressed for future widespread SLM implementation.

The fundamental physical processes involved in SLM are complex and include scattering and absorption of laser radiation into highly heterogeneous metal powders, heat transfer, the formation of molten pools and its solidification, all within multiple lengths and timescales. Extreme confinement and light trapping can convert the electromagnetic energy into heat with high efficiency and thus can fasten the initiation of the melting in SLM powders.

## 1.2 Previous Work

The potential of plasmonics to bridge the gap between electronics and photonics is now well recognized by the scientific community with a large number of investigators working in the field [9]. In 2008, Brongersma *et al.* demonstrated all-optical switch based on SPP waveguide that uses metallic (passive) nanostructures coupled with active PMMA films with photochromic molecules [9]. Unfortunately, the switching rates of the photochromic molecules were low (~20 ns) [9]. The active electronically controlled plasmonic element has been demonstrated as a selective ring resonator switch [48] where

the SPPs are controlled by induced small refractive index changes of order  $10^{-3}$ . A sub-micron bidirectional all-optical plasmonic switch with asymmetric T-shape single slit was recently demonstrated with transmission modulation of -6 dB [49]. All-optical absorption and gain-assisted switching were demonstrated using the SPP waveguide coupled with PMMA films [8] and a cavity filled with a semiconductor (InGaAsP) gain material [50]. A metal-oxide-Si field effect plasmonic modulators, and all-optical modulation by plasmonic excitation of CdSe quantum dots have been investigated at visible and telecommunication frequencies [13] [51].

Recently, a fast-all-optical switch based on a carbon nanotube metamaterial has been proposed; however, the device shows a rather low transmission modulation of less than 10% [52]. The SPP modulation rates so far demonstrated a range from a few kHz [13] to tens of MHz [53-55]. Overall, the rapid progress in the past few years have shown that (i) exceedingly fast (tens of Gbit/s) optoelectronic switching can be achieved using dielectric components. However, the device sizes are large ( $> 100\mu m^2$ ) and the signal modulation is relatively low (few dB), while (ii) metal-based plasmonic modulators can have small sizes ( $< 1\mu m^2$ ). However, an efficient switching mechanism is still to be identified. Despite the progress, it is arguable that in order for optoelectronic devices to compete with their all-electronic counterparts, a signal modulation surpassing -10 dB and bandwidths beyond the current limit of 10 GHz must be achieved.

Alternatively, to address the above-mentioned shortcoming related to SLM, different methods have been proposed. These include the use of higher power lasers to melt multiple layers at the same time [56], or the use of multiple lasers [57]. Increase in SLM productivity has been achieved by using up to four lasers simultaneously and by

implementing the hull-core scanning strategy [58]. Unfortunately, limited installation space for optical components hinders further increase in the number of lasers. Moreover, the hull-core strategy mainly offers significant benefits to parts requiring heavy wall-thickness that are usually not manufactured using SLM. Hence, there is a clear need for alternative paths toward improved productivity. Currently, the SLM process is limited by the maximum laser energy deposited in the powder bed, which mainly depends on material properties (absorbance) as well as SLM process scan rates. Therefore, in order to improve productivity, a comprehensive understanding of the complex laser-matter interactions with the powder bed is required. Also, experimental and numerical approaches have been proposed to study the complex multiphysics involved in SLM metal powder materials [59-63]. The analysis of the absorption of electromagnetic energy from the laser is usually based on the solution of the corresponding diffraction problem under the ray approximation while the wave nature of the interactions, including excitation of cavity and especially surface resonances are commonly neglected [64-68].

### 1.3 The significance of this Work

The available literature related to plasmonic switching shows an emphasis on control and modulation of SPPs on metal surfaces; however, not much attention is being paid on the fact that due to the extremely high plasma frequencies inherent to noble metals (for silver  $\omega_p = 9$  eV) there is a substantial bandwidths mismatch with electronics that cannot be easily bridged. In this dissertation, we demonstrate efficient excitation and active control of SPPs at the interface of highly doped *N*-type and *P*-type semiconductors. Utilizing highly doped semiconductor material serves three distinct purposes: (i) act as a metal-like interface to allow propagation of SPPs, (ii) allow fast

electronic switching of the SPP facilitated by a  $PN$ -junction, and (iii) provides an operation frequency that is tunable across the THz frequency range. In particular, to study the complex multiphysics involved in the semiconductor based plasmonic switch, we developed a numerical framework to self-consistently solve the Maxwell's, Poisson-Boltzmann, drift-diffusion and heat equations. This model allows for accurate simulations of the excitation and electro-optical and all-optical control of the SPPs, the minority carrier transport across the  $PN^+$ - junction, the spatially and time dependent local permittivity variations under external bias, and the introduction of thermal effects due to Ohmic heating and electromagnetic energy dissipation.

Alternatively, the available literature associated with Selective Laser Melting (SLM) technology mainly focuses on the analysis of the laser energy absorption based on the solution of the corresponding diffraction problem under the ray approximation. In this dissertation, we consider the commonly neglected wave nature of the interactions leading to new physics including excitation of the cavity and especially surface resonances. Thus, we show that further optimization in the energy absorption by the metal powders could be achieved by laser action on metal particles if the laser pulse with frequency is closely tuned to the particle's SPP resonances, resulting in localized electron excitations, and leading to the optical resonance phenomena [69-72]. To study the complex multiphysical phenomena involved in actual powder beds, where length scales can vary from nanometers into tens of micrometers, here we have developed a general numerical and high-fidelity analytical model which can describe the system beyond the ray approximation. Most importantly, for the first time, the electromagnetic interactions with dense powder beds are investigated under full-wave formalism. Localized gap and

surface plasmon polariton resonance effects are identified as possible mechanisms toward improved absorption in small and medium-size titanium powder beds.

The work done for this dissertation has contributed to the publications [120-128].

#### **1.4 Organization of this Dissertation**

The remainder of the dissertation is organized as follows. Chapter 2 presents an overview of the fundamentals of light-matter interactions. It also presents studies of the dispersion relations of guided modes (including SPPs) in 3-layer configuration such as dielectric-dielectric-metal structures. Chapter 3 investigates a novel semiconductor-based optoelectronic switch called Surface Plasmon Polariton Diode (SPPD). It also provides an explicit description of SPPs at degenerate semiconductor interfaces. Chapter 4 discusses a novel all-optical plasmonic switch. Chapter 5 presents experimental data and analysis related to the proposed optoelectronic switch. Chapter 6 presents the surface plasmon induced enhancements in SLM powder beds.

## CHAPTER 2

### LIGHT MATTER INTERACTIONS

Before exploring the rich Multiphysics phenomenon involved in plasmonic devices and laser interaction with metal powder beds, first, we briefly discuss the basic physical concepts which are critically needed to comprehend the more detailed discussions in the following chapters.

The fundamental processes involved when light interacts with matter are in principle described more precisely by the means of quantum theory. This can be explained in three basic processes. For simplicity, let us consider a 2-level atom with a lower energy state  $E_1$  and a higher energy state  $E_2$ . (i) Absorption is when an incident radiation gets absorbed, the atom uses the absorbed energy to jump into a higher energy state. The transition energy equates the difference between the two levels such that  $h\nu = E_2 - E_1$ , where  $h$  is the plank's constant and  $\nu$  is the frequency of the incident radiation. (ii) spontaneous emission is the electron in the higher energy state that can fall into the lower energy level with the emission of energy equal to  $h\nu$  being sent out as a photon. The last process for the light-matter interaction is (iii) stimulated emission is where the excited electron in the upper energy level can be triggered to jump to the lower energy state by an incoming radiation. Scattering and absorption fits quite well into the above described elementary processes.

Scattering of light by spherical particles is one of the fundamental problems of electrodynamics. It is a classical subject for which a theory was developed long ago, and it includes both the near and far field interactions. Light scattering due to particles that are considerably smaller than the light wavelength is known as Rayleigh scattering developed by Lord Rayleigh in 1871 [73]. For particles with sizes on the order of light wavelengths or larger, the scattering takes place mainly in the forward direction known as Mie scattering developed by Gustav Mie in 1908 [74]. Until recently, the interest was mainly towards far-field effects. Due to the advances in nanotechnology and specifically nano-optics, the rich physics behind the near-field effects are presently being explored. This comprise of the scattering of light intensities with spatial variations shorter than the incident wavelength, a phenomenon that enables new underlying physics, both linear and nonlinear effects, at the nanoscale. In this dissertation, we explore the possible benefits of SPPs towards optoelectronic, all-optical plasmonic devices with potential applications in optical computing and sensing. Also, for the first time, we study the SPP enhancements in SLM metal powder beds.

## **2.1 Introduction to Plasmonics**

Plasmonics is the sub-field of photonics devoted to the study of SPPs, a collective electron oscillation that propagates at the interface between a dielectric and a metal. Surface plasmons have been investigated for over a century, starting from experiments using diffraction gratings used for optical characterization, theoretical work by Rayleigh on diffraction [73], Zenneck's and Sommerfeld's work on surface waves [75] and later improvements in the understanding of metals, especially using the Drude's behavior [76]. Ritchie [77] was the first researcher to study the propagating surface plasmons. He has

first observed that the free electrons on the surface of the metal can attain coherent fluctuations which are called surface plasma oscillations. Later, the existence of the coherent fluctuations has been demonstrated in electron energy-loss experiments conducted by Powell and Swan [78].

One of the key concepts related to SPPs is its dispersion relation. This is the origin of understanding the coupling of light to SPPs. Moreover, dispersion relation benefits in predicting the matching of localized surface plasmons (LSPs) and SPPs to achieve highly enhanced electromagnetic field transmission. Close observation of the SPP dispersion relation suggests that the SPPs cannot be excited when the light is incident directly on to a flat metal-dielectric interface. This is because of the wavevector mismatch between the incident light and corresponding SPP mode. Therefore, we need special mechanisms that can assist in providing additional momentum essential for the coupling of incident light to the metal-dielectric interface. The preceding sections are devoted to the basic background and theory of SPPs, excitation mechanisms, and applications of SPPs in the light guiding.

### 2.1.1 Theory of Surface Plasmon Polaritons

**Figure 2-1** depicts the simplest geometry sustaining the SPPs. To investigate the properties of the SPPs, we need to study the dispersion relation of SPPs at the flat interface between a metal ( $y < 0$ ) and a dielectric ( $y > 0$ ). Metal exhibits complex dielectric constant  $\epsilon_1$ , in which the real part  $Re[\epsilon_1] < 0$  is negative and the top dielectric layer has positive dielectric constant  $\epsilon_2 > 0$ .

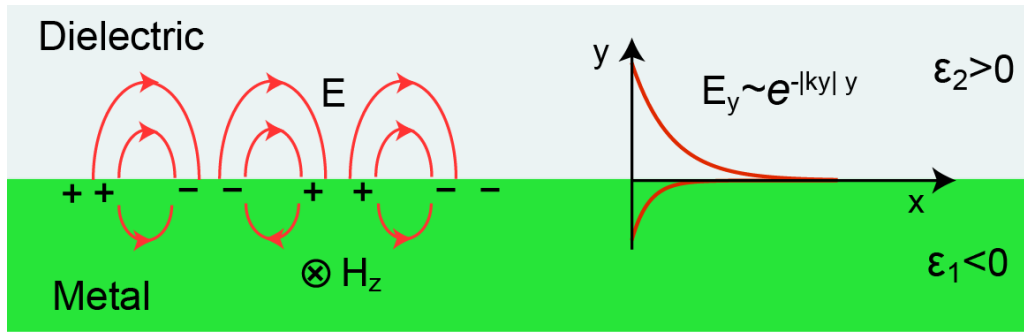


**Figure 2-1:** Schematic of the surface charges and the electromagnetic field of SPPs propagating on a metal surface in the  $x$ -direction. The exponential dependence of the field  $E_y$  is seen on the right.  $H_z$  shows the magnetic field in the  $z$ -direction of the p-polarized wave.

Let us assume an electromagnetic wave propagating along the  $x$ -direction with wavevector  $k_x$  at the interface of two materials (see **Figure 2-1**). Here we consider a polarized transverse magnetic (TM) wave in the  $z$ -direction  $\vec{H} = H(x, y)\hat{z}$  bound to the surface; the field has its maximum at the interface and decays exponentially into both materials. The frequency  $\omega$ , of these longitudinal oscillations, is tied to its wave vector  $k_x$  by a dispersion relation  $k_x(\omega)$ . The SPPs dispersion relation is obtained by enforcing the appropriate boundary conditions and solving the wave equations of the magnetic field in both materials

$$\frac{\partial^2 \vec{H}_1}{\partial x^2} + \frac{\partial^2 \vec{H}_1}{\partial y^2} = \frac{\varepsilon_1 \mu_1}{c^2} \frac{\partial^2 \vec{H}_1}{\partial t^2}, \quad y < 0 \quad \text{Eq. 2-1}$$

and

$$\frac{\partial^2 \vec{H}_2}{\partial x^2} + \frac{\partial^2 \vec{H}_2}{\partial y^2} = \frac{\varepsilon_2 \mu_2}{c^2} \frac{\partial^2 \vec{H}_2}{\partial t^2}, \quad y > 0 \quad \text{Eq. 2-2}$$

where  $\varepsilon_1$ ,  $\mu_1$ , and  $\vec{H}_1$  are the relative permittivity, permeability and the magnetic field of the material (1), respectively, and  $\varepsilon_2$ ,  $\mu_2$ , and  $\vec{H}_2$  correspond to the material (2),  $c$  is the speed of light in the vacuum which can be written as  $c = 1/\sqrt{\varepsilon_0 \mu_0}$ , where  $\varepsilon_0$  and  $\mu_0$  are

the permittivity and permeability of free space. We notice that most normal materials have permeability equal to unity ( $\mu_1 = \mu_2 = 1$ ). Assuming a harmonic propagation with frequency  $\omega$ , we seek a solution of the governing **Eq. 2-1** and **Eq. 2-2** in the form of plane waves, and the z-polarized magnetic field can be expressed as

$$\vec{H}_1(x, y) = \hat{z} H_1 e^{i(k_x x + k_{y1} y)} e^{-i\omega t}, \quad y < 0 \quad \text{Eq. 2-3}$$

and

$$\vec{H}_2(x, y) = \hat{z} H_2 e^{i(k_x x - k_{y2} y)} e^{-i\omega t}, \quad y > 0 \quad \text{Eq. 2-4}$$

where  $k_x$  is the SPP wave vector, and the transversal wave vectors

$k_{y1}, k_{y2}$  corresponding to material (1) and the material (2) are given as

$$k_{y1}^2 = \varepsilon_1 k_0^2 - k_x^2 \text{ and } k_{y2}^2 = \varepsilon_2 k_0^2 - k_x^2 \quad \text{Eq. 2-5}$$

where  $k_0 = \omega/c$  is the free space wave vector. Furthermore, we can estimate the electrical field by using Maxwell's curl equation (Ampere's law):

$$\nabla \times \vec{H}_{(1,2)} = \frac{\partial \vec{D}_{(1,2)}}{\partial t} \quad \text{Eq. 2-6}$$

where we assume zero conduction currents  $J = 0$  and  $\vec{H}_{(1,2)}$  is the magnetic field corresponding to material (1) and material (2). The electrical field displacement for material (1) and material (2) respectively is written as  $\vec{D}_{(1,2)} = \varepsilon_{(1,2)} \vec{E}$ . For harmonic oscillation, we again write it as  $\vec{E}(t) = E_0 e^{-i\omega t}$ , where  $E_0$  is the amplitude of the electrical field. Then from **Eq. 2-6**, we obtain

$$\vec{E}_1 = \left( -\frac{1}{i\varepsilon_1 \omega} \right) \left( \frac{\partial \vec{H}_1}{\partial y} \hat{x} - \frac{\partial \vec{H}_1}{\partial x} \hat{y} \right) \quad \text{Eq. 2-7}$$

$$\vec{E}_2 = \left( -\frac{1}{i\varepsilon_2 \omega} \right) \left( \frac{\partial \vec{H}_2}{\partial y} \hat{x} - \frac{\partial \vec{H}_2}{\partial x} \hat{y} \right) \quad \text{Eq. 2-8}$$

The continuity at the boundary ( $y = 0$ ) results in  $E_{1x} = E_{2x}$  and  $\vec{H}_1 = \vec{H}_2$ . This leads to

$$\frac{-k_{y1}}{\varepsilon_1 \vec{H}_1} = \frac{k_{y2}}{\varepsilon_2 \vec{H}_2}, \text{ resulting in: } k_{y1} \varepsilon_2 = -k_{y2} \varepsilon_1. \text{ Since the SPPs field is confined to the}$$

interface and evanescently decays in the y-direction, the conditions  $Re[k_{y1}] > 0$  and

$Re[k_{y2}] > 0$  necessitates in  $Re[\varepsilon_1] < 0$  if  $\varepsilon_2 > 0$ . For most metals and dielectrics, this

condition is satisfied in the visible and infrared wavelength range. The above analysis

describes the existence of the SPPs for the TM polarization. Next, substituting  $k_{y1}$  and

$k_{y2}$  results in SPP dispersion relation for the wave propagating in the x-direction as

$$k_x = k_0 n_{spp} = k_0 \sqrt{\frac{\varepsilon_1 \varepsilon_2}{\varepsilon_1 + \varepsilon_2}} = k_{spp} \quad \text{Eq. 2-9}$$

where  $n_{spp}$  is the refractive index of SPP. SPPs propagate at the interface of metal-

dielectric with the phase velocities below the speed of light in the dielectric medium and

it could not exist for frequencies above SPPs resonant frequency;  $\omega_{sp} = \omega_p / \sqrt{1 + \varepsilon_1}$ ,

where  $\omega_p$  is the plasma frequency of the bulk material, for silver  $\hbar\omega_p = 9.1 \text{ eV}$  [79]. In

the calculations pertaining to the SPP dispersion relation, generally, the permittivity of

the metal is assumed by the Drude Model.

### 2.1.2 The Drude Model and Dispersion Relation

The Drude Model explains the transport properties of electrons in the metal and

free carriers in heavily doped semiconductors. The model assumes a sea of constantly

jittering electrons bouncing and re-bouncing off heavier and relatively immobile positive

ions. The model gives the complex permittivity of metal as a function of frequency and it

describes how the electric field of light interacts with the free electrons in the metal

which cause them to oscillate until their motions are damped [80] [81]. The complex

permittivity of the metal is given by

$$\varepsilon_m(\omega) = \varepsilon'_m + i\varepsilon''_m = \varepsilon_\infty - \frac{\omega_p^2}{\omega(\omega + i\omega_\tau)} \quad \text{Eq. 2-10}$$

The real and imaginary parts of Drude permittivity are given as

$$\varepsilon'_m = \varepsilon_\infty - \frac{\omega_p^2}{\omega^2 + \omega_\tau^2}, \quad \varepsilon''_m = \frac{\omega_\tau \omega_p^2}{\omega(\omega^2 + \omega_\tau^2)} \quad \text{Eq. 2-12}$$

where  $\omega_p$  is the intrinsic bulk plasma frequency that lies in UV for most metals,  $\varepsilon_\infty$  is the

high frequency dielectric permittivity,  $\omega_p = \sqrt{\frac{n_e e^2}{\varepsilon_0 m_e}}$  is the plasma frequency of the free

electron gas ( $n_e$  is the number density of the electron gas;  $m_e$  is the effective mass of the

electron in the material) and  $\omega_\tau$  is the damping factor. The wave vector of SPPs at the

interface of air-silver is illustrated in **Figure 2-2**.

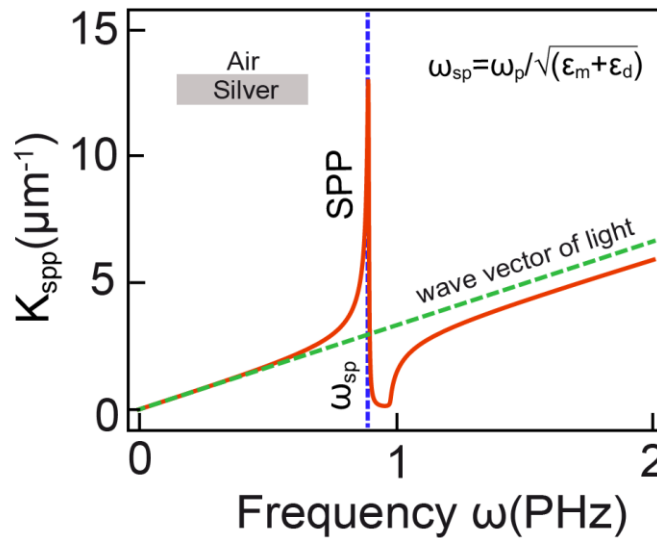


**Figure 2-2:** Wave vector of SPPs ( $k_{spp}$ ) propagating on silver/air interface (red curve). The green line represents the wave vector of light in air ( $k_0$ ), while the blue dotted line corresponds to the surface plasmon frequency  $\omega_{sp} = \omega_p / \sqrt{\varepsilon_d + \varepsilon_m}$ .

Here,  $k_{spp}$  at the interface of Air/Silver calculated using the Drude parameters given as  $\omega_\tau = 5.139$  THz,  $\omega_p = 2.186$  PHz and  $\varepsilon_\infty = 5$  [82]. From **Figure 2-2** we observe that at low frequencies, the  $k_{spp}$  (red curve) matches with that  $k_0$ . However, as

the frequency increases,  $k_{spp}$  becomes much larger than the  $k_0$ . The peak of the SPP wavevector represents the  $\omega_{sp} = \omega_p / \sqrt{\epsilon_d + \epsilon_m}$  (for silver  $\omega_{sp} = 977$  THz), below which SPPs can be excited. Since the  $k_{spp}$  is inversely related to the SPP wavelength ( $\lambda_{spp}$ ), we can observe that  $\lambda_{spp}$  is much smaller than the wavelength of light in free space ( $\lambda$ ) at the same frequency. This unique property of SPPs have led to numerous applications as described in the previous section. Also, from **Figure 2-2** we can observe a momentum mismatch between the  $k_{spp}$  and  $k_0$ . Namely, the SPP momentum  $\hbar k_{spp}$  is always greater than the momentum of light in free space  $\hbar k_0$ . To conserve the energy and momentum, we need to couple the  $k_0$  with the  $k_{spp}$  by employing special coupling mechanisms like prism or a grating coupler which are described in the preceding sections.

Wave vectors  $k_{y1}$  and  $k_{y2}$  are imaginary due to the relations  $k_0 < k_{spp}$  and  $Re[\epsilon_1] = \epsilon'_1 < 0$ , so that as described above, the field amplitude of the SPP decays exponentially as  $\exp(-|k_{y(1,2)}||y|)$ , normal to the surface. The value of the skin depth at which the field falls to  $1/e$  becomes

$$\hat{y}_2 = \frac{\lambda}{2\pi} \left( \frac{\epsilon'_1 + \epsilon_2}{\epsilon_2^2} \right)^{1/2}, \quad y > 0 \quad \text{Eq. 2-12}$$

$$\hat{y}_1 = \frac{\lambda}{2\pi} \left( \frac{\epsilon'_1 + \epsilon_2}{\epsilon_1'^2} \right)^{1/2}, \quad y < 0 \quad \text{Eq. 2-13}$$

For  $\lambda = 0.6 \mu m$ , one obtains for silver  $\hat{y}_2 = 0.39 \mu m$  and  $\hat{y}_1 = 0.024 \mu m$ , and for gold  $0.28 \mu m$  and  $0.031 \mu m$ , respectively. At large  $k_{spp}$ ,  $\hat{y}_{(1,2)}$  is given by  $1/k_{spp}$  leading to a strong confinement of the field near the interface of both media. At low  $k_{spp}$  or large  $|\epsilon'_1|$  values, the field in the air has a strong (transverse) component  $E_y$  compared to the longitudinal component  $E_x$ , namely  $E_y/E_x = -i|\epsilon'_1|^{1/2}$  and extends far into the

dielectric; it resembles a guided photon field (Zenneck-Sommerfeld wave). In the metal,  $E_y$  is small in comparison to  $E_x$  since  $E_y/E_x = i|\epsilon'_1|^{-1/2}$ . These relations are derived from  $\nabla \cdot E = 0$ , which is valid outside the surface air/metal. At large  $k_{spp}$  both components  $E_x$  and  $E_y$  become equal:  $E_y = \pm iE_x$  (air:  $+i$ , metal:  $-i$ ).

The intensity of the SPP propagating along the interface of the dielectric-metal decreases as  $e^{-2k''_{spp}x}$ . The  $l_{spp}$  (propagation length of the SPP) after which the SPP field intensity decreases to  $1/e$  is given by  $l_{spp} = (2\text{Im}[k_{spp}])^{-1}$ . In the visible region,  $l_{spp}$  reaches the value of  $22 \mu\text{m}$  in silver at  $\lambda = 0.5 \mu\text{m}$  and  $l_{spp} = 500 \mu\text{m}$  at  $\lambda = 1.06 \mu\text{m}$ . The absorbed energy at the interface of the dielectric-metal eventually heats the metal layer.

### 2.1.3 SPPs in Semiconductors

Intrinsic semiconductors can be tuned to attain diverse electric properties by doping with acceptor impurities (boron) which result in a  $P$ -type semiconductor with donor impurities (phosphorous) and will result in  $N$ -type semiconductor [80]. In  $N$ -type semiconductors, electrons are the majority carriers and the holes are the minority carriers, whereas it is the opposite in the  $P$ -type semiconductor. Doping with  $N$ -type impurities can result in obtaining optical properties similar to metal. Like metals, when the light is incident on the  $N$ -type semiconductor, it can excite collective electron oscillation and can generate SPPs. Similar to metals, the optical response of highly doped degenerate semiconductors can be characterized by the Drude Model with permittivity given as  $\epsilon(\omega) = \epsilon_b - \omega_p^2(n, T)/(\omega^2 + i\omega\omega_\tau(n))$ , where the bound electron permittivities are  $\epsilon_b = 11.6$  for Si,  $12.6$  for GaAs and  $13.9$  for  $\text{In}_{0.53}\text{Ga}_{0.47}\text{As}$  [83]. An important difference to note is that both the plasma frequency,  $\omega_p = e\sqrt{n(T)/\epsilon_0 m_e}$ , and relaxation rate,  $\omega_\tau =$

$e/m_e\mu(n, T)$ , now depend on the doping concentrations and local temperature, where  $n$  is the electron doping concentration,  $e$  is the electron charge,  $\epsilon_0$  is the permittivity of free space,  $m_e$  is the effective electron mass, and  $\mu$  is the mobility of electrons. For the semiconductor materials considered in this dissertation: n-GaAs, n-Si and n-In<sub>0.53</sub>Ga<sub>0.47</sub>As the effective mass is by given as  $m_{e(GaAs)} = 0.067 \times m_0$  [84],  $m_{e(Si)} = 0.26 \times m_0$  [84] and  $m_{e(In_{0.53}Ga_{0.47}As)} = 0.041 \times m_0$  [85], where  $m_0$  is the mass of the electron.

Doping dependence of  $\omega_p$  and  $\omega_\tau$  allows for fine tuning of the optical properties of the doped semiconductors at far-infrared and THz frequencies. **Figure 2-3 (a)** shows the plasma frequency for n-GaAs, n-Si and n-In<sub>0.53</sub>Ga<sub>0.47</sub>As calculated as the function of the doping concentration.

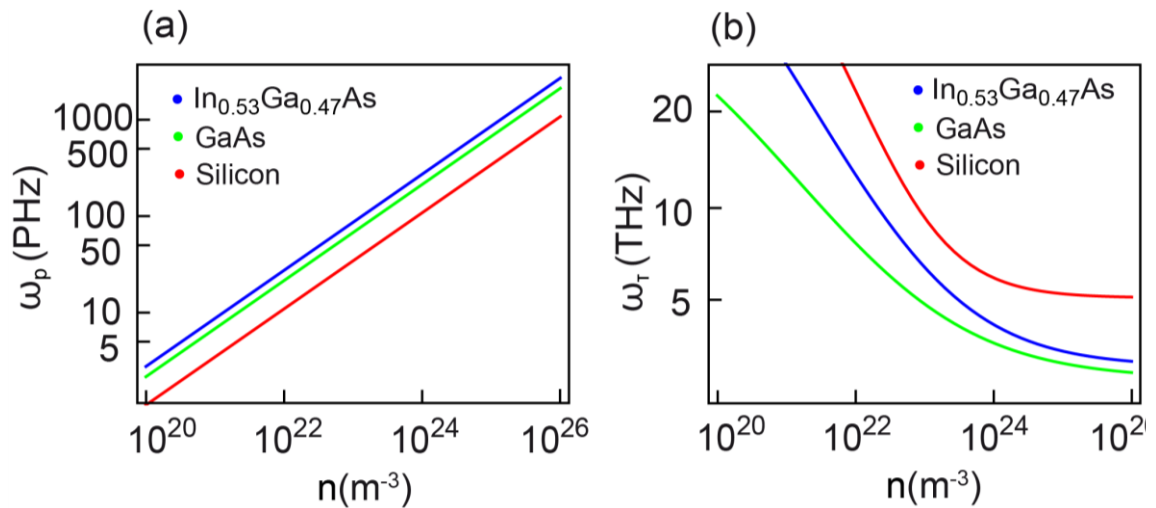


**Figure 2-3:** (a) Plasma frequencies versus the doping concentration. (b) Relaxation frequencies versus the doping concentration. The blue line is n-In<sub>0.53</sub>Ga<sub>0.47</sub>As, the green line is n-GaAs and the red line is n-Si.

Here, we can observe that the plasma frequency is a strong function of doping concentration and increases with the doping. The n-In<sub>0.53</sub>Ga<sub>0.47</sub>As, which is represented by the red line, has higher plasma frequency compared to n-Si and n-GaAs. This is

because of the direct consequence of the smaller effective mass of electrons in n- $\text{In}_{0.53}\text{Ga}_{0.47}\text{As}$ . Similarly, **Figure 2-3 (b)** shows the effect of doping on the damping frequency  $\omega_\tau$ . We can clearly observe that higher  $\omega_\tau$  is a strong function of  $\mu$ : higher the  $\mu$  lower the damping of the electron oscillation. This is because  $\mu$  has a strong dependency on doping concentration [86] [87] [88].

#### 2.1.4 SPP Dispersion Relation-Multilayer System

In this section, we study the dispersion relation of the SPPs in a multilayer geometry consisting of alternating, conducting and dielectric thin films. In such systems, both the interfaces can sustain individual bound SPPs. Also, if the thickness of the middle layer is comparable or smaller than the decay length (**Eq. 2-12** and **Eq. 2-13**) of the interface mode. The interactions between the bound SPPs will result in coupled modes.

**Figure 2-4** depicts the multilayer geometry under consideration.



**Figure 2-4:** Geometry of a three-layer system consisting of a thin layer (2) with permittivity  $\epsilon_2$  is sandwiched between two infinite half spaces (1) and (3).

To investigate the properties of the coupled modes for the multilayer geometry shown in **Figure 2-4**, first, it is assumed that SPPs propagate along the  $x$ -direction and there is no spatial variation along the  $y$ -direction.

$$H_y(z) = e^{-i\beta z} \begin{cases} H_1 e^{-k_1 z}, & z > \frac{a}{2} \\ H_2^- e^{-k_2 z} + H_2^+ e^{k_2 z}, & -\frac{a}{2} < z < \frac{a}{2} \\ H_3 e^{k_3 z}, & z < -\frac{a}{2} \end{cases} \quad \text{Eq. 2-14}$$

$$E_x(z) = e^{-i\beta z} \begin{cases} iH_1 k_1 e^{-k_1 z} \frac{1}{\omega \varepsilon_0 \varepsilon_1}, & z > \frac{a}{2} \\ (iH_2^- k_2 e^{-k_2 z} - iH_2^+ k_2 e^{k_2 z}) \frac{1}{\omega \varepsilon_0 \varepsilon_2}, & -\frac{a}{2} < z < \frac{a}{2} \\ iH_3 k_3 e^{-k_3 z} \frac{1}{\omega \varepsilon_0 \varepsilon_3}, & z < -\frac{a}{2} \end{cases} \quad \text{Eq. 2-15}$$

Continuity condition for a p-polarized wave:  $H_{1,y} = H_{2,y}$  and  $\frac{1}{\varepsilon_1} \frac{\partial H_{1,y}}{\partial z} = \frac{1}{\varepsilon_2} \frac{\partial H_{2,y}}{\partial z}$ .

Applying the above continuity condition at the interfaces,  $z = \frac{a}{2}$  and  $z = -\frac{a}{2}$  results in

Boundary 1-2 ( $z = \frac{a}{2}$ )

$$H_1 e^{-k_1 \frac{a}{2}} = H_2^- e^{-k_2 \frac{a}{2}} + H_2^+ e^{k_2 \frac{a}{2}} \quad \text{Eq. 2-16}$$

$$\frac{k_1}{\varepsilon_1} H_1 e^{-k_1 \frac{a}{2}} = \frac{k_2}{\varepsilon_2} H_2^- e^{-k_2 \frac{a}{2}} - \frac{k_2}{\varepsilon_2} H_2^+ e^{k_2 \frac{a}{2}} \quad \text{Eq. 2-17}$$

Boundary 2-3 ( $z = -\frac{a}{2}$ )

$$H_1 e^{-k_1 \frac{a}{2}} = H_2^- e^{-k_2 \frac{a}{2}} + H_2^+ e^{k_2 \frac{a}{2}} \quad \text{Eq. 2-18}$$

$$\frac{k_3}{\varepsilon_3} H_3 e^{-k_3 \frac{a}{2}} = \frac{k_2}{\varepsilon_2} H_2^- e^{-k_2 \frac{a}{2}} - \frac{k_2}{\varepsilon_2} H_2^+ e^{k_2 \frac{a}{2}} \quad \text{Eq. 2-19}$$

Let us substitute  $R_i = \frac{k_i}{\varepsilon_i}$  and substitute **Eq. 2-16** in **Eq. 2-17**; **Eq. 2-18** in **Eq. 2-19** and

multiply by  $e^{k_2 \frac{a}{2}}$

$$R_1 (H_2^- + H_2^+ e^{k_2 a}) = R_2 (H_2^- - H_2^+ e^{k_2 a}) \quad \text{Eq. 2-20}$$

$$R_3 (H_2^+ + H_2^- e^{k_2 a}) = R_2 (H_2^+ - H_2^- e^{k_2 a}) \quad \text{Eq. 2-21}$$

The original system of four variables is now reduced to two

$$e^{2ak_2} = \frac{(R_1 - R_2)(R_3 - R_2)}{(R_1 + R_2)(R_3 + R_2)} \quad \text{Eq. 2-22}$$

$$e^{2ak_2} = \frac{(k_1/\varepsilon_1 - k_2/\varepsilon_2)(k_3/\varepsilon_3 - k_2/\varepsilon_2)}{(k_1/\varepsilon_1 + k_2/\varepsilon_2)(k_3/\varepsilon_3 + k_2/\varepsilon_2)} \quad \text{Eq. 2-23}$$

where  $\varepsilon_1$ ,  $\varepsilon_2$ , and  $\varepsilon_3$  are the dielectric permittivity's of the three mediums,  $a$  is the

thickness of the middle layer, and  $k_l = \sqrt{k_{spp}^2 - \varepsilon_l k_0^2}$  are the transversal SPP

wavevectors in the three layers  $l \in \{1,2,3\}$ .

### 2.1.5 Propagation Properties of SPP

Previous sections describe the basics of the SPPs. In this section, we talk about the propagation properties of SPPs. Two critical parameters that determine mode characteristics of SPPs are the  $l_{spp} = (2k_x'')^{-1} = \lambda/(4\pi n_{spp}'')$  and the normalized mode area  $A$ , defined as [11]

$$A = \frac{A_m}{A_0} = \frac{\iint_{-\infty}^{\infty} W(x, y) dx dy}{\max[W(x, y)]} \times \frac{1}{A_0} \quad \text{Eq. 2-24}$$

where  $\lambda$  is the operating wavelength,  $n_{spp}''$  is the imaginary part of the SPP effective refractive index,  $A_m$  is the mode area,  $A_0 = \lambda^2/4$  is the diffraction limited mode area, and the energy density  $W(x, y)$  is defined as

$$W(x, y) = \frac{1}{2} Re \left\{ \frac{d[\omega \varepsilon(x, y)]}{d\omega} \right\} |E(x, y)|^2 + \frac{1}{2} \mu_0 |H(x, y)|^2 \quad \text{Eq. 2-25}$$

where  $E(x, y)$  and  $H(x, y)$  are the electric and magnetic fields, respectively. From **Eq.**

**2-24** and **Eq. 2-25**. we can deduce that a larger value of  $A$  corresponds to a lower degree of mode confinement. Hence, there is a need for the trade-off. For device geometry shown in **Figure 2-4**, both asymmetric mode (SM) and asymmetric mode (ASM) of SPPs can be possible. For a metal insulator metal (MIM) waveguide, for the fundamental

ASM, it is shown to have a critical cut-off thickness for the central dielectric layer which is equal to  $\pi c/\omega\sqrt{\epsilon_1}$  [89], while the fundamental SM does not exhibit the cutoff thickness for the central dielectric layer. In other words, the field of an SM can be confined into a central dielectric region with an arbitrarily small thickness, indicating it can provide a very high level of confinement ( $A\sim\lambda^2/500$ ), which was demonstrated in [28]. It is far beyond the diffraction limit. However, such strong mode confinement is achieved at the cost of the propagation length, which is in the order of a few micrometers ( $l_{spp}\sim 10\ \mu m$  [90]).

The propagation length for the long-range SPP (LRSPPs) mode can be up to a few centimeters ( $l_{spp}\sim 20\ mm$  [15]). Such large  $l_{spp}$  is accompanied by a very poor mode confinement (here, the mode area is comparable to that of the optical fiber mode [90]). Also, it has been demonstrated that a dielectric loaded SPP (DLSPPs) can provide a modest mode confinement ( $A\sim 0.16\ \lambda^2$ ) [91] as well as a fairly good propagation length ( $l_{spp}\sim 100\ \mu m$ ) [91].

#### 2.1.6 SPP Excitation Methods

As described above, to compensate for the momentum mismatch between  $k_0$  and the  $k_{spp}$  at the metal-dielectric interface, we need special mechanisms to couple the incident light to the SPP. Special excitation techniques are employed for launching SPP, for example, prism coupling [92], grating coupling [93], near field excitation [94], and highly focused laser beam excitation [95]. Here, we present the two most popular techniques, prism coupling and grating coupling [76].

### 2.1.6.1 Grating Coupling

Metal gratings can be used to compensate the wavevector mismatch between incident light and SPPs. **Figure 2-5** depicts a grating coupler with a period of  $\Lambda$ , with air as the surrounding dielectric ( $\epsilon_2 = 1$ ). When a light with wave vector  $k_0$  hits the metal grating at an incident angle  $\theta_0$ , its surface component can have two wave vectors;  $k_0 \sin \theta_0 \pm m\left(\frac{2\pi}{\Lambda}\right)$ , where  $m$  is an integer ( $m = 1, 2, 3 \dots$ ). The dispersion relation **Eq. 2-9** can then be fulfilled by

$$k_{spp} = k_0 \sin \theta_0 \pm m \left( \frac{2\pi}{\Lambda} \right) = k_0 \sqrt{\frac{\epsilon_1 \epsilon_2}{\epsilon_1 + \epsilon_2}} \quad \text{Eq. 2-26}$$

The incident light can be coupled to an SPP mode when  $m\left(\frac{2\pi}{\Lambda}\right)$  equals to the wavevector mismatch ( $\Delta k = k_{spp} - k_0$ ). In addition, it should be noted that the reverse process can also take place: SPPs propagating along the grating can reduce their wave vector  $k_{spp}$  by  $\Delta k$  so that the SPPs can be decoupled and transformed into light.

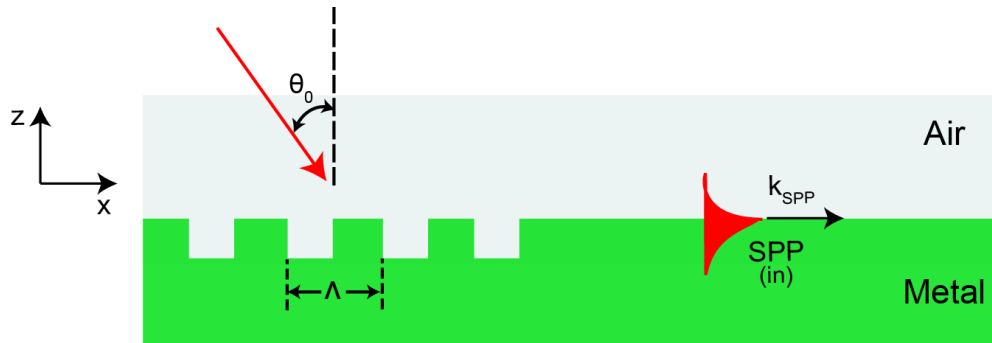


**Figure 2-5:** Grating coupler: Matching incident light to SPP wavevector.

### 2.1.6.2 Prism/ATR Coupling

SPPs can be coupled in a three-layer system consisting of a thin metal film sandwiched between two insulators of different dielectric constants. For simplicity, here

we consider air as one of the dielectric layers ( $\epsilon_1 = 1$ ) and prism with higher dielectric constant ( $\epsilon_2 > 1$ ). A beam reflected at the interface between the prism (see **Figure 2-7**), and the metal will have an in-plane momentum  $k_x = k_0\sqrt{\epsilon_2} \sin \theta_0$ , which is sufficient to excite SPPs at the interface between the metal and the lower-index dielectric, i.e. in this case at the metal/air interface. This way, SPPs with propagation constants  $k_{spp}$  between the light lines of air and the higher-index dielectric can be excited (see **Figure 2-6**). SPP excitation manifests as a minimum in the reflected beam intensity. Here, phase-matching to SPPs at the prism/metal interface cannot be achieved as the respective SPP dispersion line lies outside the prism light cone (see **Figure 2-6**).

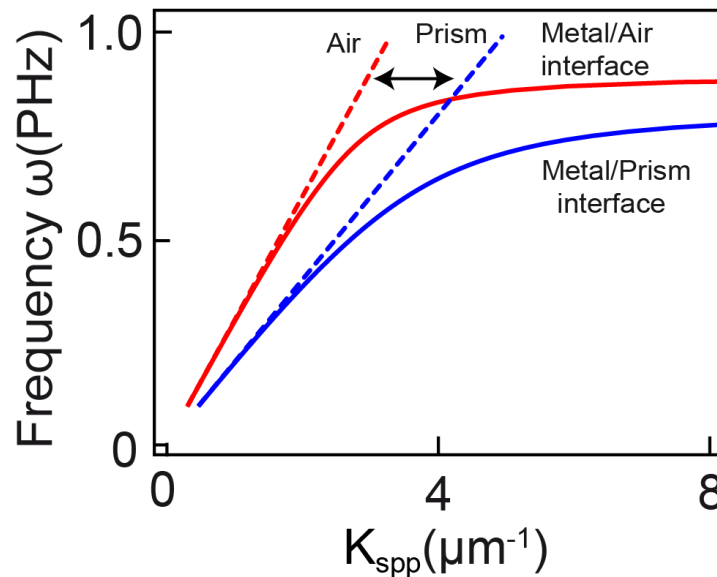


**Figure 2-6:** Prism coupling and SPP dispersion. Propagation constants between the light lines of air and the prism are accessible, resulting in additional SPP damping due to the leakage radiation into the latter; the excited SPPs have propagation constants inside the prism light cone.

The above-described coupling system is also known as attenuated total internal reflection (ATR) -involving the tunneling of the fields of the excitation beam to the

metal/air interface where SPP excitation takes place. Two different geometries for prism coupling are possible, depicted in **Figure 2-7**. The most common configuration is the Kretschmann Method [96], in which a thin metal film is evaporated on top of a glass prism. Photons from a beam impinging from the glass side at an angle greater than the critical angle of total internal reflection tunnel through the metal film and excite SPPs at the metal/air interface. Another geometry is the Otto configuration [97], in which the prism is separated from the metal film by a thin air gap. Total internal reflection takes place at the prism/air interface, exciting SPPs via tunneling to the air/metal interface. Also, excitation of SPPs using a prism can be termed as the evanescent wave coupling mechanism.

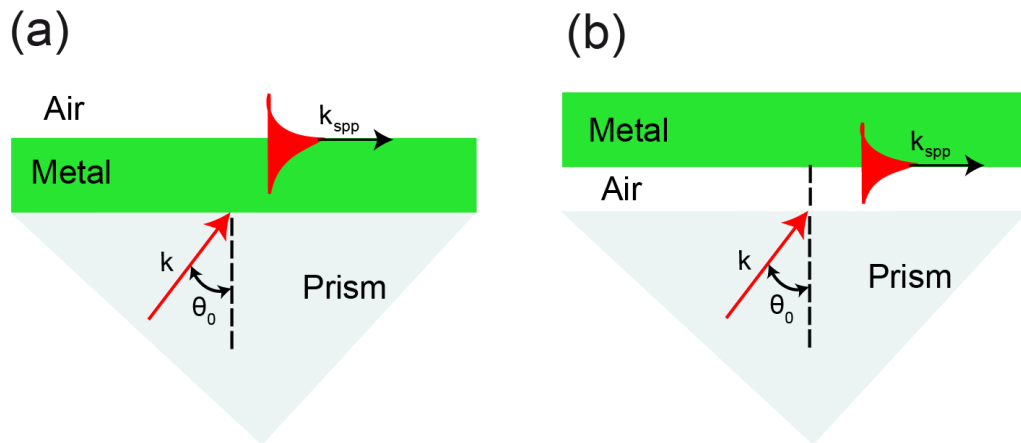


**Figure 2-7:** Prism coupling to excite SPPs using the attenuated total internal reflection in the (a) Kretschmann and (b) Otto configurations.

## CHAPTER 3

### ACTIVE CONTROL OF CHARGE DENSITY WAVES AT DEGENERATE SEMICONDUCTOR INTERFACES

The field of plasmonics has experienced a renaissance in recent years by providing a large variety of new physical effects and applications. Surface plasmon polaritons, i.e. the collective electron oscillations at the interface of a metal/semiconductor and a dielectric, may bridge the gap between electronic and photonic devices, provided a fast switching mechanism is identified. In this chapter, we demonstrate a surface plasmon-polariton diode (SPPD), an optoelectronic switch that can operate at exceedingly large signal modulation rates. The SPPD is built by using heavily doped  $PN^+$ -junction where surface plasmon polaritons propagate at the interface between  $N$  and  $P$ -type semiconductor layers and can be switched by an external voltage.

Furthermore, we also present a comprehensive multi-physics study of the complex phenomena behind the SPPD operation and discuss the numerical framework developed to self-consistently solve the Maxwell's, Poisson-Boltzmann, drift-diffusion, and heat equations. This model allows for accurate simulations of the excitation and electro-optical control of the SPPs, the minority carrier transport across the  $PN^+$ -junction, the spatially and time-dependent local permittivity variations under external bias, and the introduction of thermal effects due to Ohmic heating and electromagnetic energy dissipation. Combined with the use of two Figures of Merits (FOMs), we

specifically perform studies to identify the best semiconductor material among Silicon, lattice matched Indium Gallium Arsenide ( $\text{In}_{0.53}\text{Ga}_{0.47}\text{As}$ ) and GaAs that can offer SPPD operation with low loss, high tunability and extreme mode confinement which could potentially lead to smaller and low dissipation optoelectronic devices with high signal modulation. We also study the operation characteristics, transmission modulation of the SPPD. In addition, we also present the possible optoelectronic logic gates using the SPPD as an impute waveguide.

Most importantly, in the current study, we consider the constraints imposed by the present micro and nanomanufacturing technology by using realistic doping concentrations and electromagnetic frequency range of operation that is accessible through experimentation, specifically using  $\text{CO}_2$  or quantum cascade lasers (QCL) [102] [70].

### 3.1 Surface Plasmon Polariton Diode

Basic schematic of the SPPD is shown in **Figure 3-1**. It consists of a  $PN^+$  - junction made of highly doped (degenerate) semiconductor with an active drift-diffusion region formed between two control electrodes. When a forward bias is applied across the device, minority carriers (electrons) are injected in the  $P$ - doped layer altering its dielectric constant  $\epsilon_p$ . For applied voltage higher than a critical value  $V > V_c$ , the  $P$ - layer acquires a metal like characteristics impeding the propagation of the SPP across the active region and establishing the OFF state of the device. For a given operation frequency  $\omega$ , the critical voltage can be obtained from the transparency condition  $\omega = \omega_p(V_c)/\sqrt{\epsilon_b}$  (or  $\epsilon_p(\omega, V_c) = 0$ ), and the carrier balance equation  $n = n_c \approx n_0 e^{V_c/V_T}$ , giving

$$V_c = V_T \ln \left[ \frac{\epsilon_b \omega^2}{\omega_{p0}^2} \right] \quad \text{Eq. 3-1}$$

where  $\omega_{p0} = qn_i(T)/\sqrt{\epsilon_b m_e N_A}$  is the renormalized plasma frequency of the minority carriers under thermal equilibrium,  $m_e$  is the electrons effective mass in the  $P$ -layer,  $\epsilon_b$  is the contribution of the lattice electrons to the semiconductor permittivity,  $V_T = k_B T/q = 0.026V$  is the thermal voltage,  $n_0 = n_i^2/N_A$  where  $n_i$  is the intrinsic concentration and  $N_A$  is the acceptor doping concentration. In all calculations that follows, the SPPD geometric characteristics are fixed with the  $P$ -layer having a thickness of  $d = 1.5 \mu m$  and the overall length of the active drift-diffusion region is  $w = 4 \mu m$ . The SPPD can be designed using a large variety of semiconductor materials.

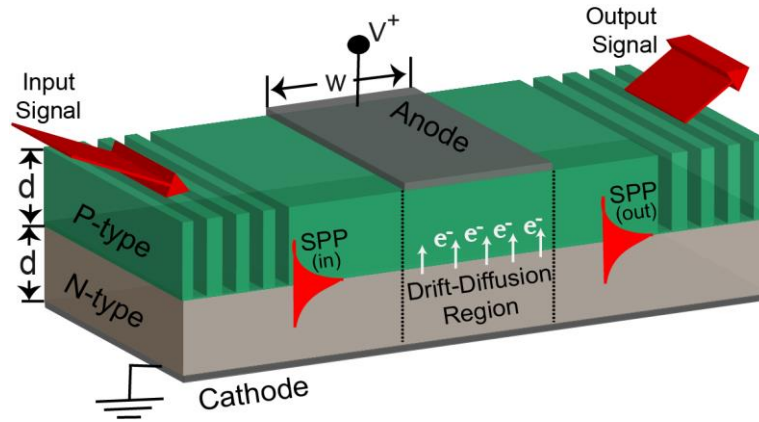


**Figure 3-1:** Basic schematic of a Surface Plasmon Polariton Diode (SPPD).

### 3.2 Thermo-electro-optical Model

Since the SPPD switching is due to injection of minority carriers in the presence of an external forward bias voltage, the flow of charge carriers is expected to result in Ohmic heating and a corresponding increase of metallurgical junction temperature. The

junction temperature is additionally influenced by the electromagnetic energy dissipation of the SPP. To have a proper understanding of the complex Multiphysics processes governing the SPPD operation, a self-consistent thermo-electro-optic model is developed. A finite difference integrated circuits COMSOL Semiconductor Module (CSM) is implemented to obtain the minority carriers distribution across the device, which is then used to extract the inhomogeneous dielectric function of the *P*-layer. Full-wave finite difference (FD) calculations of the SPPD electromagnetic response are then performed using the COMSOL Electromagnetic Module (CEM) (see **Figure 3-2**). As we see in the proceeding sections of this chapter, the SPPD response is also sensitive to the thermal effects due to Ohmic heating which is accounted for by the COMSOL Heat Transfer Module (CHTM). A seamless integration between the three physical modules is accomplished by developing a MATLAB based facilitator code which shares the inter-dependent physics parameters between the separate modules and allows for self-consistent steady-state and time-dependent simulations.

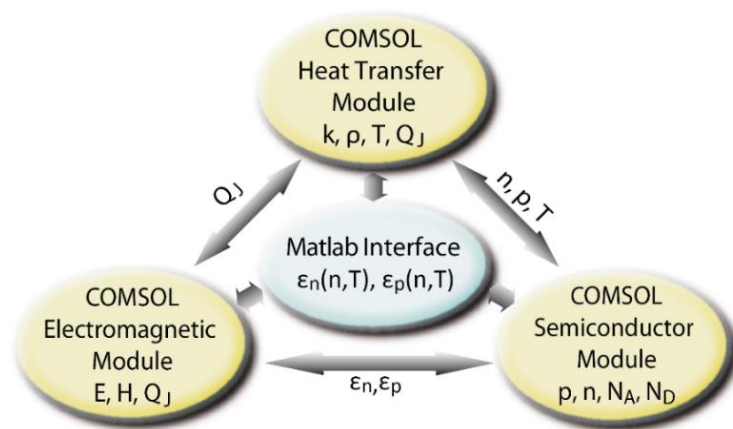


**Figure 3-2:** Self Consistent thermo-electro-optic model.

### 3.3 The figure of Merit of SPPD

The operation of the SPPD depends on a large set of parameters including donor and acceptor doping, temperature, applied bias, semiconductor materials, and device geometry. In this study, we focus on silicon (Si), lattice matched Indium Gallium Arsenide ( $\text{In}_{0.53}\text{Ga}_{0.47}\text{As}$ ) and Gallium Arsenide (GaAs) based devices. These semiconductors are excellent candidates due to well-established manufacturing protocols at high (degenerate) doping levels and as shown next, these materials can also provide superior SPP characteristics. As described in **Chapter 2**, the SPPs at the metal-semiconductor interfaces have wavelengths substantially shorter compared to those in the adjacent dielectric media. However, with the increased confinement/localization, there is a corresponding increase in propagation losses, thus for a practical application, a positive trade-off must be achieved between these two characteristics. To address this issue and provide a roadmap toward practically feasible SPPD, we introduce two figures of merit (FOM) to quantify the SPP localization and propagation characteristics.

$$\begin{aligned}
 FOM_1 &= \left| \frac{\text{Re}[k_{SPP}(\omega, N_D, N_A)]}{\text{Re}[k_P(\omega, N_A)]} \right| \\
 FOM_2 &= \left| \frac{\text{Re}[k_{SPP}(\omega, N_D, N_A)] - \text{Re}[k_P(\omega, N_A)]}{\text{Im}[k_{SPP}(\omega, N_D, N_A)]} \right|
 \end{aligned}
 \tag{Eq. 3-2}$$

The  $FOM_1$  is defined as the ratio of the SPP wavevector  $k_{SPP}$  to the wavevector  $k_P$  of bulk waves propagating in the lightly  $P$ -doped layer (the dielectric layer) and is a measure of how much smaller in size the SPPD can be compared to conventional optical devices. The  $FOM_2$  describes both the SPPs localization and dissipation losses.

An optimal SPPD design is determined by the parametric range where the two figures of merit are large. The FOMs for Si,  $\text{In}_{0.53}\text{Ga}_{0.47}\text{As}$ , and GaAs are calculated for practically feasible doping and frequency ranges as shown in **Figure 3-3**. As expected,

our parametric studies show that the SPPD can be formed with minimal physical sizes if the operational frequency is close to the surface plasmon frequency  $\omega_{sp} \sim \sqrt{N_D}$ . The lateral size of the SPPD can be a factor of two (in the case of Si) and a factor of four (in the case of  $\text{In}_{0.53}\text{Ga}_{0.47}\text{As}$  and GaAs) smaller than that of dielectric devices. However, at the surface plasmon frequency, the SPP are highly attenuated. Hence, operation at lower frequencies should be considered as shown by the second figure of merit so that positive tradeoff between localization and propagation losses is achieved. The data clearly demonstrates that SPPD based on  $\text{In}_{0.53}\text{Ga}_{0.47}\text{As}$  is expected to manifest both small device sizes and propagation length that is more than 100 times larger compared to the free space wavelength. In what follows, we fix the operation wavelength at 30 THz (corresponding to the free space wavelength of 10microns) and adjust the doping concentration accordingly so that an optimal operation is achieved. It must be also noted that in the performed parametric studies we have considered a range of doping concentrations consistent with experimentally attainable values for Si ( $N_D \leq 4 \times 10^{26} m^{-3}$ ),  $\text{In}_{0.53}\text{Ga}_{0.47}\text{As}$  ( $N_D \leq 8 \times 10^{25} m^{-3}$ ) [103] and GaAs ( $N_D \leq 6 \times 10^{25} m^{-3}$ ).

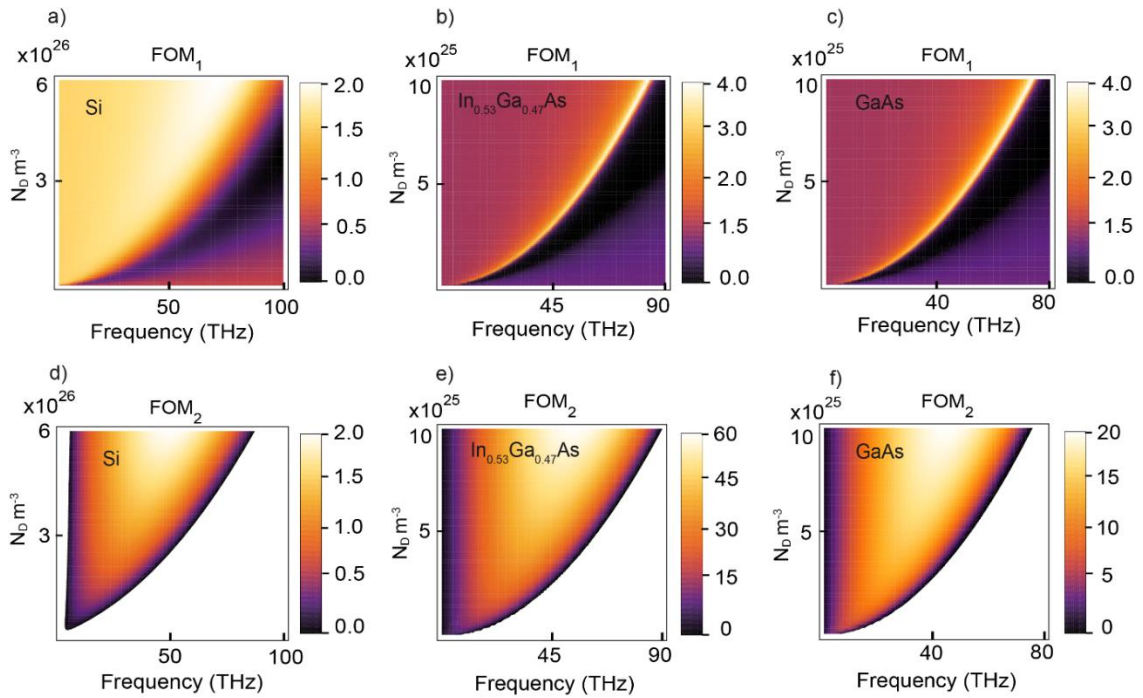


**Figure 3-3:** The Surface Plasmon Polaritons (SPPs) Figures of Merit (FOM) vs. frequency and doping for (a,b,c) Si and (d,e,f) In<sub>0.53</sub>Ga<sub>0.47</sub>As.

### 3.4 SPPD Operational Characteristics

#### 3.4.1 Steady State Analysis

Using the numerical model, we begin our study of the SPPD input-output characteristics by first considering the steady-state case. The signal modulation of the device is described as the logarithmic ratio of the output/input SPP power densities,  $m_p = 10\log_{10}(P_{out}/P_{in})$ . As identified above, a rapid decrease in power transmission is expected for forward bias larger than the critical  $V > V_c$ , for which the *P*-doped layer acquires metal-like characteristics. Indeed, with an increase in the applied voltage, the SPP dispersion is rapidly modified as seen in **Figure 3-4 (a-c)**.

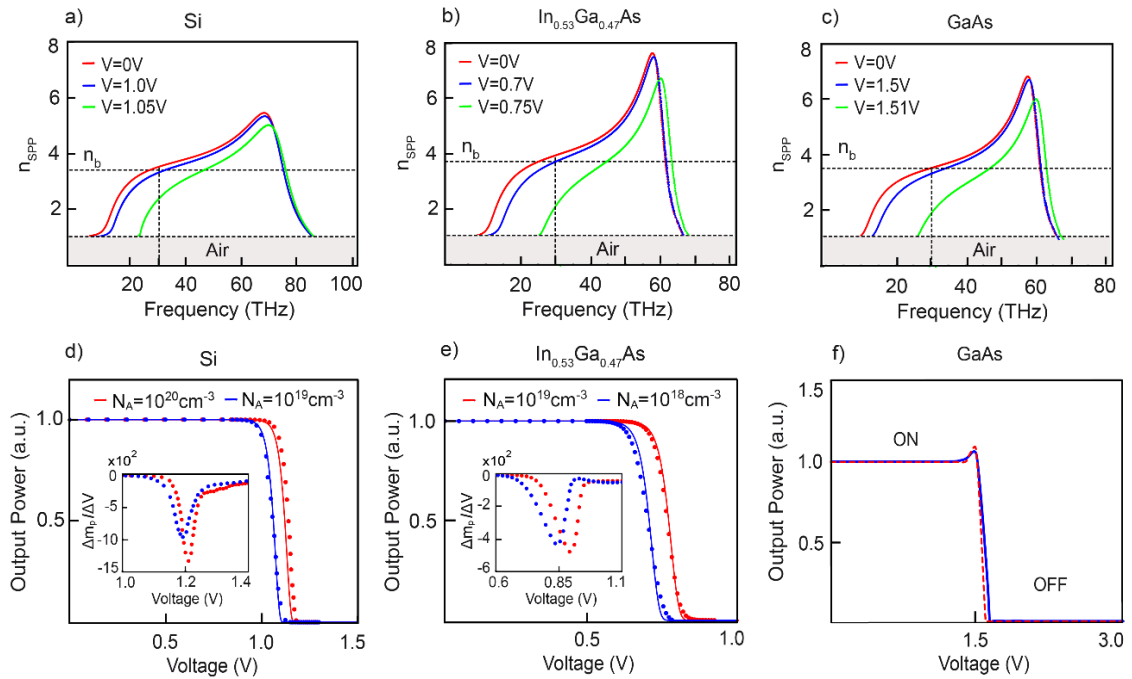


**Figure 3-4:** The SPPs dispersion at different external bias voltages for (a) Si with doping concentrations;  $N_A = 1 \times 10^{20}$ ,  $N_D = 4 \times 10^{20} cm^{-3}$  (b) In<sub>0.53</sub>Ga<sub>0.47</sub>As with  $N_A = 1 \times 10^{19}$ ,  $N_D = 5 \times 10^{19} cm^{-3}$  and GaAs with  $N_A = 5 \times 10^{19}$ ,  $N_D = 5 \times 10^{19} cm^{-3}$ . The SPPD transmittance for (d) Si (e) In<sub>0.53</sub>Ga<sub>0.47</sub>As and (f) GaAs, for different  $P$ -doping concentrations, are obtained using the self-consistent Multiphysics model (dots, dashed) and compared to the WKB approximation (solid lines). The corresponding responsivities are shown as inserts of (d, e). In the calculations the operation frequency is set at 30 THz, the thickness of the  $P$ -type layer is  $d = 1.5 \mu m$ ,  $n_b$  identifies the refractive index of  $P$ -layer and the overall length of the active drift-diffusion region is fixed at  $w = 4 \mu m$ .

For fixed operation frequency  $f_o = \omega_o/2\pi = 30$  THz and zero applied bias, the SPPs can travel across the device which is exemplified by the fact that the effective refractive index  $n_{SPP}$  of these surface modes is larger than the refractive index  $n_p$  of the  $P$ -doped layer. As the applied voltage approached the critical, the SPP dispersion curve is shifted and a refractive index mismatch between SPPs in the drift diffusion region  $n_{SPP}(\omega_o, V)$  and in the rest of the device  $n_{SPP}(\omega_o, V = 0)$  is observed. This immediately leads to reflection and signal attenuation at the active zone establishing the OFF-state. The actual modulation of the SPP signal is shown in **Figure 3-4 (d-f)**. Signal modulations

surpassing  $m_p > -20$  dB are observed for applied bias above the critical, and responsivities are in excess of  $\Delta m_p/\Delta V > -1000$  dB  $\cdot$  V<sup>-1</sup> for Si,  $\Delta m_p/\Delta V > -500$  dB  $\cdot$  V<sup>-1</sup> for In<sub>0.53</sub>Ga<sub>0.47</sub>As and  $\Delta m_p/\Delta V > -800$  dB  $\cdot$  V<sup>-1</sup> for GaAs are demonstrated (see inserts in **Figure 3-4 (d, e)**). Generally, an increase in acceptor doping concentration ( $N_A$ ) leads to larger responsivity. These results are orders of magnitudes higher compared to the competing optoelectronic devices studied in the literature [14] [13] [51] [104-106], attesting to the SPPD potential as a high-quality switch.

The SPPD switching can be described using the Wentzel-Kramers-Brillouin (WKB) method [100], which when implemented for the SPP transmittance across the drift-diffusion region gives

$$T(V) = \left| e^{i \int_0^w k_{spp}(x,V) dx} \right|^2 \approx e^{-2w \text{Im}[k_{spp}(V)]} \quad \text{Eq. 3-3}$$

where  $w$  is the length of the active drift-diffusion region (corresponding roughly to the length of the top electrode), and the SPP wave vector  $k_{spp}$ , which is generally position and voltage dependent due to the spatially inhomogeneous minority carrier concentration in the  $P$ -type layer. Under steady state conditions, the SPP wave vector in the drift-diffusion zone can be assumed to be spatially homogeneous and dependent only on the applied voltage ( $k_{spp}(x, V) \approx k_{spp}(V)$ ). As a result, the WKB approximation gives an explicit analytical formulation of the SPP transmission across the device. For a given frequency of operation  $\omega$  and sufficiently low minority carrier concentration, we have  $k_{spp} \in \mathbb{R}$  and  $T \approx 1$ . For  $V > V_c$ , the permittivity of the  $p$ -doped layer becomes negative ( $\epsilon_p(\omega) < 0$ ) and the SPP wave vector is complex quantity ( $k_{SPP} \approx i \left( \frac{\omega p_0}{c} \right) e^{\frac{V}{2V_T}} \in \mathbb{C}$ ). Consequently, the transmittance exponentially decreases with an increase in the applied

voltage (see solid line in **Figure 3-4(d-f)**). Also, as seen in **Figure 3-4(d-f)**, numerical data is compared to the analytical theory showing a remarkable correlation between the two results.

### 3.4.2 SPPD-Numerical Simulations

**Figure 3-5** depicts snapshots of the minority carrier concentration, SPP local field profiles and temperature distributions across the device.

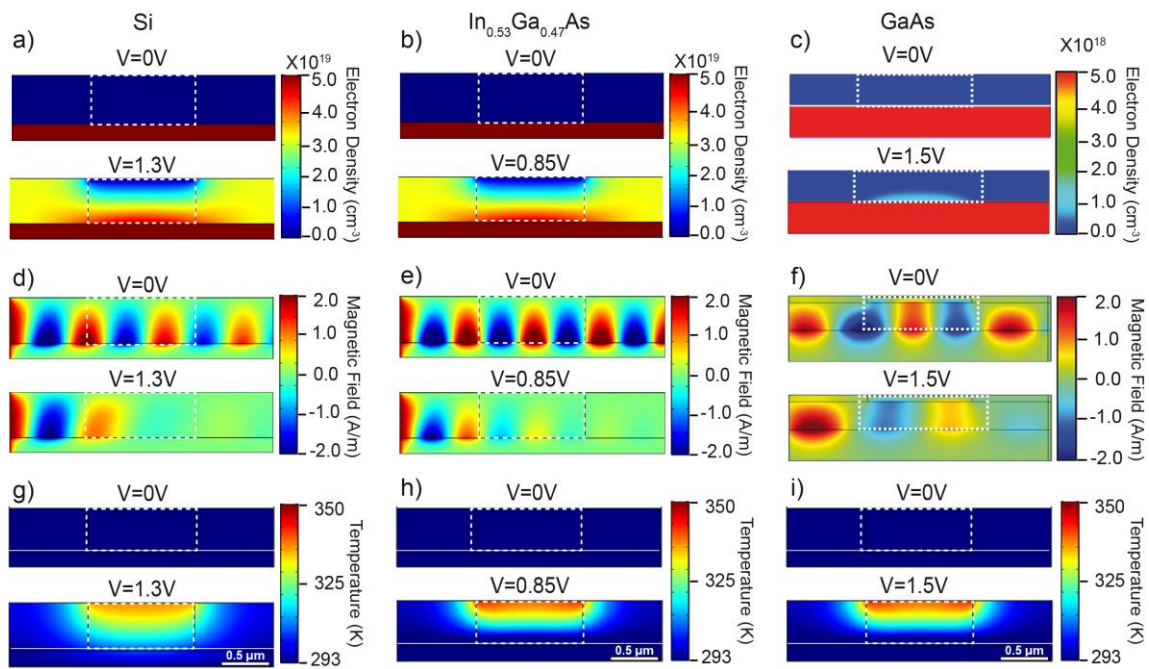


**Figure 3-5:** (a, b, c) Steady-state minority carrier concentration profiles at different applied voltages. (d, e, f) SPP propagation along the length of the device. (g, h, i) Local temperature profile. In the calculations the operation frequency is set at 30 THz, the thickness of the  $P$ -type layer is  $d = 1.5\mu\text{m}$  and the length of the active drift-diffusion region is fixed at  $w = 4\mu\text{m}$ .

For zero external voltage bias, the  $P$ -doped layer is devoid of minority carriers and the SPP modes propagate freely at the  $PN^+$ -junction interface. Close observation of the SPP local field profiles validates the fact that stronger modal localization is achieved for SPPD based on the lattice-matched  $\text{In}_{0.53}\text{Ga}_{0.47}\text{As}$ . As the external bias voltage

approach/surpass the critical, exponential increase in the minority carrier concentration is observed within the device's active region. This results in alteration of the refractive index of the *P*-doped layer leading to reflection and attenuation of SPP modes and the establishment of the OFF-state. Furthermore, the flow of charge carriers increases the device temperature due to Ohmic heating (see **Figure 3-5(g-i)**).

Interestingly, it is evident that minor changes in the electron concentration in close proximity to the metallurgic junction can result in rapid switching of the SPP. This is due to the localized nature of the SPP: these modes are confined to the  $PN^+$  - junction and slight modification of the electron density near the junction can lead to drastic changes in the SPP propagation characteristics as has been already demonstrated in **Figure 3-5(a-c)**. Furthermore, the higher local temperatures observed in proximity to the top electrode can be attributed due to two different processes.

First, the local current density achieves maximum values near the anode (which acts as a sink), and second, the integrated convective heat transfer is higher at the position of the cathode (predominantly due to the larger surface area). From the data, it is also evident that the  $\text{In}_{0.53}\text{Ga}_{0.47}\text{As}$  device switches at lower applied voltages as compared to Si and GaAs device. This is due to the fact that the critical voltage  $V_c$  increases logarithmically with the electron's effective mass, which for Si is six times and GaAs is 0.6 times higher than for  $\text{In}_{0.53}\text{Ga}_{0.47}\text{As}$ .

### 3.4.3 SPPD-Step Response

A major interest in plasmonic-based optoelectronic switching can be attributed to their perceived fast temporal response [13] [107] [53] [54] [55]. Here, we study the speed at which the optical properties of the *P*-layer switches between dielectric ( $\epsilon_p > 0$ ) to

metallic ( $\epsilon_p < 0$ ) and vice-versa. The switching rate depends on the applied bias and doping concentrations and can be obtained from time-dependent calculations of the minority concentration and the corresponding SPPD propagation characteristics. To assess the response times of the SPPD, we have performed a transient analysis under step-type input voltage bias. Our results for sets of acceptor concentrations are shown in

**Figure 3-6.**

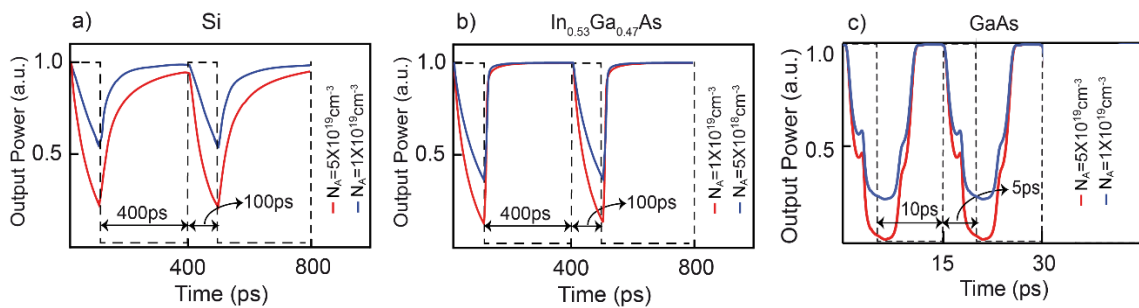


**Figure 3-6:** SPPD output signal (solid line) under step-type of input voltage (dashed black line) with magnitude (a) 1.3 V for Si and (b) 0.9 V for  $\text{In}_{0.53}\text{Ga}_{0.47}\text{As}$  and (c) 4 V for GaAs. The signal is repetitively switched following the external voltage. In the calculations, the operation frequency is set at 30 THz, and the donor doping concentration is  $N_D = 4 \times 10^{20} \text{ cm}^{-3}$  for the Si,  $N_D = 5 \times 10^{19} \text{ cm}^{-3}$  for the  $\text{In}_{0.53}\text{Ga}_{0.47}\text{As}$  and  $N_D = 5 \times 10^{19} \text{ cm}^{-3}$  for the GaAs device.

In the calculations, the maximum values of the input voltages are fixed above the corresponding critical values  $V_c = 1.14 \text{ V}$  for Si,  $V_c = 0.81 \text{ V}$  for  $\text{In}_{0.53}\text{Ga}_{0.47}\text{As}$  and  $V_c = 1.52 \text{ V}$  for GaAs. The SPPD transmittance curve, depicted in **Figure 3-6**, is obtained by finite difference (FD) self-consistent numerical calculations in the time domain and shows reproducible switching. Under a forward bias larger than the critical ( $V > V_c$ ), the minority carriers easily overcome the potential barrier due to the space-charge region. The electron concentration rises exponentially, and close to the metallurgic junction and within a few ps, the concentration surpasses the critical value  $n_c$  at which point, the SPPs are no longer able to propagate (establishing the “OFF” state of the device).

Once the applied bias is removed, the excess electrons in the  $P$ -layer diffuse and their concentration falls below the critical value. At this point, the SPPs can propagate through the device establishing the “ON” state. Consistently, faster response times are observed for GaAs. This can be attributed to the fact that GaAs SPPD is studied at very high voltages  $V = 4 V$ , whereas the Si  $V = 1.3 V$  and the  $\text{In}_{0.53}\text{Ga}_{0.47}\text{As}$  device  $V = 0.9 V$ . Moreover, the modulation rates are revealed to dependent on the acceptor doping concentration ( $N_A$ ), with higher doping's leading to faster signal modulation rates.

From **Figure 3-5(a-c)**, it is evident that to switch the SPPD it is not necessary for the minority concentration to surpass the critical value within the entire drift-diffusion zone; but only in close proximity to the metallurgic junction. This is a fundamentally different effect compared to convention all-electronic diodes where the response time is proportional to the electron fly time between the terminals. The SPPs, however, are exponentially sensitive to the dielectric environment in close proximity to the space-charge region (the metallurgic interface) and are switched OFF once the electron concentration within 20 to 50 nm from the junction surpasses the critical value  $n_c$ . This happens within a few picoseconds. This fact and the almost immediate signal transfer between a set of SPPDs (the SPPs travel with the speed of light) is what may allow for much faster response times and negligible interconnect delay times of lumped optoelectronic circuits made of SPPD as compared to conventional diodes.

#### 3.4.4 SPPD-Response Times and Operation Temperature

To assess the true potential of the SPPD as a fast-optoelectronic switch, we have performed extensive parametric analyses of the 3 dB ON ( $\tau_{3dB}^{ON}$ )/OFF ( $\tau_{3dB}^{OFF}$ ) times and maximum local temperature at the drift-diffusion region. The temporal response of the

device depends on the injection rate of electrons from the *N*-type into the *P*-type layer and thus on both applied voltage and doping concentrations.

The response times and temperature for different applied voltages and doping concentrations are shown in **Figure 3-7**. The ON time of the device is diffusion limited and is thus independent on the initial applied bias (the ON state is initiated after the voltage is switched off). The OFF times, however, are governed by the drift of the electrons in the *P*-type layer and are thus inversely proportional to the applied voltage. Furthermore, as shown in **Figure 3-7(b)**, the response times decrease exponentially with an increase in the *P*-layer doping. This phenomenon is due to the dependence of  $\tau_{\text{ON}}$  and  $\tau_{\text{OFF}}$  on the SPP penetration depth in the *P*-type layer which varies with the doping. The effects of applied voltage and doping on the response times can be quantitatively estimated as follows. In the presence of external bias, electrons drift into the *P*-layer with a velocity  $v_d \approx \mu_e^p (V - V_{bi}) / x_p$ , where  $\mu_e^p$  is the minority carrier drift mobility in *P*-type layer [101] [116, 117],  $x_p$  is the thickness of the *P*-layer and  $V_{bi}$  is the build-in potential [99].

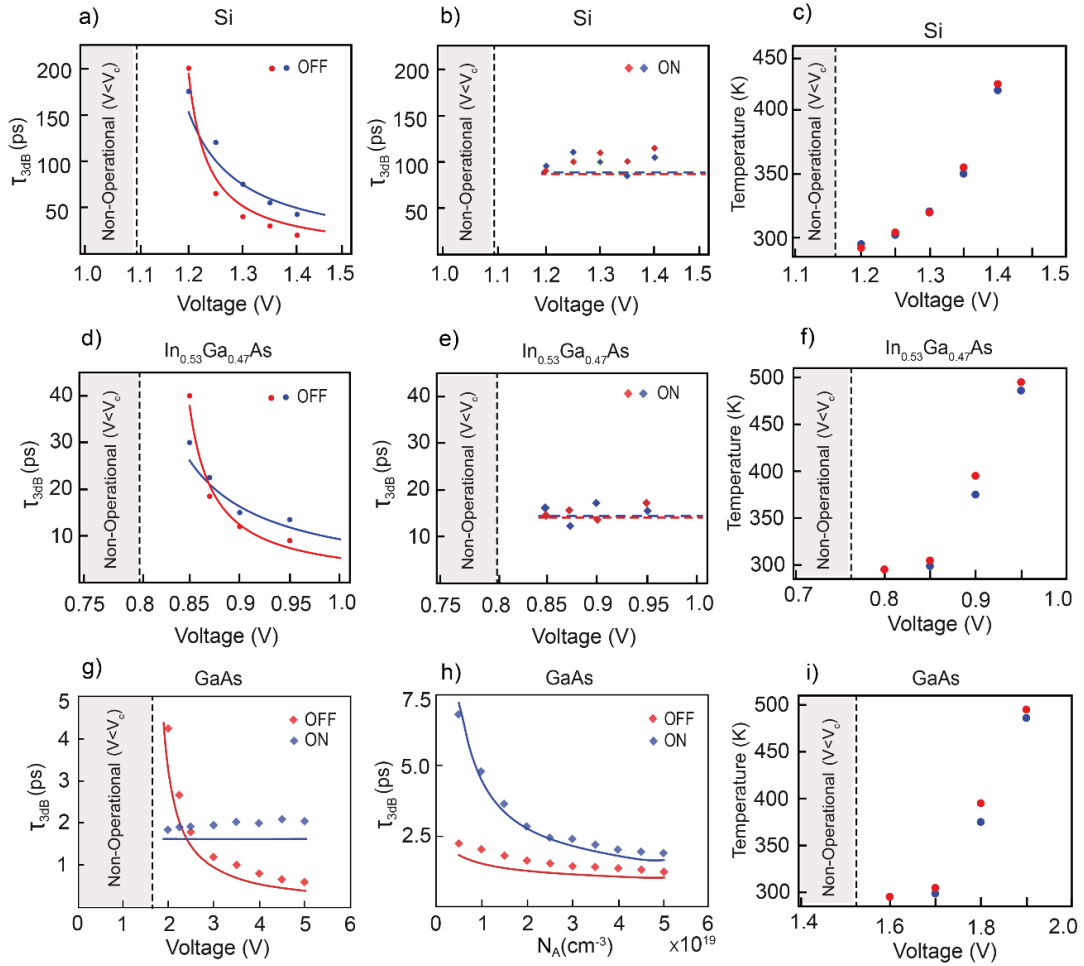


**Figure 3-7:** (a, d, g) Dependence of the SPPD OFF times on the applied voltage ( $V > V_c$ ). The device OFF time is dependent on the electron drift into the p-region and is thus inversely proportional to the applied voltage. (b, e, h) Dependence of the SPPD ON times on the applied voltage ( $V > V_c$ ). (h) The SPPD response times as a function of the P-layer doping concentration. (c, f, i) The maximum temperature recorded inside the device vs. the applied voltage. In the calculations, the operational frequency is set at 30 THz. The doping concentrations for the Si device are  $N_A = 1 \times 10^{19} \text{ cm}^{-3}$  (blue dots) and  $N_A = 1 \times 10^{20} \text{ cm}^{-3}$  (red dots) with  $N_D = 4 \times 10^{20} \text{ cm}^{-3}$ , for In<sub>0.53</sub>Ga<sub>0.47</sub>As the doping concentrations are  $N_A = 1 \times 10^{19} \text{ cm}^{-3}$  (red dots) and  $N_A = 1 \times 10^{18} \text{ cm}^{-3}$  (blue dots) with  $N_D = 5 \times 10^{19} \text{ cm}^{-3}$  for GaAs  $N_A = N_D = 5 \times 10^{19} \text{ cm}^{-3}$ . The doping influences both the width of the space charge region and the electron mobility and thus the ON and OFF times. In the figures, the numerical data (dots diamonds) is compared to the analytical drift-diffusion model (solid lines).

The SPPD OFF time is inversely proportional to the drift velocity and concurrently the applied bias and can be estimated as  $\tau_{\text{OFF}} = l_{\text{spp}}/v_d$ , where  $l_{\text{spp}} =$

$1/k_z^{spp} = 1/\sqrt{k_{spp}^2 - \epsilon_p k_0^2}$  is the field penetration depth of the SPP in the  $P$ -type layer.

At zero bias, the excess minority carriers in the  $P$ -layer are removed by net carrier outflow from the quasi-neutral region by the process of diffusion.

Using dimensional analyses, we can write the response (ON) time as  $\tau_{ON} = l_{spp}^2/(2D_n)$ ,  $D_n = (kT/q)\mu_e^n$  is the diffusion co-efficient of the electron in  $p$ -region, and  $\mu_e^n$  is the electron mobility [88] [118] [119]. The predicted above analytical considerations response times are shown with solid lines in **Figure 3-7**. Since the electron mobility of  $\text{In}_{0.53}\text{Ga}_{0.47}\text{As}$  is higher compared to Si and GaAs, we obtain faster response times for  $\text{In}_{0.53}\text{Ga}_{0.47}\text{As}$ . For sufficiently high applied voltages, the 3 dB data rates in excess of 50 Gbit/s can be obtained for  $\text{In}_{0.53}\text{Ga}_{0.47}\text{As}$  while moderate rates of up to 10 Gbit/s are expected for Si. However, the increase in the applied voltage can lead to an increase in heat dissipation. As clearly visible in **Figure 3-7(c, f, i)** where the maximum local temperatures within the device are depicted.

To minimize heating for the considered device sizes, the applied forward bias should not exceed 1.4 V in the case of Si, 1 V in the case of  $\text{In}_{0.53}\text{Ga}_{0.47}\text{As}$ , and 1.8 V in the case of GaAs. Further minimization of the power dissipation can be accomplished by reducing the size of the SPPD drift-diffusion region and varying the  $N$ -layer doping while keeping the SPP operation frequency within the experimentally accessible mid-IR spectral range. Here, the SPPD response times are estimated by fitting the transmittance data with an exponential function  $e^{-t/\tau}$ , where  $\tau$  is the rise/fall time. The 3 dB response times are then estimated using the standard procedure  $10 \log_{10} \left( e^{-\frac{\tau_{3dB}}{\tau}} \right) = -3$ .

### 3.5 SPPD Logic Gates

In **Figure 3-8**, we study possible optoelectronic logic elements based on the SPPD.

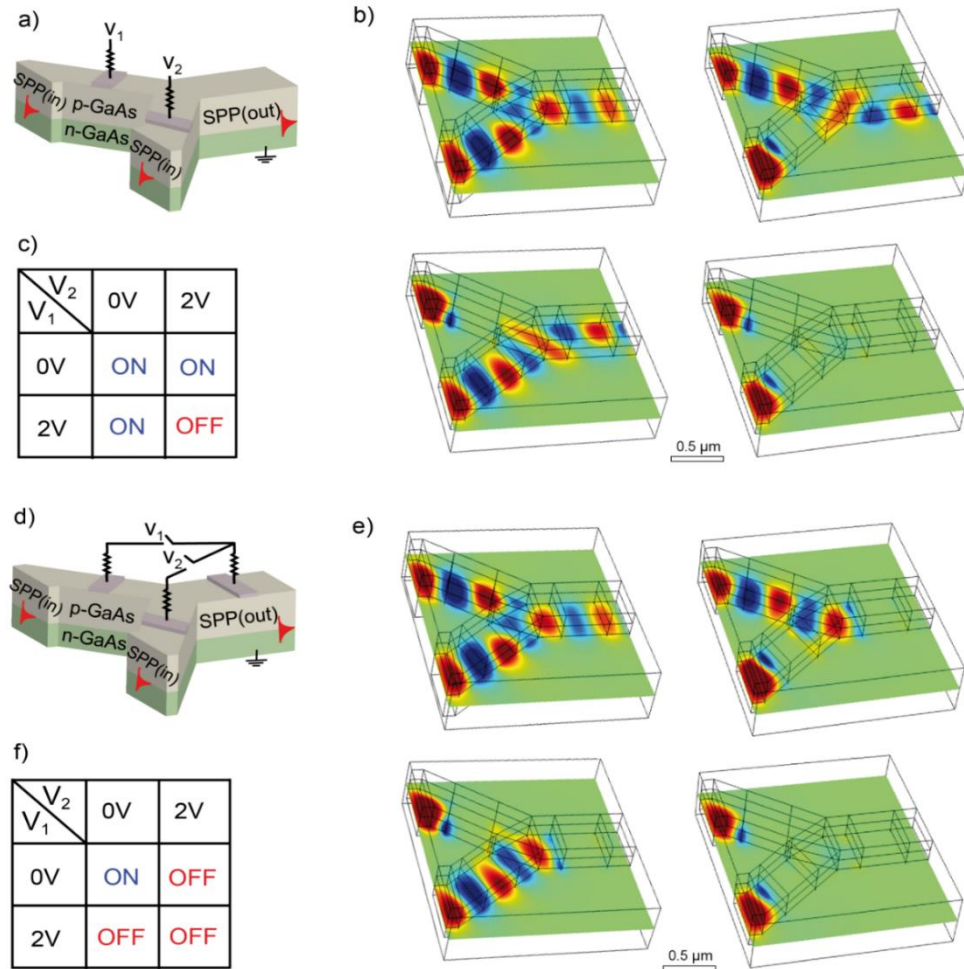


**Figure 3-8:** (a, d) Schematic of the SPPD logic (NAND and NOR) gates. (c, f) Logic table of the SPP NAND and NOR gates. (b, e) SPP propagation in the SPPD based NAND and NOR gates corresponding to the control voltages  $V_1$  and  $V_2$  as specified in the logic tables.

The logic elements are constructed by connecting three SPPs waveguides in a “Y” shape configuration, each waveguide controlled by separate SPPD. The NAND gate (**Figure 3-8(a)**) is controlled by two external voltages  $V_1$  and  $V_2$  applied at the input waveguides SPPDs, while the NOR gate (**Figure 3-8(b)**) is controlled by external

voltages applied in a series at the input and output waveguides SPPDs. In the absence of external bias ( $V_1 = 0V$  and  $V_2 = 0V$ ), the input SPPs interact constructively at the Y-junction, and the signal is transferred establishing “ON” states of both NAND and NOR gates. In the presence of single external bias ( $V_1 = 0V, V_2 = 2V$  or  $V_1 = 2V, V_2 = 0V$ ), the SPPs from one of the impute waveguides is transmitted in the case of the NAND gate (“ON” state) and reflected in the case of a NOR gate (“OFF” state).

When both input SPPDs are biased, there is no transmission, and both gates are in “OFF” state. The actual three-dimensional magnetic field profiles calculated in correspondence to the logic tables (see **Figure 3-8(c, f)**) are depicted in **Figure 3-8(b, e)**. Both electronic control (through the SPPD applied voltages) and constructive/destructive interference at the output waveguides are utilized to establish the proper input/output signal associations. We must emphasize that in principle there are many possible gate configurations, and the chosen “Y” shape design may not be the optimal. More importantly, due to the SPPD nature of the operation, the proposed logic gates are optoelectronic (not all-optic) and can be simply viewed as a fast and efficient way of controlling the propagation of surface plasmon polariton (SPP) modes at highly doped semiconductor interfaces.

### 3.6 SPPD-Temperature Sensor

The exponential dependence of the equilibrium minority concentration at the metallurgic junction with respect to the external voltage and local temperature can be used to develop a temperature sensor with high sensitivity. Specifically, from **Eq. 3-1** it follows the expected sensitivity of a temperature sensor based on the SPPD given as

$$\frac{dV_c}{dT} = \frac{k}{q} \ln \left[ \frac{\epsilon_b \omega^2}{\omega_{p0}^2} \right] \quad \text{Eq. 3-4}$$

For GaAs and operation frequency of 40 THz, the sensitivity of the device is expected to be a few mV/K. The power output for three different temperatures is shown in **Figure 3-9(a)**. These examples show the basic principle of the sensor operation. For an applied voltage of 0.5 V and temperature 300 K, there is no output signal. With the increase of the temperature, the diode is switched ON (red line). The modulation sensitivity with respect to the temperature is studied in **Figure 3-9(b)**. A slight change in temperature results in an exponential change in the output power with a sensitivity of more than 10 dB/K.

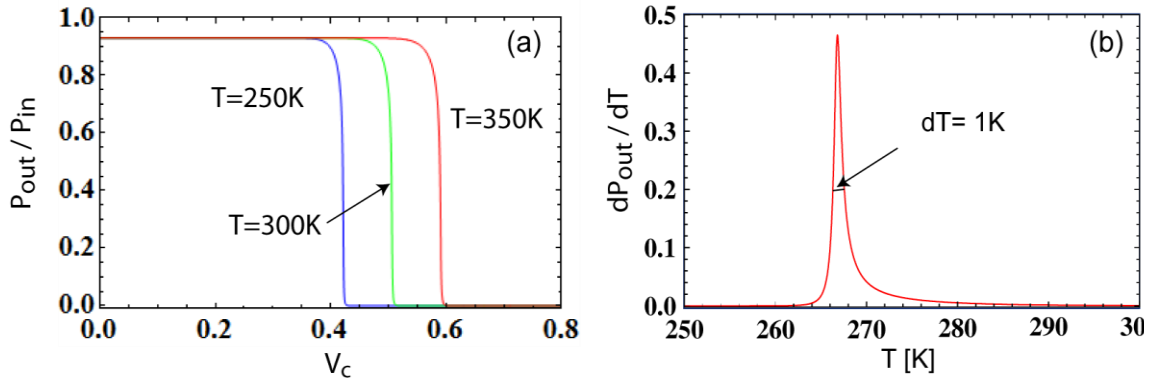


**Figure 3-9:** SPPD temperature sensor. Due to the abrupt (exponential) switching of the SPPD output signal, a temperature sensitivity of less than 1.7 mV/K is demonstrated.

### 3.7 SPPD-Experimental Implementation

Finally, for the experimental implementation and characterization of the SPPD, it is crucial to introduce an efficient coupling/decoupling scheme. In what follows, we consider local SPP excitation and detection using a pair of far-infrared single-mode

fibers and a set of gratings. The overall geometry of the proposed set up is shown in **Figure 3-10(a)**.

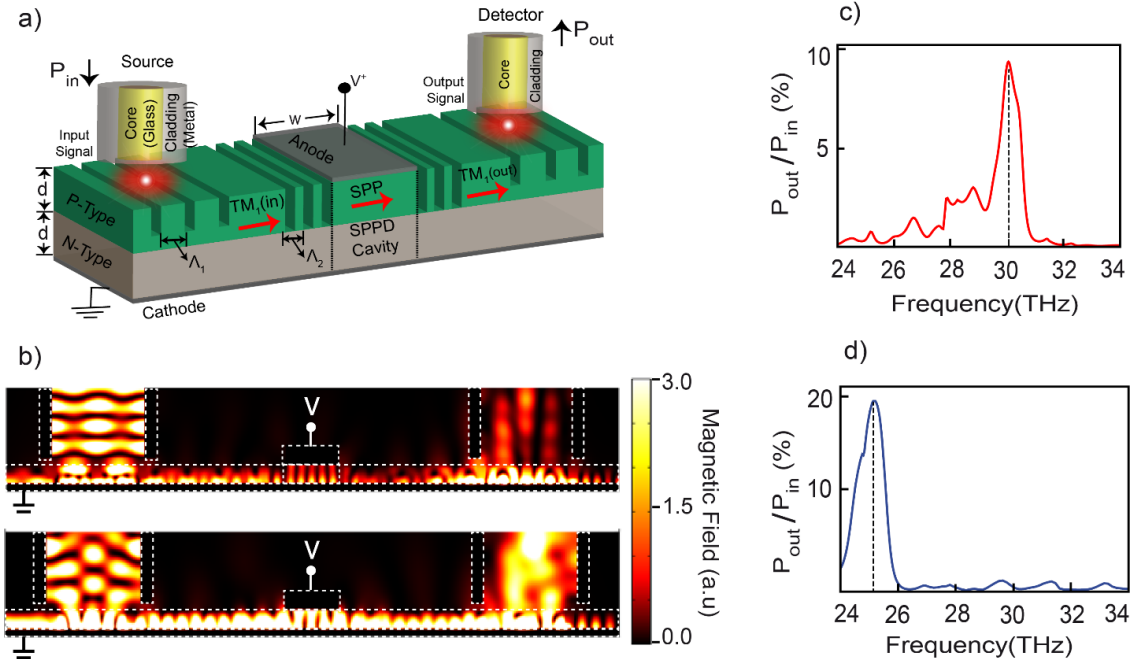


**Figure 3-10:** (a) Schematic of the SPPD with input and output waveguides coupling. (b) Magnetic field intensity for two different input grating  $\Lambda_1 = 6 \mu\text{m}$  (top) and  $\Lambda_1 = 5 \mu\text{m}$  (bottom) at constant SPP cavity grating  $\Lambda_2 = 2.6 \mu\text{m}$ . (c) SPP coupling efficiency for the  $\Lambda_1 = 6 \mu\text{m}$  (top) grating showing maximum efficiency at operating frequency of 30 THz. (d) SPP coupling efficiency for the  $\Lambda_1 = 5 \mu\text{m}$  (bottom) grating showing maximum efficiency at operating frequency of 25 THz.

The input radiation is coupled first to a low loss dielectric-dielectric-metal (DDM) waveguide mode of the  $P$ -layer, either  $TM_1$  for a planar device or  $TM_{11}$  for the rectangular device, which are then fed into a SPPD cavity via an etched grating. The cavity length is set at  $7 \mu\text{m}$  to support low order SPP resonances with a cavity height of  $1.8 \mu\text{m}$ . The SPPD output signal is then fed into the output fiber with a second grating. The local magnetic field profile for the planar device is shown in **Figure 3-10(b)**. The

excitation of the lower wavelength SPP cavity mode is clearly visible within the drift-diffusion region.

In the calculations, we have used two sets of input grating,  $\Lambda_1 = 6 \mu\text{m}$  (top) and  $\Lambda_1 = 5 \mu\text{m}$  (bottom), with a fixed output grating of  $\Lambda_2 = 2.6 \mu\text{m}$ . The grating periods have been optimized to obtain better coupling/decoupling efficiencies at two operational frequencies; 30 THz (top) and 25 THz (bottom). This is shown in **Figure 3-10(c, d)** where the output power efficiency is as high as  $\sim 9\%$  (for 30 THz) and up to  $\sim 20\%$  (for 25 THz). It must be noted that due to the used symmetric input grating, the decoupling efficiencies are fundamentally restricted to less than 50%. Alternatively, asymmetric grating configurations could also be considered to further improve the collected output signal. Regardless, the demonstrated efficiencies are sufficient for the practical demonstration of the device.

## CHAPTER 4

### EXPERIMENTAL REALIZATION OF SPPD

In this chapter, we present an important step towards the experimental realization of the SPPD studied in **Chapter 3**. Here, in collaboration with UT Austin, Mid-IR Photonics Laboratory, we demonstrate electrical control of the mid-IR optical properties of  $PN^+$ -junction fabricated by spin-doping of Si-on-oxide (SOI) wafers. We characterize the  $PN^+$ -junction device electrically and optically, measure the changes in the optical properties as a function of external bias voltage and the frequency. Finally, we present the comparison between the numerical results obtained using the thermo-electro-optical model and the corresponding experimental data. We found excellent agreement between the two, indicating the potential of the presented device architectures.

#### 4.1 Fabrication of Si $PN^+$ -Junction Device

The Si device is fabricated from an SOI wafer comprised of p-doped ( $N_A = 1 \times 10^{18} \text{ cm}^{-3}$ ) Si active region grown on  $1 \mu\text{m SiO}_2$  (see **Figure 4-1**). We initiate the fabrication process by diffusing  $N$ -type impurities to create a  $PN^+$ -junction. This is achieved by a spin on diffusion of phosphorous ( $N$ -type) impurity, where the SOI wafer is coated with 15% P compound-concentration dopant, prebaked ( $400^\circ\text{C}$ , 105 s) and then annealed ( $950^\circ\text{C}$ , 40 min) in an  $N_2$  environment. Next, the dopant film is removed with a

buffered oxide etch and followed by dicing of the doped SOI wafer, including the Si-wafer handle into square pieces.

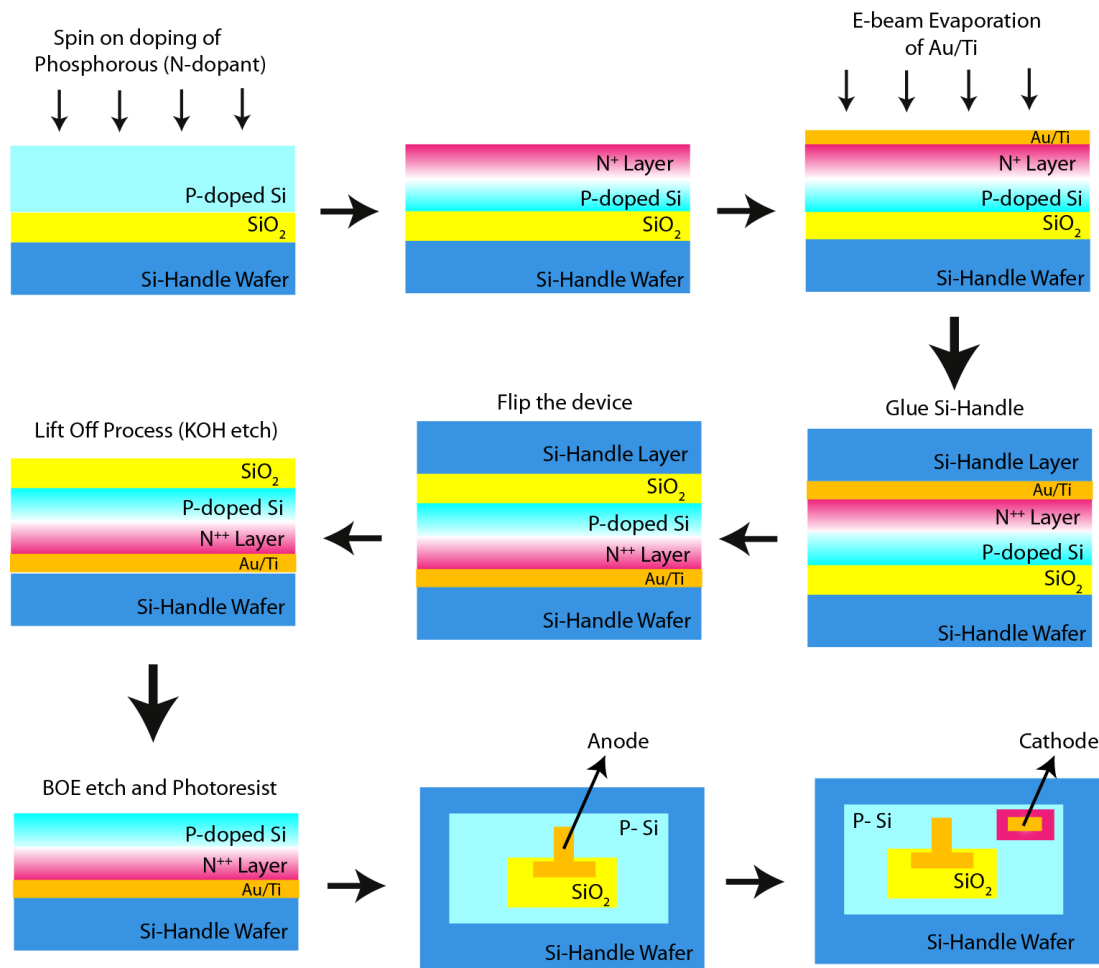


**Figure 4-1:** Fabrication process flow for the manufacturing of degenerate semiconductor (Si) PN<sup>+</sup> junctions.

The diced samples are now placed in an evaporation chamber, where Ti/Au is coated on both the SOI and Si handles. Metal-coated samples are bonded at 9 MPa pressure and 400°C for 20 min. The SOI wafer substrate is then removed using a deep silicon etcher, followed by a buffered oxide etch to remove the SiO<sub>2</sub> layer. Now the Si samples are then fabricated into mesa devices, with the mesas formed by standard UV

photolithography and dry etching in an Oxford ICP etcher. The SOI sample is etched by HBr/Cl<sub>2</sub>(45/5 sccm). Top and bottom contacts are then defined by photolithography, metallization (Ti/Au, 5/125 nm), and the lift-off process. Schematics of the steps for the fabrication process of Si-devices are shown in **Figure 4-1**. The samples are then mounted to copper mounting blocks and wire-bonded to stand-off ceramic pads. Schematics of the final device structures are shown in **Figure 4-2(a)**.

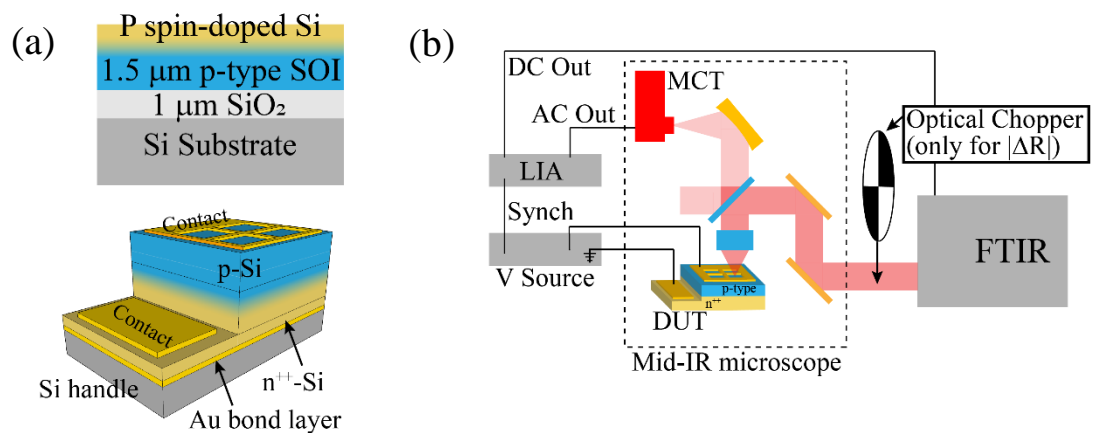


**Figure 4-2:** (a) Layer structure for the P spin-doped SOI wafer, and device schematic for the spin-doped N<sup>+</sup>P junction diode following wafer-bonding, substrate removal, and device fabrication. (b) Experimental set-up for amplitude modulation step-scan measurement of reflection ( $|R|$ ) modulation from the biased devices.

All samples were characterized by reflection spectroscopy using a Bruker v80V Fourier transform infrared (FTIR) spectrometer and a mid-IR microscope operating in rapid-scan mode and normalized to a reflection from an Au surface (which in the mid-IR has a near-perfect reflection). Upon fabrication, we measured the current-voltage (IV) characteristics of each device. Finally, we measured the change in reflection under applied bias using the experimental set-up shown in **Figure 4-2(b)**, where light incident upon the surface of a modulated N<sup>+</sup>P-junction diode (square wave voltage signal with an amplitude  $V_a$ ) and reflected to the microscope's HgCdTe (MCT) detector, whose output

is fed into a lock-in amplifier (LIA). The FTIR is then operated in a step-scan mode, and the DC output fed into the FTIR at each mirror position, giving the spectrum  $|I_R(\lambda, V_a) - I_R(\lambda, 0)|$ . To determine the absolute change in reflectivity (normalizing for the FTIR source spectrum, optics, and MCT response), an additional spectrum is taken, where the incident light is chopped before reflecting from the unbiased sample, giving  $I_R(\lambda, 0)$ . The modulation amplitude of reflection is then calculated using  $|R(\lambda)| = |I_R(\lambda, V_a) - I_R(\lambda, 0)|/I_R(\lambda, 0)$ . All measurements were performed at room temperature.

## 4.2 SPPD Characterization

Two types of characterizations of the Si SPPD devices have been performed. First, the fabricated devices were studied under zero external bias. These studies provided important material characteristics such as doping concentration profiles, layers thickness, plasma frequencies, and relaxation rates. Once the material of the device and geometrical characteristics were matched with the theory, we proceeded to characterize the SPPD modulation under external bias. Our results have clearly demonstrated the sensitivity of the SPPD optical response to external voltage bias validating the underlining theory behind the SPPD operation.

### 4.2.1 Model for Optical Parameter Extraction

Here, we consider diffusion of donors in *P*-type semiconductors with donor profile given as

$$N_D(x) = N_D \operatorname{erfc}\left(\frac{x}{x_D}\right), \quad N_A(x) = N_A, \quad x \geq 0 \quad \text{Eq. 4-1}$$

where  $x_D$  is the doping length. In steady-state, the electron and hole current densities are zero and the normalized potential  $\varphi(x) = qV(x)/kT$  is a solution of the Poisson-Boltzmann equation

$$\varphi''(\zeta) = \lambda^2 \left( \frac{2n_i}{N_D} \sinh(\varphi(\zeta)) + \frac{N_A}{N_D} - \operatorname{erfc}(\zeta) \right) \quad \text{Eq. 4-2}$$

where  $\zeta = x/x_D$ ,  $\lambda = x_D/\lambda_D$  and  $\lambda_D = \sqrt{\epsilon\epsilon_0 kT/q^2 N_D}$  is the Debye length. **Eq. 4-2** in non-linear, inhomogeneous second order ODE and do not have an analytical solution.

However, for high doping, the Debye length is much smaller compared to the doping length scale ( $\lambda = x_D/\lambda_D \gg 1$ ), and we can neglect the second order derivative in **Eq. 4-2** giving the local charge neutrality  $N_D - n - N_A + p = 0$ . The potential is then easily obtained as

$$\varphi(\zeta) = \sinh^{-1} \left( \frac{N_D \operatorname{erfc}(\zeta) - N_A}{2n_i} \right) \quad \text{Eq. 4-3}$$

The junction is formed at  $\varphi(\zeta_j) = 0$  and, hence, we have  $x_j = x_D \operatorname{erfc}^{-1}(N_A/N_D)$ .

Similarly, using **Eq. 4-3** we obtain the build-in potential

$$V_{bi} = \frac{kT}{q} (\varphi(0) - \varphi(\infty)) = \frac{kT}{q} \left( \sinh^{-1} \left( \frac{N_A}{2n_i} \right) + \sinh^{-1} \left( \frac{N_D - N_A}{2n_i} \right) \right) \quad \text{Eq. 4-4}$$

If  $N_D \gg N_A \gg 2n_i$  we get  $V_{bi} \approx V_T \ln(N_A N_D / n_i^2)$ , which is the classical value for homogeneous doping and abrupt junction. The electron/hole concentrations are obtained from the local charge neutrality condition and enforcing the mass action law giving

$$n(\zeta) = \frac{1}{2} \left( \sqrt{(N_D(\zeta) - N_A)^2 + 4n_i^2} + N_D(\zeta) - N_A \right) \quad \text{Eq. 4-5}$$

$$p(\zeta) = n_i^2 / n(\zeta)$$

The accuracy of the approximate results **Eq. 4-3** and concurrently **Eq. 4-5** was checked by numerically integrating the Poisson-Boltzmann equation (**Eq. 4-2**). Our results for three sets of parameters are shown in **Figure 4-3**. Since for the degenerate doping levels used in the SPPD we have  $\lambda > 1000$ , it is clear that **Eq. 4-3** coincides with the exact

numerical solution and hence will be used in the optical parameters extraction procedure described next.

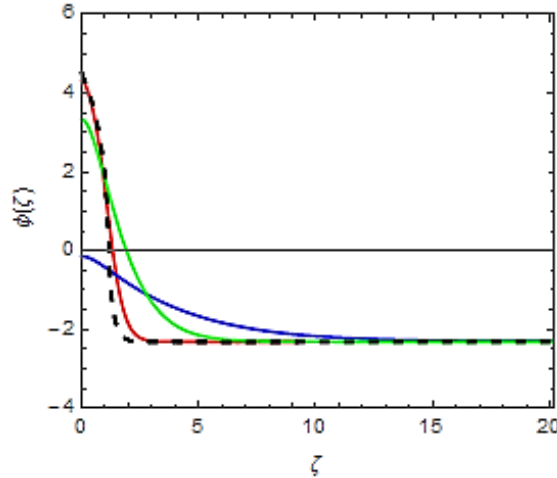


**Figure 4-3:** The built-in electrical potential obtained by numerically solving **Eq. 4-2** (solid lines) is compared to the charge neutrality result **Eq. 4-3** (dashed line). The doping parameters used are  $\lambda = 1$  (blue),  $\lambda = 3$  (green), and  $\lambda = 10$  (red). In all calculations, we have set  $n_i/N_D = 0.01$  and  $N_A/N_D = 0.1$ .

To extract the doping profile from the experimental data, we use the transfer matrix approach (TMA). For inhomogeneous permittivity profile  $\varepsilon(x)$ , we represent the doped semiconductor material as a system of  $N$  homogeneous layers each with constant permittivity

$$\varepsilon_j(\omega) = \varepsilon_b(\omega) - \frac{\omega_{pj}^2}{\omega(\omega - i\omega_{\tau j})} \quad \text{Eq. 4-6}$$

$$\omega_{pj}^2 = \frac{\tilde{\omega}_{pj}^2}{2} \left( \sqrt{\left( \operatorname{erfc}\left(\frac{x_{j-1} + w_j/2}{x_D}\right) - \frac{N_A}{N_D}\right)^2 + \left(\frac{2n_i}{N_D}\right)^2} + \operatorname{erfc}\left(\frac{x_{j-1} + w_j/2}{x_D}\right) - \frac{N_A}{N_D} \right) \quad \text{Eq. 4-7}$$

where  $w_j = x_j - x_{j-1}$  are the  $j$ -layer thicknesses,  $\tilde{\omega}_{pj} = \sqrt{q^2 N_D / \epsilon_0 m_{ej}}$  is the plasma frequency at the front of the device, and the doping and position dependent relaxation rates, mobilities and effective electron mass are given as

$$\omega_{\tau j} = \frac{q}{\mu_{nj} m_0 m_{ej}} \quad \text{Eq. 4-8}$$

$$\mu_{nj} = \mu_{n,min} + \frac{\mu_{n,max} - \mu_{n,min}}{1 + \left[ \frac{N_A}{N_r} + \frac{N_D}{N_r} \operatorname{erfc} \left( \frac{x_{j-1} + w_j/2}{x_D} \right) \right]^{0.85}} \quad \text{Eq. 4-9}$$

$$m_{ej} = 0.28 + 0.42 \times \left[ \frac{N_D}{N_m} \operatorname{erfc} \left( \frac{x_{j-1} + w_j/2}{x_D} \right) \right]^{0.65} \quad \text{Eq. 4-10}$$

For phosphorous doped Silicon, we have  $N_r = 1 \times 10^{23} \text{ m}^{-3}$ ,  $\mu_{n,min} = 0.0092 \text{ m}^2/\text{V.s}$ ,  $\mu_{n,max} = 0.141 \text{ m}^2/\text{V.s}$  and  $N_m = 10^{24} \text{ m}^{-3}$ . At high doping, the effective mass and mobility are doping dependent and shown in **Figure 4-4**.

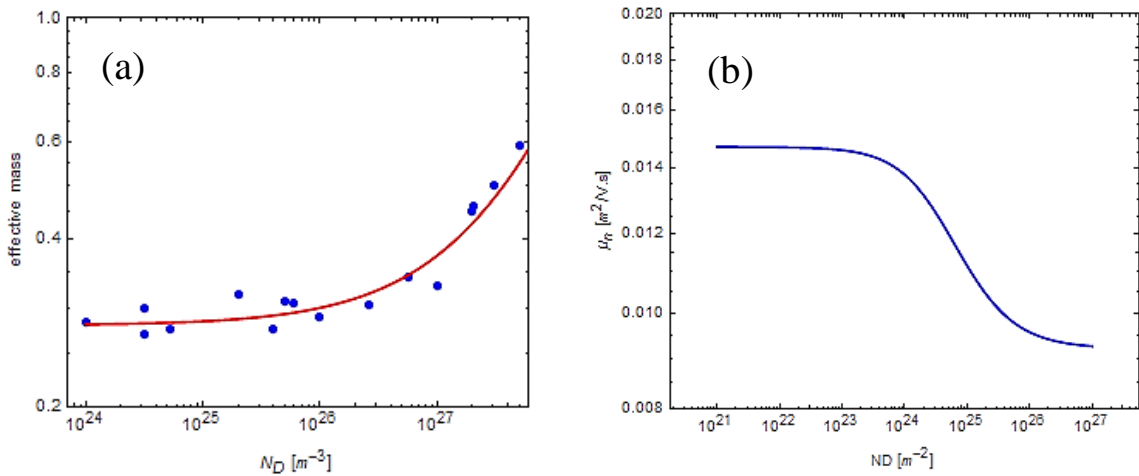


**Figure 4-4:** Dependence of (a) effective mass and (b) mobility on doping.

For normal incidence, the transfer matrix method connects the field amplitudes and their derivatives in the adjacent layers as follows

$$\begin{pmatrix} \psi_j(x_j) \\ \psi'_j(x_j) \end{pmatrix} = \widehat{M}_j \begin{pmatrix} \psi_{j-1}(x_{j-1}) \\ \psi'_{j-1}(x_{j-1}) \end{pmatrix}, \quad \widehat{M}_j = \begin{pmatrix} \cos(k_j w_j) & \frac{1}{k_j} \sin(k_j w_j) \\ -k_j \sin(k_j w_j) & \cos(k_j w_j) \end{pmatrix} \quad \text{Eq. 4-11}$$

The reflection and transmission coefficients are obtained by matching the field components at the front and back of the stratified media and the reflectance then follows

$$R = |r|^2 = \left| \frac{k_b M_{11} - k_a M_{22} + i(M_{21} + k_a k_b M_{12})}{k_b M_{11} + k_a M_{22} + i(M_{21} - k_a k_b M_{12})} \right|^2 \quad \text{Eq. 4-12}$$

where  $M_{ij}$  are the components of the transfer matrix  $\hat{M} = \hat{M}_N \hat{M}_{N-1} \cdots \hat{M}_2 \hat{M}_1$ .

#### 4.2.2 Reflectivity Measurements and Optical Parameter Extraction

The reflectance of the in-homogeneously doped semiconductors depends on three independent parameters: maximum (surface) doping concentration  $N_D$ , doping penetration depth  $x_D$ , and the permittivity of the original  $P$ -doped semiconductor  $\epsilon_b$ . The extraction procedure is a five (5) step process which follows the fabrication steps of the SPPD device.

**Step 1: P-doped wafer:** Obtain the wavelength dependent permittivity  $\epsilon_b(\lambda)$  of the  $P$ -doped semiconductor from reflectivity measurements. In the far-infrared spectral range, the semiconductor permittivity is predominantly real and can be directly obtained from the Fresnel equations. For normal incidence,  $R(\lambda) = (1 - n_b(\lambda))/(1 + n_b(\lambda))$ , which can be re-written to estimate the permittivity as  $\epsilon_b(\lambda) = \left(1 + \sqrt{R(\lambda)}\right)^2 / \left(1 - \sqrt{R(\lambda)}\right)^2$ .

**Figure 4-5** depicts the extracted  $p$ -doped layer permittivity of Si.

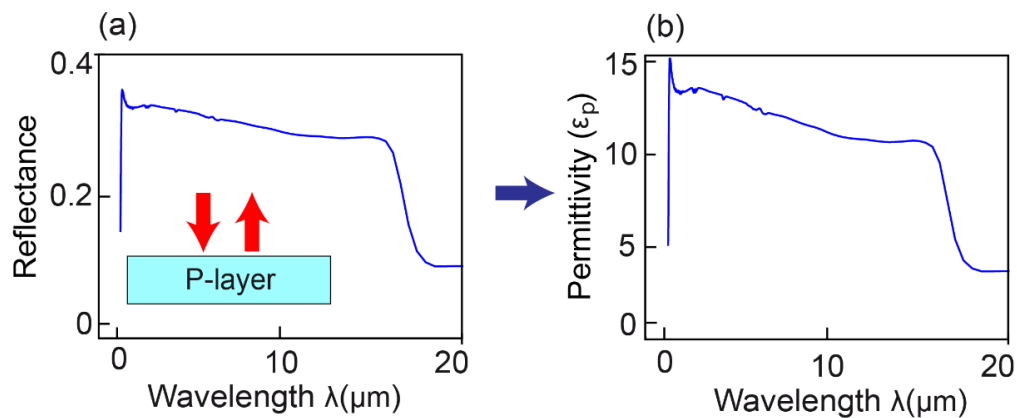


**Figure 4-5:** (a) Reflectance and (b) Effective permittivity of the  $p$ -doped wafer.

**Step 2: Un-doped multilayer device:** We use the transfer matrix method (TMM) to find a set of parameters (layers thicknesses) that minimize the error between the experimentally obtained reflectance of the un-doped multi-layer device predicted by the model. Figure 5.6 depicts the schematic of the initial SOI wafer under consideration, the thickness of the corresponding SiO<sub>2</sub> and Si Substrate are of  $\sim 1 \mu m$  and  $\sim 500 \mu m$ . Applying the TMM, the first layer (p-doped) permittivity ( $\epsilon_p(\lambda)$ ) is obtained from the standalone *P*-layer reflectance data (see Step 1). For the middle (SiO<sub>2</sub>) layer, we considered tabulated frequency dependent permittivity/refractive index. The bottom Si handle has a constant permittivity  $\epsilon_{si} = 11.7$ . **Figure 4-6(b)** shows a comparison between the theoretical and experimental reflectance data. A best match is obtained for *P*-layer thickness;  $d = 2.05 \mu m$  and  $\epsilon_p'' = 0.2$ .

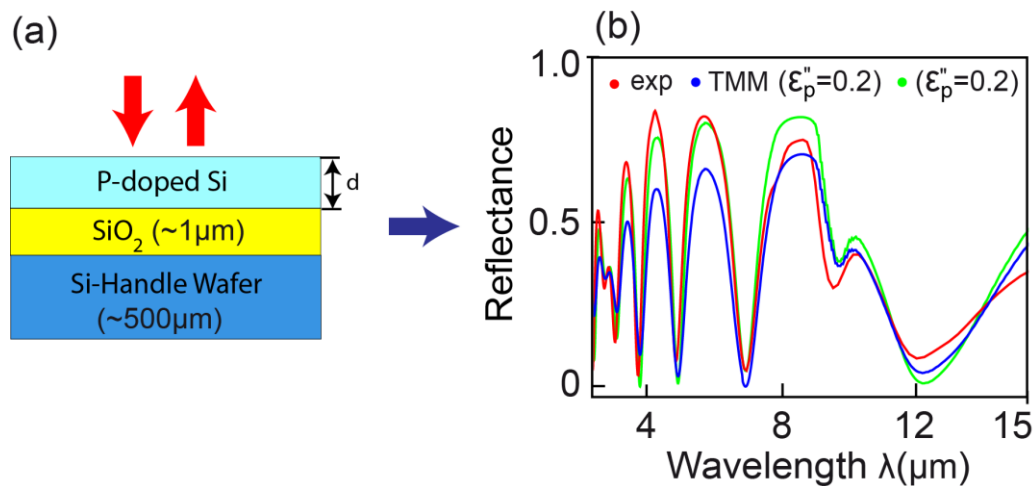


**Figure 4-6:** (a) Schematic of the un-doped multilayer device. (b) Comparison of the experiment (red solid line) and TMM model (blue and green solid line).

**Step 3: Doped multilayer device:** **Figure 4-7(a)** depicts the device geometry after the spin on doping of *n*-type impurity on the SOI wafer. Transition layer with graded

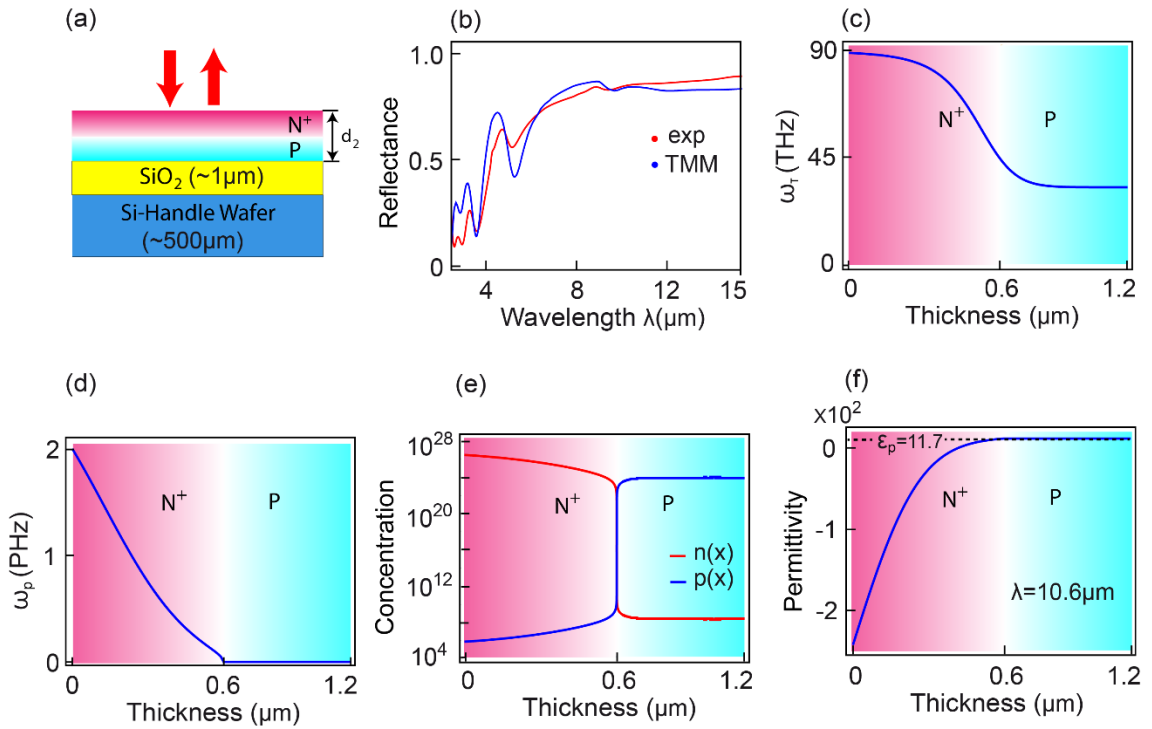


**Figure 4-7:** (a) Schematic of the SOI wafer after spin on diffusion of  $n$ -type impurities, (b) Comparison of reflectance due to experiment (red solid line) and TMM model (blue solid line), (c) plasma frequency, (d) relaxation frequency, (e) electron concentration and (d) permittivity.

doping concentration is formed from the top surface leading to the formation of a PN-junction. As a result, position-dependent permittivity is formed

$$\epsilon_s(\omega, x) = \epsilon_p(\omega) + i\epsilon_p'' - \frac{\omega_p^2(x)}{\omega(\omega + i\omega_\tau(x))} \quad \text{Eq. 4-13}$$

where  $\omega_p(x)$  and  $\omega_\tau(x)$  are the position dependent plasma and relaxation frequencies, respectively. To determine these complex dependences, we again rely on the TMM model. The extraction procedure includes optimizing fitting parameters such as doping length ( $x_D$ ), the thickness of the  $PN$ -region ( $d_1$ ) and maximum donor concentration ( $N_D$ ). The theoretical and experimental reflectance (see **Figure 4-7(b)**) are matched for  $x_D = 0.29 \mu\text{m}$ ,  $N_D = 2.85 \times 10^{26} \text{ m}^{-3}$  and thickness  $d_1 = 1.10 \mu\text{m}$ . From the extracted parameters, we can also estimate the  $pn$ -junction distance from the top of the sample

$x_j = 0.598 \mu\text{m}$ . **Figure 4-7(c-f)** shows the variation in the  $n(x)$ ,  $\omega_p(x)$ ,  $\omega_\tau(x)$  and  $\varepsilon_p(x)$ . Close inspection of **Figure 4-7(f)** shows the transition in the permittivity from negative to positive at the  $PN$ -junction interface which satisfies the condition for the existence of the SPP.

**Step 4: Doped multilayer device with bottom electrode:** The schematic of the final SPPD device after deep etching and gold electrode deposition is shown in **Figure 4-8(a)**. To model the  $PN^+$ -layer, we use the  $\omega_p(x)$  and  $\omega_\tau(x)$  profiles obtained in Step 3. The 250 nm gold layer is modelled using the Drude;  $\varepsilon_g(\omega) = 9.5 - f_p^2/f(f + if_\tau)$ , where  $f_p = 2.183 \text{ PHz}$  and  $f_\tau = 17.14 \text{ THz}$ . The theoretical and experimental reflectance shown in **Figure 5.8(b)** are in good agreement when the optical parameters extracted in Step 3 are used;  $x_D = 0.29 \mu\text{m}$ ,  $N_D = 2.85 \times 10^{26} \text{ m}^{-3}$  and  $\varepsilon_p'' = 0.78$  (see **Figure 4-6(b)**).

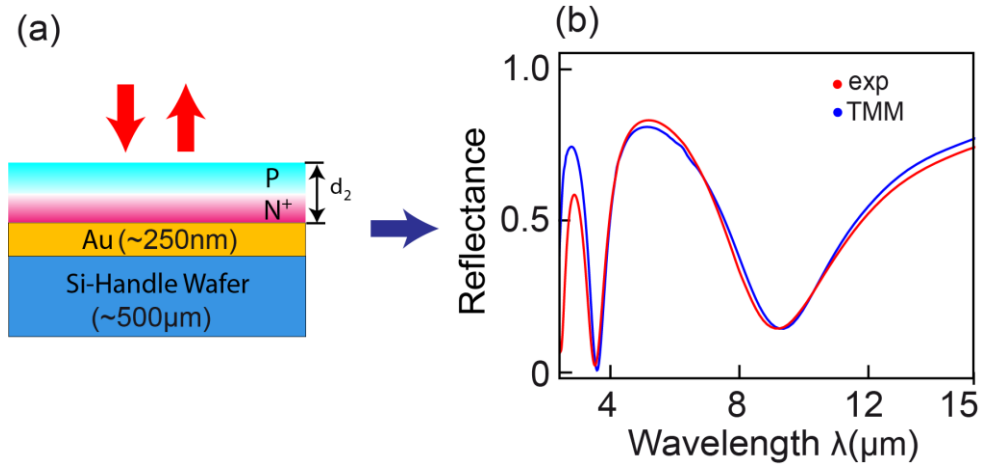


**Figure 4-8:** (a) Schematic of the Si PN-diode with the bottom gold anode. (b) Comparison of the experiment (red solid line) and TMM model (blue and green solid line).

The best fit is obtained for diode thickness  $d_2 = 0.81 \mu\text{m}$ . The  $PN$ -layer thickness obtained here is in slight deviation from the one obtained in Step 3 ( $d_1 - d_2 = 0.19 \mu\text{m}$ ),

which is a result of the deep etching process. Also, there is a slight discrepancy in the amplitude at short wavelengths. This may be the result of added impurities and oxidation during gold deposition and etching.

**Step 5: Doped multilayer device with the bottom and top electrodes:** The last step in the SPPD fabrication is the deposition of the top electrode. The experimental patterning of the top electrode and the schematic of the numerically simulated device are shown in **Figure 4-9(a)**. The theoretically and experimentally obtained reflectance are depicted in **Figure 4-9(b)**. These results complete our investigation into the SPPD material and geometrical characteristics.

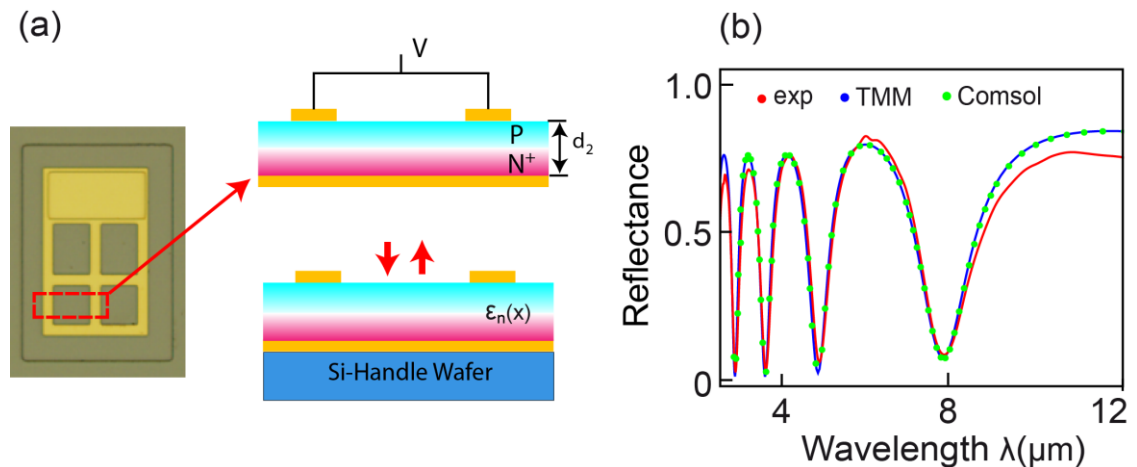


**Figure 4-9:** (a) Schematic of the Si PN-diode with top and bottom electrodes. (b) Comparison of the experiment (red solid line) and TMM model (blue) and direct full-wave simulation using the COMSOL software (green dots).

#### 4.2.3 Reflectivity Modulation and IV Characteristics

**Figure 4-10** shows the relative change in reflectance  $|\Delta R(\lambda)| = |R(\lambda, V_a) - R(\lambda, 0)|/R(\lambda, 0)$  for forward biases. Both experiment and theory show distinct spectral features associated with the charge injection/depletion of the biased junction, with changes in reflectance occurring predominantly at the edges of strong reflection features.

These changes are more pronounced in forward bias but are also observed in reverse bias. The correspondence between theory and experiment is excellent up to a forward bias of  $V_a = 0.68 \text{ V}$ . For higher voltage, a discrepancy between theory and experiment is observed, with the theory predicting stronger modulation of reflectance. This discrepancy can be explained by the effect of a contact resistance present in the experimental device.

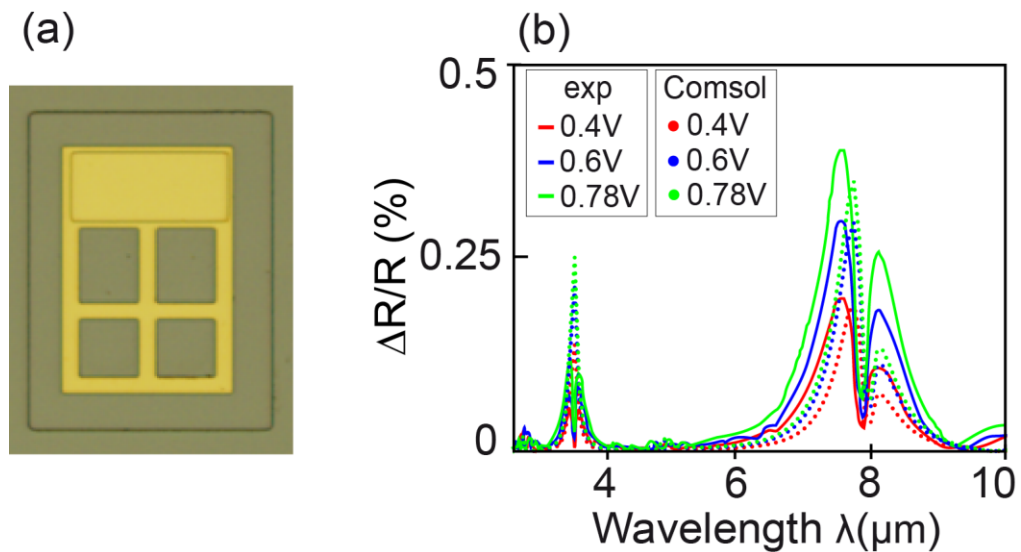


**Figure 4-10:** (a) Schematic of the Si PN-diode with top and bottom electrodes. (b) Comparison of the experiment (red solid line) and TMM model (blue) and direct full-wave simulation using the COMSOL software (green dots).

#### 4.2.4 Extraction of Contact resistance

To better understand the discrepancy in the reflectance at high applied voltage, we studied the IV response of the device. The experimental and theoretical response is shown in **Figure 4-11**.

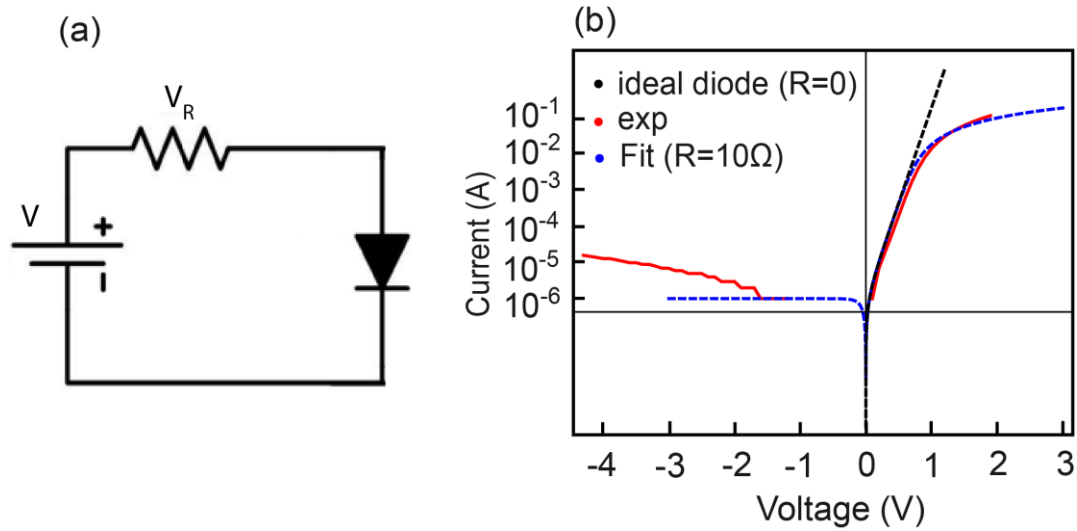


**Figure 4-11:** (a) Equivalent circuit for the PN-diode in series with the contact resistance. (b) IV-curve comparison of the experiment (red solid line), analytical model (dashed blue) and ideal diode IV (dashed black).

To model the experimental data, we consider an “ideal” diode rectified by a series contact resistance  $R$ . The current vs voltage relationship in this case is given as

$$I = I_s \left( e^{\frac{V-IR}{nV_T}} - 1 \right) \quad \text{Eq. 5-14}$$

where  $I_s$  is the saturation current at reverse bias,  $V_T = kT/q$  is the thermal voltage and  $n = 2$  is the high current exponent. **Eq. 4-14** can be solved explicitly in terms of the current giving

$$I = I_s \left[ \frac{nV_T}{RI_s} W \left( \frac{RI_s}{nV_T} e^{\frac{V+RI_s}{nV_T}} \right) - 1 \right] \quad \text{Eq. 4-15}$$

where  $W$  is the Lambert W-function. A best fit is obtained for a contact resistance of  $R = 10 \Omega$ . This is rather a large value which shows that there is a room for substantial improvement in the experiment. Additionally, at large voltages, the effective temperature of the junction is expected to increase with the current (see **Figure 3-5(g-i)**).

## CHAPTER 5

### ALL-OPTICAL SWITCHING OF SPPS USING EXTRAORDINARILY HIGH THERMO-OPTICAL NONLINEARITY

In the preceding chapters, we have shown the possibilities of using semiconductor materials in the subwavelength regime in designing plasmonic optoelectronic switching device where the switching of SPPs is obtained by applying an external voltage. In this chapter, we will focus our efforts to extend our initial work and design an all-optical analog of SPPD; where the switching of SPPs is by using a control SPP mode. The switching mechanism is through a new thermo-optical nonlinearity present at the highly-doped *PN*-junction with the goal of obtaining the all-optical plasmonic device, with high signal modulation paving the path to a viable cutting-edge optical computing.

#### 5.1 Introduction to Thermo-optical Nonlinear Switch

Here, we perform a thorough investigation of thermal characteristics of the SPPD and will demonstrate a new type of all-optical device, which we refer to as Surface Plasmon Polariton Diode (thermal) or SPPDt, can operate at all-optical switching rates surpassing 10GHz. The general schematic of the SPPDt is shown in **Figure 5-1**. A cross-type structure of a highly doped *P*-layer is formed on top of a highly doped *N*-layer. One of the constraints of SPPDt is the chosen semiconductor material must have excellent thermal properties, specifically large thermal diffusivity. In the operation of the SPPDt,

two types of SPP modes are involved, a signal and a control. If the control beam is switched off the signal passes through the drift-diffusion region uninterrupted. The application of the control beam results in added heating in the shared part of the waveguide (the drift-diffusion zone, below the top electrode) which induces a strong thermo-optical effect in the vicinity of the PN-junction and switches OFF the signal.

We mainly focus on discussing the following: **a)** design and operational characteristics of SPPDt. **b)** to access the SPPDt switching characteristics for different doping of *P*-layer, operational frequency and as well as the width of the active drift-diffusion region. **c)** to design all four possible SPPDt logic gates (AND, NAND, OR and NOR).

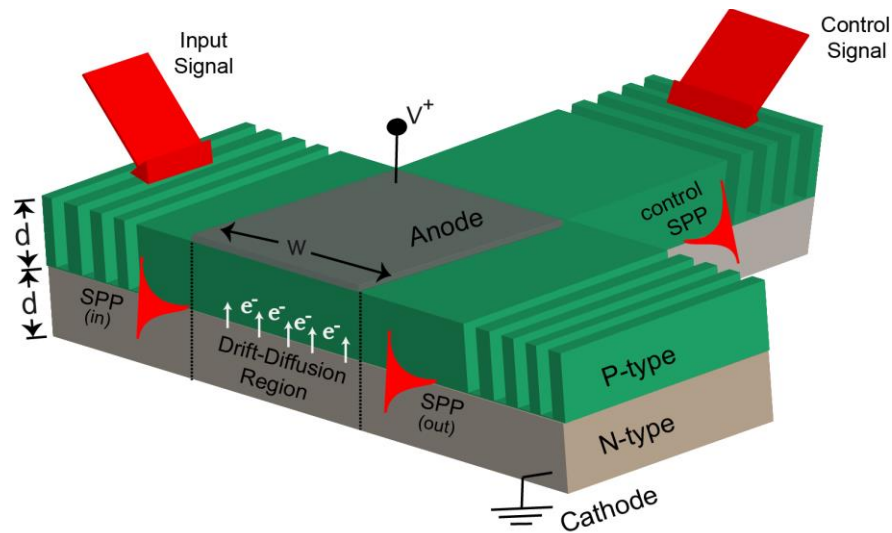


**Figure 5-1:** Schematic of the SPPDt.

## 5.2 Working Principle of SPPDt

Structure and design of an SPPDt is shown in **Figure 5-1**. Silicon is chosen for the initial device's demonstration and future analysis will be done for other

semiconducting materials for understanding the best performer. The temperature dependence of the effective permittivity of the  $P$ -type layer is given by the Drude model,  $\epsilon_p(T) = \epsilon_b - \omega_p^2(T)/\omega(\omega + i\omega_\tau(T))$ , where the plasma frequency of the  $P$ -layer  $\omega_p^2(T) = e^2 n_i^2(T) e^{eV/k_B T} / (\epsilon_0 N_A m_e)$  and relaxation frequency  $\omega_\tau(T) = e/m_e \mu_e^p(T)$  are strongly dependent on the temperature through the intrinsic electron concentration  $n_i$ , electron mobility in the  $P$ -layer  $\mu_e^p$  and applied voltage.

The working concept of the SPPDt can be explained using the temperature dependence of the intrinsic concentration. The  $T^{3/2}$  is the dependence of the intrinsic carrier concentration  $n_i^2 = BT^3 e^{-E_g(T)/kT}$ , where  $B = 4(2\pi k/h^2)^3 (m_{eff}^h m_{eff}^e)^{3/2}$  and  $E_g(T) = E_g - \alpha T^2/(T + \beta)$ , where  $E_g = 1.12 \text{ eV}$ ,  $\alpha = 4.73 \times 10^{-4} \text{ eV/K}$ ,  $\beta = 636 \text{ K}$  for Si [99] and the exponential dependence of the equilibrium minority concentration  $n = n_0 e^{V_c/V_T}$  (where  $n_0 = n_i^2/N_A$  and  $N_A$  is the acceptor concentration) at the metallurgic junction with respect to the applied voltage and temperature can be used to develop a high sensitive thermal switching of SPP's. At the ambient temperature, the depletion region at the  $PN$ -junction prevents the free carriers to cross from the  $N$ -type into the  $P$ -type layer. As a result for frequencies  $\omega_p^h < \omega < \omega_p^n$ , the  $n$ -layer acquires metal-like properties ( $\epsilon_s^n < 0$ ) while the  $P$ -layer acts as a dielectric ( $\epsilon_s^p > 0$ ), where  $\omega_p^h$  is the plasma frequency of the  $P$ -layer and  $\omega_p^n$  is the plasma frequency of the  $N$ -layer. This allows SPPs to propagate along the interface establishing the "ON" state of the device.

Next, a temperature change is induced at the  $PN$ -junction, through a high intensity control beam of the excited electro-magnetic modes. This increase in the lattice temperature consequences in the injection of electrons within the active drift zone (see **Figure 5-1**) resulting in dramatic modification of  $P$ -layer permittivity ( $\epsilon_s^p < 0$ ). This

modification results in strong reflection of the SPPs at the active zone, establishing the “OFF” state of the device.

The above phenomenon can be qualitatively described using the Wentzel-Kramers-Brillouin (WKB) method as described for the SPPD

$$TT(V, T) = \left| \exp \left( i \int_0^w k_{SPP}(x, V, T) dx \right) \right|^2 \approx e^{-2w \text{Im}[k_{SPP}(V, T)]} \quad \text{Eq. 5-1}$$

where  $w$  is the thickness of the active drift region,  $T$  is the lattice temperature, and the SPP wave vector  $k_{SPP}$  is the position, voltage and temperature dependent due to the spatially inhomogeneous minority carrier concentration in the  $P$ -type layer. For a given frequency of operation  $\omega$  and sufficiently low minority carrier concentration we have  $k_{SPP} \in \mathbb{R}$  and  $TT \approx 1$ . For  $T > T_c$ , the SPP wave vector becomes complex quantity ( $k_{SPP} \in \mathbb{C}$ ) and the transmittance exponentially decreases with the thickness  $w$ . We can obtain the operational range of the device by forcing the transparency condition  $\text{Re}[\varepsilon_p(\omega, V, T_c)] = 0$ , which now is solved with respect to the critical temperature  $T_c$ , beyond which the  $P$ -layer acquire metal-like properties. This critical temperature can be obtained explicitly and is given as

$$T_c = \alpha T_a W^{-1} \left( \frac{\alpha e^\alpha \omega_p^{2/3}(T_a)}{\omega^{2/3} \varepsilon_b^{1/3}} \right) \quad \text{Eq. 5-2}$$

where  $\alpha = (E_g - eV)/3k_B T_a$ ,  $E_g$  is the band gap energy at the ambient temperature  $T_a$ , and  $W$  is the Lambert W function.

### 5.3 SPPDt-Steady State Analysis

As described, the SPPDt switching is mainly due to the injection of minority carriers in the presence of a constant forward bias voltage and the high-intensity control-

SPP. Here, the junction temperature is predominantly influenced by the electromagnetic energy dissipation of the control-SPP. Additionally, the flow of charge carriers will also result in Ohmic heating. The above two processes will result in an increase of metallurgical junction temperature. To have a proper understanding of the complex Multiphysics processes governing the SPPDt operation, we again use the developed self-consistent thermo-electro-optic (see **Section 3.2**).

Using the thermo-electro-optic model, we begin our study of the SPPDt input-output characteristics by first considering the steady-state case. As identified above, a rapid decrease in SPP power transmission is expected for a forward bias just less than  $V < V_c$  and the local temperature larger than the critical  $T > T_c$ , for which the  $P$ -doped layer acquires metal-like characteristics. Indeed, with an increase in the local temperature, the signal-SPP dispersion is rapidly modified as seen in **Figure 5-2(a)**. For fixed operation frequency  $f_o = \omega_o/2\pi = 30$  THz and constant applied bias ( $V = 1.12$  V), the SPPs can travel across the device which is exemplified by the fact that the effective refractive index  $n_{SPP}$  of these surface modes, is larger than the refractive index  $n_p$  of the  $P$ -doped layer. As the lattice temperature approached the critical, the SPP dispersion curve is shifted and a refractive index mismatch between SPPs in the drift diffusion region  $n_{SPP}(\omega_o, V, T)$  and in the rest of the device  $n_{SPP}(\omega_o, V, T = 0)$  is observed. This immediately leads to reflection and signal attenuation at the active zone establishing the OFF-state.

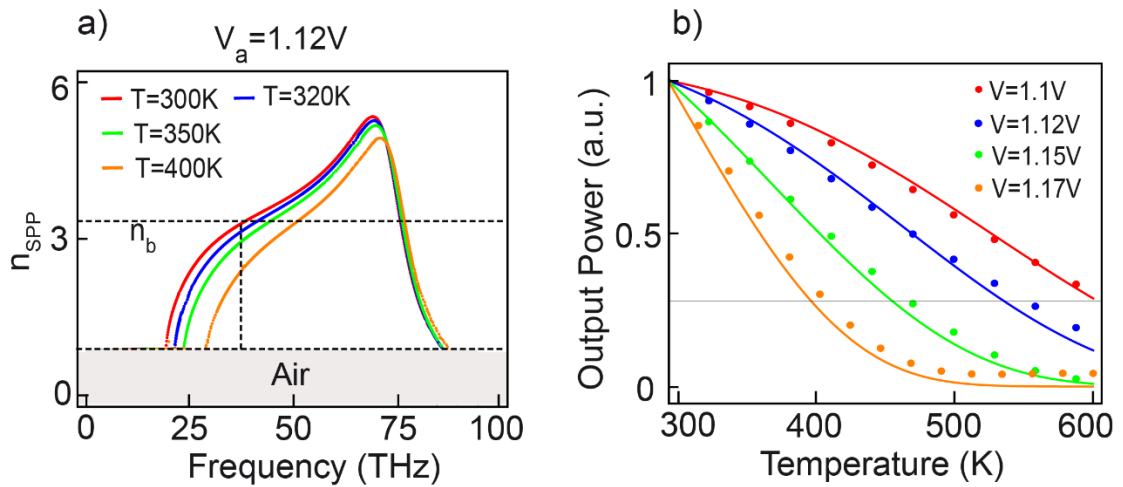


**Figure 5-2:** The Surface Plasmon Polaritons (SPPs) dispersion at constant external bias voltages  $V_a = 1.12 V$  and different lattice temperature for (a) Si with doping concentrations;  $N_A = 1 \times 10^{20}$ ,  $N_D = 4 \times 10^{20} cm^{-3}$ . (b) The SPPDt transmittance for Si at obtained using the self-consistent Multiphysics model (dots) and compared to the WKB approximation (solid lines). In the calculations the operation frequency is set at 30 THz, the thickness of the  $P$ -type layer is  $d = 1.5 \mu m$ ,  $n_b$  identifies the refractive index of  $P$ -layer and the overall length of the active drift-diffusion region is fixed at  $w = 4 \mu m$ .

Preliminary results based on the WKB and **Eq. 5-2** are shown in **Figure 5-2(b)**. In the numerical calculations, we have used,  $N_A = 10^{20} cm^{-3}$ ,  $N_D = 4 \times 10^{20} cm^{-3}$ ,  $f = 30$  THz,  $V \in (1.1, 1.12, 1.15, 1.17)V$  and  $E_g(T)$  as specified in the above section. In the calculations, we used relevant experimental data for Si. The model predicts a decay of the signal with an increase in the temperature. The temperature range across which the SPPDt is switched OFF depends on a variety of parameters including operation frequency,  $\omega$ , acceptor,  $N_A$  and donor,  $N_D$ , concentrations, applied voltage and the device spatial characteristics specifically the width of the drift-diffusion zone. We could attain a sharp decay and faster response for larger applied voltage provided  $V < V_c$ . As depicted in **Figure 5-2(b)** signal modulation surpassing -20 dB can be achieved for a temperature change of as little as 10 K. The numerical data is also compared to an analytical theory

based on the Wentzel-Kramers-Brillouin (WKB) showing a remarkable correlation between the two results.

### 5.3.1 Thermo-optic Co-efficient at the doped PN-interface

The dependence of the surface plasmon refractive index ( $n_{spp} = k_{spp}/k_0$ ) on the lattice temperature is investigated at different applied voltages. The result in **Figure 5-3**, clearly shows that high thermo-optic co-efficient of  $\frac{dn_{spp}}{dT} \sim 0.3K^{-1}$  at the drift-diffusion region. Such high thermo-optic co-efficient suggests that the SPPDt is the promising all-optical plasmonic switch. Here, the effect of  $n_{spp}$  can be analysed using the Drude Model for semiconductors, in which the change in  $n_{spp}$  is mostly due to the intrinsic concentration of the *P*-layer.

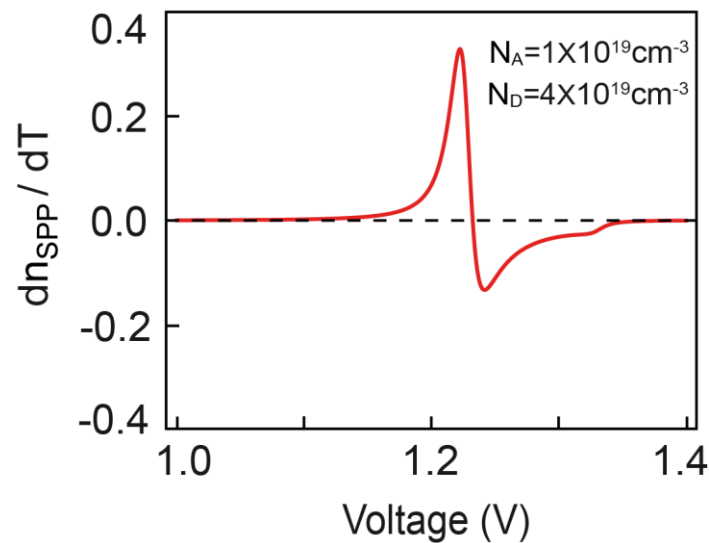


**Figure 5-3:** Thermo-optic co-efficient at doped PN-junction.

### 5.3.2 Numerical Analysis

Under steady ambient conditions with the control beam switched OFF, the electron concentration in the  $P$ -layer is below the critical and the SPPDt is in ON state (see **Figure 5-4(a)** & **Figure 5-4(b)**).

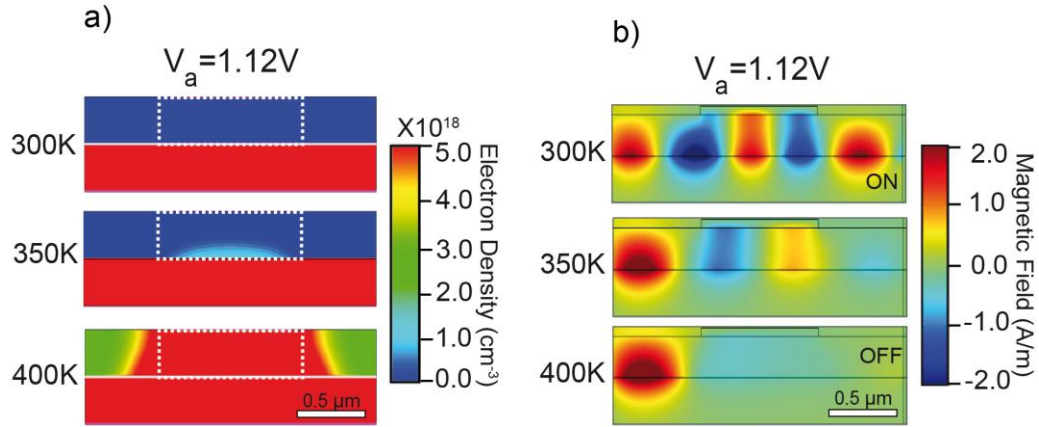


**Figure 5-4:** (a) Steady-state minority carrier concentration profiles at a constant applied voltage  $V_a = 1.12\text{ V}$  and different lattice temperature  $T = (300\text{ K}, 350\text{ K}, 400\text{ K})$ . (b) SPP propagation along the length of the device.

Once the control SPP is switched ON, it brings additional electromagnetic heating, increasing the local temperature in the drift-diffusion zone. The temperature increase depends on the frequency range of operation, device geometry, choice of semiconductor and total power density of the control beam. In the simulations, we have used a control beam power density of  $50\text{ mW}\cdot\mu\text{m}^{-2}$ , a typical value used in experiments involving SPP. This power level is sufficient to raise the local temperature by 40 K and switch OFF the signal, providing a signal modulation of -14 dB. The presented preliminary data, based on the WKB approximation and the exact numerical calculations, demonstrates that the SPP propagating at the  $PN$ - junction interfaces are subject to an

exceptionally strong thermo-optical effect that is not commonly observed in nature but is due to the abrupt electron concentration profile at the space charge region.

### 5.3.3 Effect of Doping

There is a direct relationship between the acceptor concentration and the critical temperature. The decrease in the  $P$ -layer concentration leads to a decrease in the critical temperature. **Figure 5-5** depicts the SPP transmittance as a function of  $N_A$  and lattice temperature.

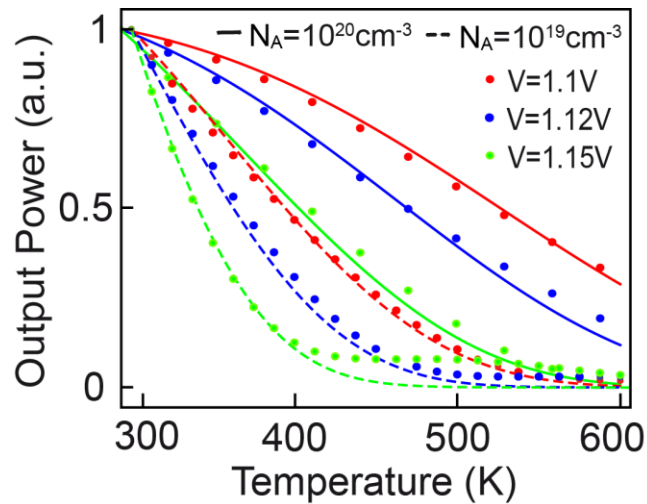


**Figure 5-5:** The SPPDt transmittance for Si at different  $P$ -doping concentrations and different external voltage  $V = (1.1 V, 1.12 V, 1.15 V)$ . are obtained using the self-consistent Multiphysics model (dots) and compared to the WKB approximation (solid lines). In the calculations the operation frequency is set at 30 THz, the thickness of the  $P$ -type layer is  $d = 1.5 \mu m$  and the overall length of the active drift-diffusion region is fixed at  $w = 4 \mu m$ .

For a lower doping concentration, we can see that the SPPDt attains OFF-state for lower critical temperature  $T_c$ . Here, for the external voltage of  $V_a = 1.12 V$  and a lattice temperature of  $T = 350 K$ , the device with  $N_A = 10^{19} cm^{-3}$  attains 50% more modulation in comparison with a device doped with  $N_A = 10^{20} cm^{-3}$ . Using the self-consistent model, we will have established the parametric range for the acceptor doping

concentration which can provide critical temperatures less than 350 K and signal modulation no less than -10 dB.

#### 5.3.4 Effect of Operational Frequency

The SPPDt operation strongly depends on SPP frequency,  $\omega$ . **Figure 5-6** depicts the SPP transmittance as a function of operational frequency and lattice temperature.

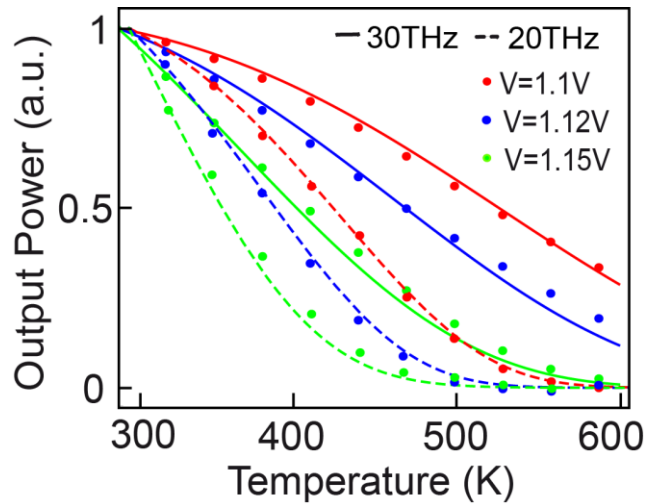


**Figure 5-6:** The SPPDt transmittance for Si at different operational frequencies and different external voltage  $V = (1.1 V, 1.12 V, 1.15 V)$  are obtained using the self-consistent Multiphysics model (dots) and compared to the WKB approximation (solid lines). In the calculations, the thickness of the  $P$ -type layer is  $d = 1.5 \mu m$  and the overall length of the active drift-diffusion region is fixed at  $w = 4 \mu m$ .

For instance, the critical temperature increases with  $\omega$  and the chosen SPP operation frequency will affect the localization and propagation characteristics of the SPP modes. Using the self-consistent model, we have performed parametric analysis for two frequencies, 30THz and 20THz. Here, we can clearly see that the device with a doping concentration  $N_A = 1 \times 10^{20}$ ,  $N_D = 4 \times 10^{20} cm^{-3}$  operates for critical temperatures less than 350 K, signal modulation no less than -10 dB for the operational frequency of 20 THz and applied voltage of  $V = 1.12 V$ .

#### 5.4 SPPDt-Response Times (Transient Analysis)

The speed at which the optical properties of the  $P$ -layer switches between dielectric ( $\epsilon_p > 0$ ) to metallic ( $\epsilon_p < 0$ ) and vice-versa depends on the rise time of the local temperature, which itself depends on the thermal diffusion coefficient of the material, the size of the device, operation frequency, and the control signal power density. Using dimensional analyses of the time dependent heat equation  $\rho c_p \partial_t T(\vec{x}, t) = k \nabla^2 T(\vec{x}, t) + Q_J(\vec{x}, t)$ , we can get rough estimates of the expected characteristic times of the SPPDt, namely  $\tau = l^2/\alpha$ , where  $\alpha = k/\rho c_p$  is the thermal diffusivity of the semiconductor material and  $l = l_{spp}$  is the characteristic length scale which in our case coincides with the SPP effective mode size. Solving the heat diffusion equation analytically gives a set of increasingly smaller time scales:  $\tau_n = l^2/\alpha \pi^2 (2n + 1)^2$ , where  $n = 0, 1, 2, \dots$  and a steady state achieved for times of the order of  $\tau_0$ . A set of characteristic times were estimated by fixing the operation frequency at 30 THz,  $N_A = 10^{19} \text{ cm}^{-3}$ ,  $N_D = 5 \times 10^{19} \text{ cm}^{-3}$ , for the four semiconductor materials of interest and are shown in Table 1. Furthermore, depending on the input power, the switching of the device can be achieved even before the steady-state is established, hence for times  $\tau < \tau_0$ . As shown in **Table 5-1**, silicon is the promising material with high switching rates due to high conductivity.

**Table 5-1:** SPPDt characteristic times.

$\tau_n$	GaAs	InAs	InSb	Si
$\tau_0$	45.4 ps	74 ps	88 ns	17.6 ps
$\tau_1$	16.3 ps	26.7 ps	31.7 ps	6.3 ps
$\tau_2$	8.3 ps	13.6 ps	16.2 ps	3.2 ps

### 5.5 SPPDt Logic Gates

The all-optical SPPDt impute waveguide elements can potentially be used to substitute one of the fundamental units in a microprocessor: the logic gate. The ON and OFF state pertaining to the logic gates correspond to the ubiquitous ones and zeroes found in binary language. Thus, logic gates have a necessary role within computer systems that are limited by the speed of their ON-OFF switching. Using the SPPDt, we will have designed the fundamental NAND/NOR diode logic by interconnecting the SPPDt (see **Figure 5-7**).

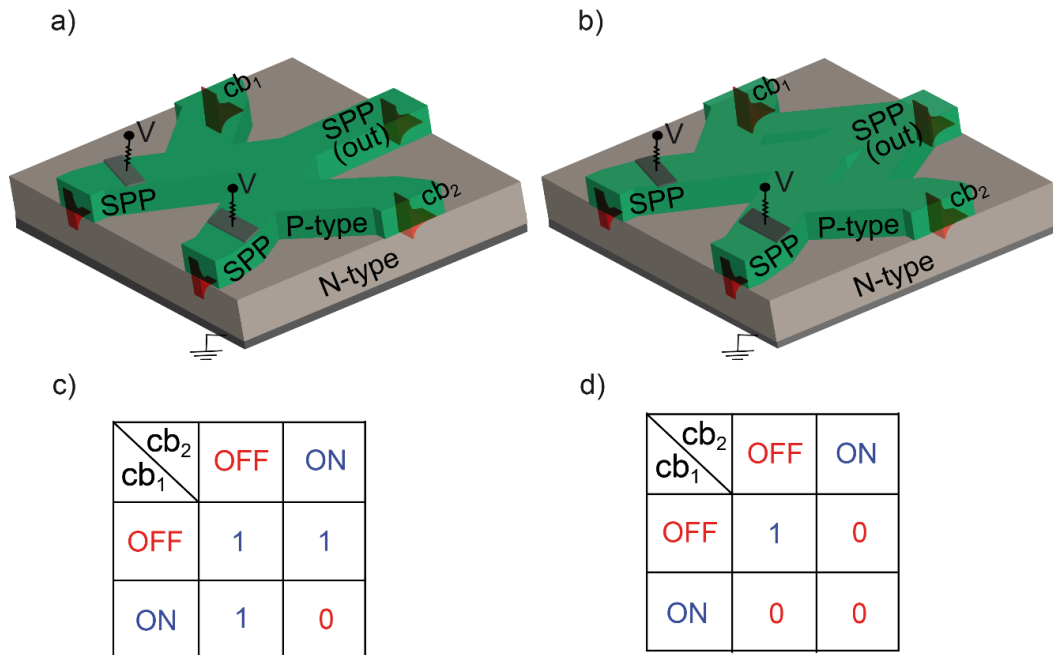


**Figure 5-7:** (a,b) Schematic of the TSPD logic (NAND and NOR) (c,d) Logic table corresponding to the NAND and NOR gates, respectively.

The logic gates operation is through the thermo-optic nonlinearity. The applied voltages will be fixed (below or above the critical depending on the gate) and the output will depend on the power densities of the two impute SPP waves. For instance, in the absence of a control beam, the input SPPs interact constructively at the Y-junction, and the signal is transferred establishing the “ON” states for both NAND and NOR gates. In the presence of the control beam ( $cb_1 = OFF$ ,  $cb_2 = ON$  or  $cb_1 = ON$ ,  $cb_2 = OFF$ ), the SPPs from one of the impute waveguides is transmitted in the case of the NAND gate (“ON” state) and reflected in the case of a NOR gate (“OFF” state) due to high thermo-optic effect at the active region. When both input control beams are ON, there is no transmission and both gates are in “OFF” state. As part of this project, a practically feasible design that is consistent with the CMOS technology will be provided.

## **CHAPTER 6**

### **SURFACE PLASMON ENHANCEMENT IN SELECTIVE LASER MELTING PROCESSES**

As discussed in the previous chapters, one of the most fascinating aspects of SPPs is the way light is channeled using the system geometries and has been used in a wide range of application. Extreme confinement and light trapping can convert the electromagnetic energy into heat with high efficiency and thus can fasten the initiation of the melting in SLM powders. The fundamental physical processes involved in SLM are complex and include scattering and absorption of laser radiation into highly heterogeneous metal powders, heat transfer, the formation of molten pools and its solidification, all within multiple lengths and timescales.

In this chapter, we perform a comprehensive multi-physics study of the complex phenomena associated with light-matter interactions in metal powder beds pertaining to SLM. A numerical framework is developed which self-consistently solves the Maxwell's and Heat equations to study the relevant electro and thermodynamic phenomenon. This model allows for accurate simulations of the excitation of the gap, bulk, and surface electromagnetic resonance modes, the energy transport across the powders, time-dependent local permittivity variations at high powers, and the thermal effects (Joule heating) due to electromagnetic energy dissipation. We have acquired numerical data representing the local laser heating and temperature profiles for steady-state and transient

illumination. The numerical results are compared with a developed semi-analytical model showing an excellent agreement for powder beds consisting of titanium particles with sizes ranging from hundreds of nanometers up to tens of microns. The analytical model provides a qualitative and quantitative description of the volumetric temperature rise, critical laser power, saturation temperature and deposition rates as a function of various optical and thermometric parameters. Finally, specific guidelines are outlined for a potentially significant increase in the SLM energy efficiency and deposition rates.

### 6.1 Thermo-optical Model

In a typical SLM process, there are two competing mechanisms that are primarily responsible for the initiation of melting in the powder bed. The first mechanism is related to complex light-matter interactions such as multiple reflections and scattering while the second is associated with heat re-distribution within the powder bed, black-body radiation, and conduction/convection heat transfer. To account for these strongly coupled effects, a self-consistent thermo-optical model is developed. Full-wave finite difference (FD) calculations of the optical phenomena manifested within the powder bed are performed using the COMSOL Electromagnetic Module. The thermal effects due to Joule heating are accounted for by the COMSOL Heat Transfer Module. A seamless integration between the two physical modules is accomplished by developing a MATLAB based facilitator code. The developed code shares the inter-dependent physical parameters between the two separate modules and allows for self-consistent steady-state and time-dependent simulations (see **Figure 6-1**).

Due to multiple length and time scales involved in SLM, specific mesh size and time step constraints must be strictly enforced. The electromagnetic simulations are stable

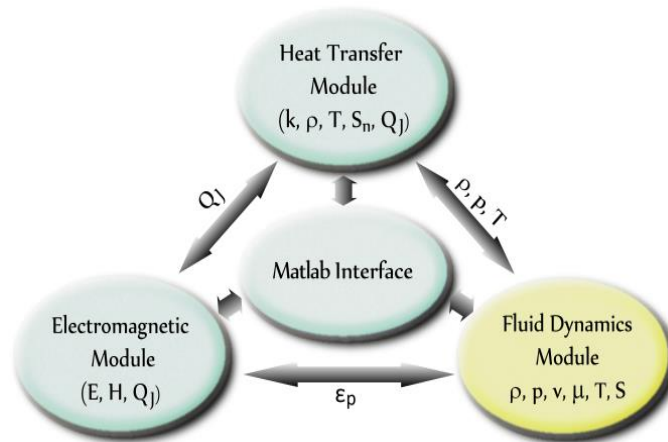


**Figure 6-1:** Self Consistent thermo-optic model.

and sufficiently accurate as long as we set the mesh size  $\Delta h = \delta/5$ , where  $\delta$  is the particles skin depth (the skin depth is generally much smaller than the wavelength  $\lambda$  at optical frequencies). For titanium, the skin depth is  $\delta = 22$  nm (for  $\lambda = 1.0$   $\mu\text{m}$ ) [108], and to accurately simulate the largest particle beds considered in this work (particle radius up to 10 microns), operational memory surpassing 30GB is required. Combined with adaptive meshing, this memory constrain is easily addressed even on an average workstation. Hence, the historical use of ray tracing methods is no longer a necessity and the simulation community should transition to exact numerical calculations of the electromagnetic phenomenon associated with SLM. Such transition can provide high fidelity codes that accurately capture new electromagnetic phenomenon such as excitation of surface electromagnetic states which are completely missed in commonly used ray approximation schemes.

Apart from the spatial considerations, the self-consistent thermo-optics model has to capture all relevant time scales properly as well. The numerical solutions of the heat equation are stable provided the time step is  $\Delta t < \frac{1}{2\alpha_P} \Delta h^2 = \frac{1}{50\alpha_P} \delta^2 = 50\text{ps}$ , where  $\alpha_P$

is the particle thermal diffusivity (titanium is assumed in the estimate). This time step is sufficiently larger compared to the transient times in the electromagnetic simulations. As a result, steady-state solutions of the Maxwell's equations can be generated in each time step, and the local Joule heating can be incorporated in the heat transfer module. This iterative process continues until saturation in the particle temperature or onset of melting is reached at macroscopic times.

#### 6.1.1 Numerical Simulation-Isolated Particle

To test the developed thermo-optical model, we first consider a simple configuration comprising of a free-standing titanium particle, (see **Figure 6-2(a)**). As we consider extreme thermodynamic conditions, actual temperature dependent thermo-physical parameters are considered in the model [109] [110]. As the first step, we consider steady-state conditions where the absorption scattering cross-section obtained by the finite-difference model, shown in **Figure 6-2(a)**, is found to match the Mie formalism [111]. The particle absorption exhibits resonance behavior for small particles and asymptotically approaches the absorbance from a flat metal at large particle sizes. In **Figure 6-2(b)**, we observe that while the local Joule heating can be highly inhomogeneous and localized within the particle skin depth, the corresponding steady-state temperature is near uniform. This is attributed to the fact that a homogenization of the temperature profile inside the particle is established rapidly and within a characteristic time  $\tau \approx R^2/\alpha_p$ , where  $R$  is the particle radius. For titanium particles with radius  $R = 5 \mu\text{m}$ , the corresponding characteristic time is  $\tau \sim 2.7 \mu\text{s}$ .

To better understand the temporal dynamics of the particle heating process, we have performed a set of time-dependent simulations shown in **Figure 6-2(c)** and **Figure 6-2(d)**.

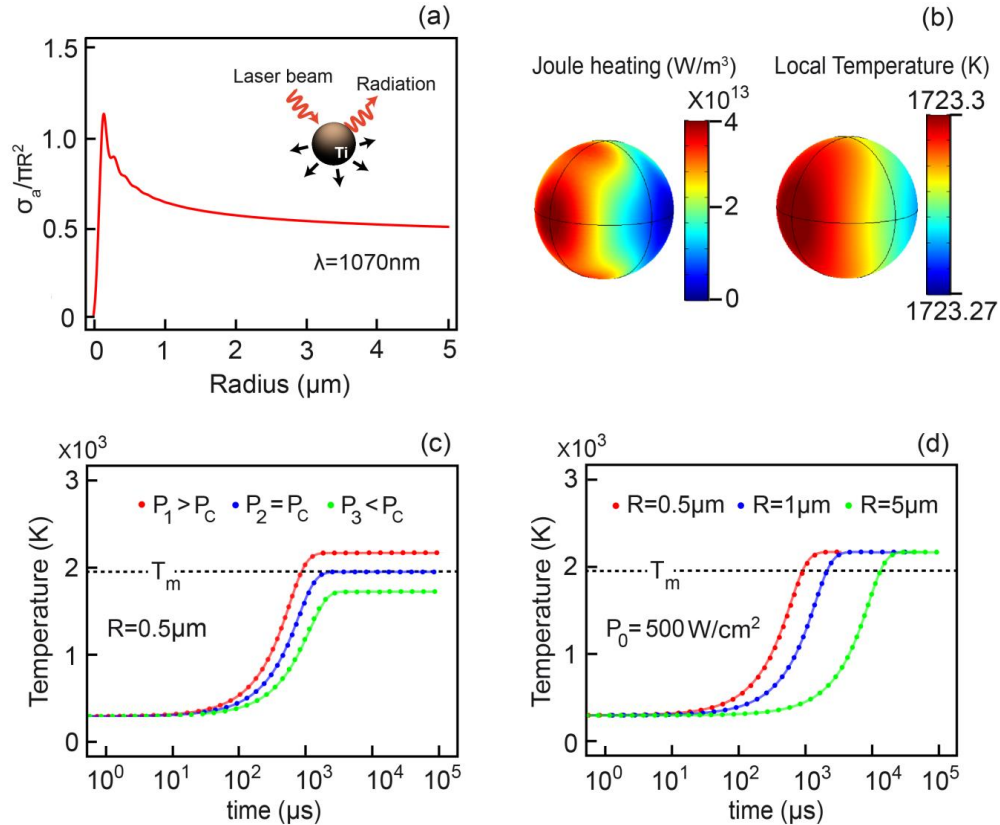


**Figure 6-2:** (a) Absorption cross-section of isolated titanium (Ti) particle using the Mie theory. At the chosen operational wavelength  $\lambda = 1.070 \mu\text{m}$  (corresponding to Concept Laser Mlab cusing R 3D printer [112]) the refractive index of titanium is  $n_p = 3.4740 + i4.0113$  [113]. (b) The local Joule heating is found to be predominantly along the polarization direction of the impinging radiation and the steady state temperature profile of the particle ( $R = 0.5 \mu\text{m}$ ) irradiated with laser power density  $P_0 = 200 \text{ W}/\text{cm}^2$  is found to be remarkably homogeneous. (c, d) The volume-averaged particle temperature as a function of the elapsed time is obtained using the self-consistent multiphysics model (dots) and compared to the analytical result given by **Eq. 6-3** (solid lines). In (c) the size of the particle is fixed at  $R = 0.5 \mu\text{m}$  and irradiated with three different laser power densities  $P_0 = (200, 320, 500) \text{ W}/\text{cm}^2$ , while in (d) three different particle sizes are investigated at a fixed laser power density  $P_0 = 500 \text{ W}/\text{cm}^2$ . In the calculations, the operational wavelength is set at  $1.070 \mu\text{m}$ , and the particle melting temperature is shown with dashed line.

A linear increase of the volume averaged temperature with time is observed up until the onset of saturation due to black-body radiation. In the simulations, various conditions related to the particle sizes and input laser power densities are investigated. **Figure 6-2(c)** depicts the temperature rise and saturation for three separate laser power densities and titanium particle with fixed size  $R = 0.5 \mu\text{m}$ . The power densities are chosen such that we can separately investigate the three operational regimes where the saturation temperature is lower, equal and higher compared to the particle melting temperature  $T_m = 1941 \text{ K}$  [114]. For laser power densities below the critical  $P_0 < P_c = 320 \text{ W/cm}^2$ , the temperature saturates at a maximum value lower than the particle melting temperature. At higher powers  $P_0 > P_c$ , the time to melt is inversely proportional to the power density and depends linearly on the particle size (see **Figure 6-2(d)**). In all investigated cases and for laser power densities typical for SLM, the onset of melting or temperature saturation (for power densities less than the critical  $P_0 < P_c$ ) happens within a few milliseconds. This time scale is much larger than the local temperature homogenization time  $\tau$  which as we have shown above is within a few microseconds. The existence of two separate time scales pertaining to the SLM process allows for the development of a simple analytical model which we present next.

### 6.1.2 Analytical Model

Starting with the local form of the heat equation, performing averaging over the particle volume and using the divergence theorem, we arrive at

$$\rho c_p V \frac{d\langle T(t) \rangle}{dt} = k_p \oint \vec{\nabla} T(\vec{r}, t) \cdot d\vec{S} + \dot{Q} \quad \text{Eq. 6-1}$$

where  $\langle T(t) \rangle = V^{-1} \int T(\vec{r}, t) dV$  is the volume average temperature,  $V$  is the particle volume,  $\dot{Q} = \sigma_a P_0$  is the Joule heating rate which depends on the incident laser power

density  $P_0$  and the absorption cross-section  $\sigma_a$ . The heat flux at the surface is due to conduction/convection and radiation losses and can be written as a function of the average surface temperature  $\langle T(t) \rangle_R = S^{-1} \int T(\vec{r}, t) dS$  as follows

$$\rho c_p V \frac{d\langle T(t) \rangle}{dt} = -hS(\langle T(t) \rangle_R - T_a) - \epsilon \sigma_B S (\langle T(t) \rangle_R^4 - T_a^4) + \dot{Q} \quad \text{Eq. 6-2}$$

where  $T_a = 300 \text{ K}$  is the ambient temperature,  $\sigma_B$  is the Boltzmann constant, and  $\epsilon = \sigma_a / \pi R^2$  is the emissivity. For stagnant flow, the heat transfer coefficient is given as  $h = k_a / R$ , where  $k_a$  is the thermal conductivity of the buffer gas. For times sufficiently larger compared to the thermalization time  $t \gg \tau$  but smaller compared to the time to melt (or saturation at lower powers), we can equal the average volumetric and surface temperatures  $\langle T(t) \rangle = \langle T(t) \rangle_R = T(t)$ . In this case **Eq. 6-2** has an exact analytical solution which however is rather a combuster and not very illuminating. Instead, we recognize that SLM ambient conditions involve buffer gases with low thermal conductivities and high powder bed temperatures for which the conduction term can be neglected. The rate equation **Eq. 6-2** then has a simple analytical solution in implicit form

$$t = \frac{t_0}{2} \left( \tan^{-1} \left( \frac{T}{T_s} \right) + \tanh^{-1} \left( \frac{T}{T_s} \right) - \tan^{-1} \left( \frac{T_a}{T_s} \right) - \tanh^{-1} \left( \frac{T_a}{T_s} \right) \right) \quad \text{Eq. 6-3}$$

where  $t$  is the time since the onset of heating,  $t_0 = \frac{\rho c_p R}{3 \epsilon \sigma_B T_s^3}$  is a characteristic time

corresponding to reaching saturation, and  $T_s = \left( T_a^4 + \frac{P_0}{4 \sigma_B} \right)^{1/4}$  is the saturation

temperature which is independent on the particle size. For a given melting

temperature,  $T_m$ , the theory predicts a critical power density  $P_c = 4 \sigma_B (T_m^4 - T_a^4)$  required

to initiate the melting process. For high powers such that  $T_a \ll T_m \ll T_s$ , a linear rise of

temperature is expected  $T \approx T_a + (t/t_0) T_s$ , and the time to melt can be estimated as

$t_m = \frac{t_0 T_m}{T_s} = \frac{4\rho c_p R T_m}{3\epsilon P_0}$ , showing linear dependence with the particle size and inverse

dependence on the incident power. This is consistent with the numerical findings in **Figure 6-2(c, d)**, where we compare the analytical theory with the numerical results for different incident power densities and particle sizes. We observe an excellent agreement both in terms of predicting the transient behavior and steady state temperature. As discussed above, the analytical model is only applicable if a near homogeneous temperature is observed for macroscopic times or provided  $t_m \gg \tau$ . This condition sets a limit for the laser power density  $P_0 < k_p T_m / R$ , beyond which the analytical model cannot be trusted. For titanium particles with radius  $R = 1 \mu m$ , the power densities must be lower than  $4000 \text{ W/cm}^2$ .

## 6.2 Dense Metal Powders

The developed thermo-optical models have also been extended to study the dense metal powders used in SLM. The system under consideration consists of a layer of touching titanium spheres resting on a substrate representing the already melted pool and is depicted as an insert in **Figure 6-3**. In the numerical simulations, the metal powder is represented as a periodic arrangement of closely packed particle in a square lattice with near neighbor interactions taken into account by imposing periodic boundary conditions across the system (in the plane parallel to the substrate). The calculated absorptance under steady-state conditions, normal laser incidence, fixed wavelength, and varying particle sizes is shown in **Figure 6-3**.

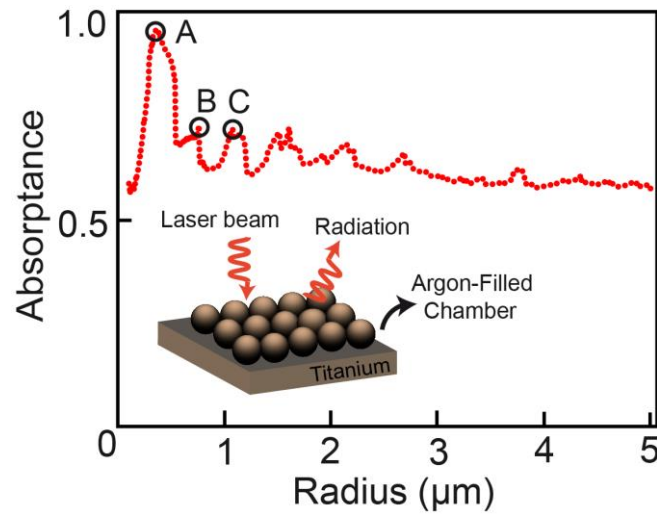


**Figure 6-3:** Absorbance versus particle size for closely packed (touching) titanium spheres arranged in a square lattice on top of a titanium substrate (see insert). In the calculations, the laser radiation is normal to the particle bed and the laser wavelength is set at  $1.070 \mu m$ . Morphologically dependence resonances are manifested due to electromagnetic interactions between neighbors and excitation of surface plasmon states (points A, B, and C).

Compared to a single non-interactive particle (see **Figure 6-2(a)**), here we observe absorbance with added complexity. This added complexity is predominantly due to inter-particle field interactions that provide additional channels for excitation of morphology-dependent resonances facilitated by surface plasmon polaritons (SPPs). As discussed in previous chapters, SPPs are the transfer magnetic (TM) surface modes that propagate at the metal-dielectric interfaces. For planar surfaces, the SPP wavevector is given as  $k_{sp} = (\omega/c)\sqrt{\epsilon_d\epsilon_p/(\epsilon_d + \epsilon_p)}$ , where  $\epsilon_d$  and  $\epsilon_p$  are dielectric and metal permittivities, respectively. For large metal particles and neglecting curvature effects, the leading SPP resonances can be obtained using the standing-wave condition  $\text{Re}[k_{sp}R] = 2n$ , where  $n = 1, 2, \dots$ . For titanium particles illuminated with laser radiation at fixed free space wavelength  $\lambda = 2\pi c/\omega = 1.070\mu m$ , we obtain a set of resonance particle sizes  $R = 0.34 \mu m, 0.680 \mu m, 1.02 \mu m, \dots$ . These correlate rather well with the absorbance peaks

in **Figure 6-3**: manifested for  $R = 0.37\mu\text{m}$  (A point),  $R = 0.752\mu\text{m}$  (B point), and  $R = 1.07\mu\text{m}$  (C point).

As seen in **Figure 6-4** as the particle size increases, higher order SPP resonances are excited. The quality factor of these resonances generally decreases with the order and

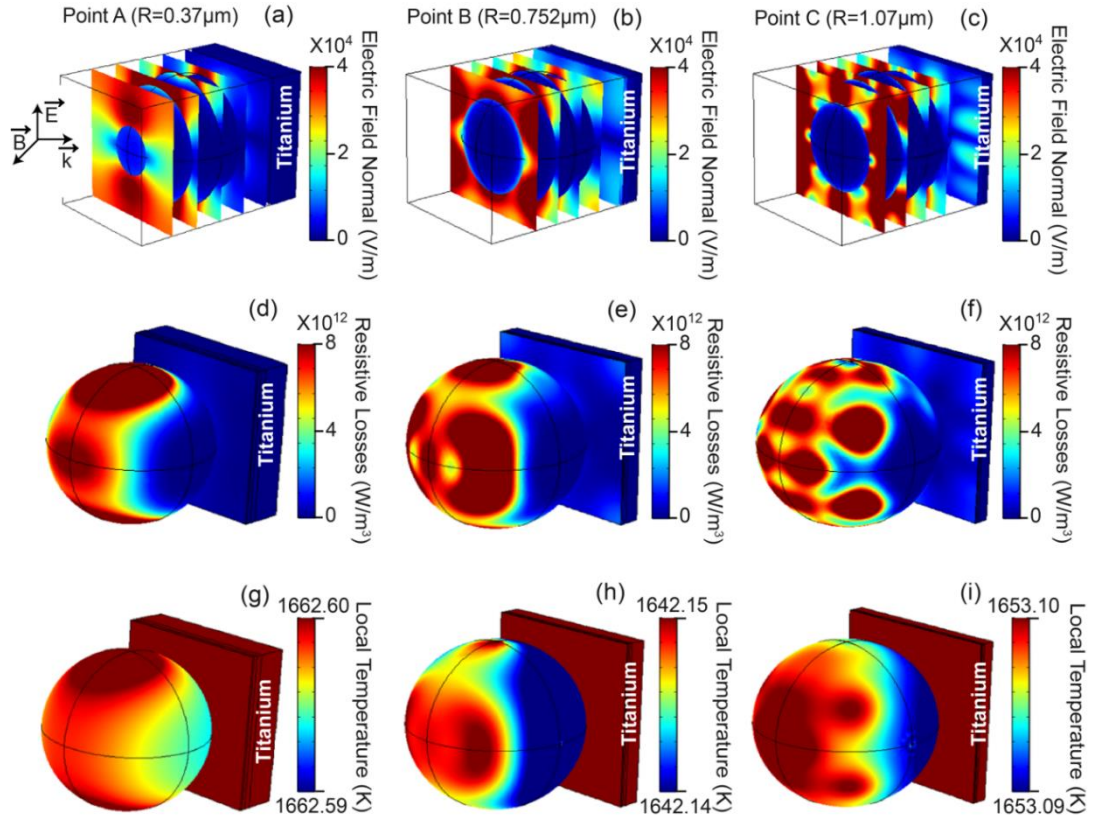


**Figure 6-4:** (a, b, c) Local electric field profiles due to impinging (from the left) laser radiation showing excitation of standing surface waves associated with SPPs. (d, e, f) The SPP modes induce localized Joule heating which is found to be predominantly on the polarization direction of the impinging radiation. (g, h, i) The local steady-state temperature on the particle surface shows a highly homogeneous distribution despite the strongly localized Joule heating. In the calculations, the operational wavelength is set at  $1.070\mu\text{m}$  and the incoming laser beam power density is  $P_0 = 40\text{ W/cm}^2$ .

as a result, gradual disappearing of the resonance structure is observed for large particles  $R > 5\mu\text{m}$ , with the absorbance approaching  $A \rightarrow 61.5\%$  which is consistent with estimates using the ray tracing method [64].

The numerically obtained steady-state electric field, Joule heating and temperature distributions for titanium powders with particle sizes supporting SPP resonances are depicted in **Figure 6-4**. Close inspection of the local electric field profiles provides further validation of the proposed explanation of the resonance effects as facilitated by SPP standing-waves (see **Figure 6-4(a-f)**). While the local electric field and corresponding Joule heating are aligned with the laser polarization direction and show highly inhomogeneous profiles, the steady-state surface temperature is remarkably homogeneous (**Figure 6-4(g-i)**). As discussed in the preceding sections, this is due to fast thermalization times sufficiently larger than the homogenization time  $t \gg \tau = R^2/\alpha_p$ . This fact, similarly to the case of a free-standing particle, allows the implementation of the analytical model **Eq. 6-3** with few simple modifications. To account for the change in geometry (dense powders) in the model, the Joule heating rate is now given by  $\dot{Q} = AP_0S$ , the emissivity is equal to the absorptance  $\epsilon = A$ , and  $S = 4R^2$  is the cross-sectional area of the unit cell (touching spheres).

The temporal response of the volume averaged particle temperature calculated using the numerical method and analytical theory is shown in **Figure 6-5**. In the calculations, we consider again a set of input power densities and particle sizes were chosen to exemplify the various regimes of operation.

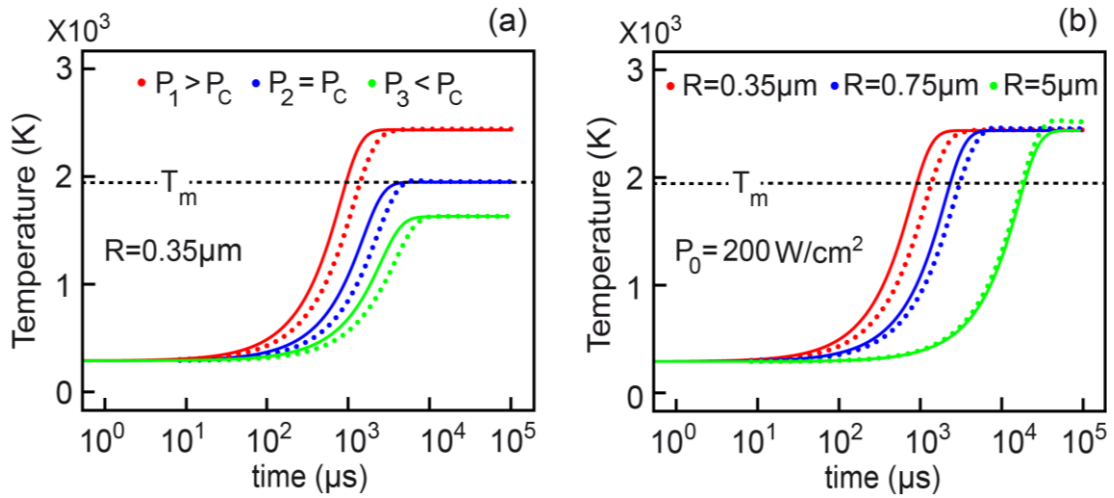


**Figure 6-5:** The volume-averaged particle temperature as a function of the elapsed time for a periodic array of titanium particles obtained using the self-consistent multiphysics model (dots) and compared to the analytical result (solid line). (a) The size of the particle is set to match the  $n = 1$  SPP resonance (point A) and is irradiated with three different laser power densities  $P_0 = (40, 82, 200) \text{ W/cm}^2$ . (b) The temperature versus time calculated for periodic arrays of titanium particles with varying sizes and irradiated with a constant laser power density  $P_0 = 200 \text{ W/cm}^2$ . In the calculations, the operational wavelength is set at  $1.070 \mu\text{m}$ .

**Figure 6-5(a)** depicts the temperature versus time for a periodic array of  $0.35 \mu\text{m}$  sized particles (matching the  $n = 1$  SPP resonance) at input powers below, at and above critical. Similar behavior to that of a free-standing particle is observed. The main difference compared to the free-standing particle is that for dense powders, the critical laser power density is reduced by a factor of  $\approx 1/4$ . This is consistent with the shading effect due to the adjacent particles which can reabsorb the thermal radiation if the angle of emission is  $\theta > \theta_M$ .

For closely packed powders, the angle of the radiation window is  $\theta_M = \tan^{-1}(2)$  and the critical power is reduced by a factor proportional to the radiation solid angle fraction  $\Omega_R/4\pi = \frac{1}{2} \int_0^{\theta_M} \sin(\theta) d\theta = 0.27 \approx 1/4$ . In all three cases, the analytical theory closely matches the numerical results and melting conditions are reached within a few

milliseconds. Similar consistency is observed at fixed incident power density and varying particle sizes as shown in **Figure 6-5(b)**. In the linear regime, the time to melt  $t_m = \frac{\pi\rho c_p R T_m}{3AP_0}$  is proportional to the particle radius which is clearly evident in the presented data. Note, in the presentation we use log-normal plots to capture the behavior for large range of times.

The presented study provides an insight into the intra- and inter-particle heat transfer processes within the powder bed. Inter-particle heat transfer is typically governed by conduction into the buffer gas (argon in our case), contact conduction between the particles and to the substrate they reside on. For typical SLM buffer gasses and low pressures, the conductive transfer is weaker compared to radiation losses and can be neglected for power densities  $P_0 < k_p T_m / R$ . When considering the intra-particle heat transfer, the time scale defining the transient processes are typically much smaller than the time scales governing particle melting. In other words, under typical SLM conditions, conductive homogenization of non-uniform energy and temperature distributions across the powder bed and inside the individual particles happen extremely fast, and we can safely consider the metal powder under near uniform temperature at macroscopic times.

### **6.3 Selective Laser Melting-Volumetric Deposition Rate and Energy Efficiency**

Some of the major obstacles for the widespread implementation of metal printing based on SLM is the time-consuming processing which can take hours to create a single component. Increasing the printing rate and improving the energy efficiency are the main goals for the industry. To access possible strategies for such technology improvements, we have performed a systematic study of the volumetric deposition rate versus average particle size and input laser power density. The deposition rate is estimated as  $\dot{V} =$

$4\pi R^3 N/3t_m = \pi R W_0/3P_0 t_m$ , where  $N = S_0/4R^2$  is the number of particles within the laser beam spot area  $S_0$ ,  $W_0 = S_0 P_0$  is the incident laser beam power, and  $t_m = t_m(A, P_0, R)$  is the melting onset time which is a function of the absorptance  $A$ , power density  $P_0$  and average particle size. In **Figure 6-6(a)** we present the volumetric deposition rates for various laser power densities and particle sizes.

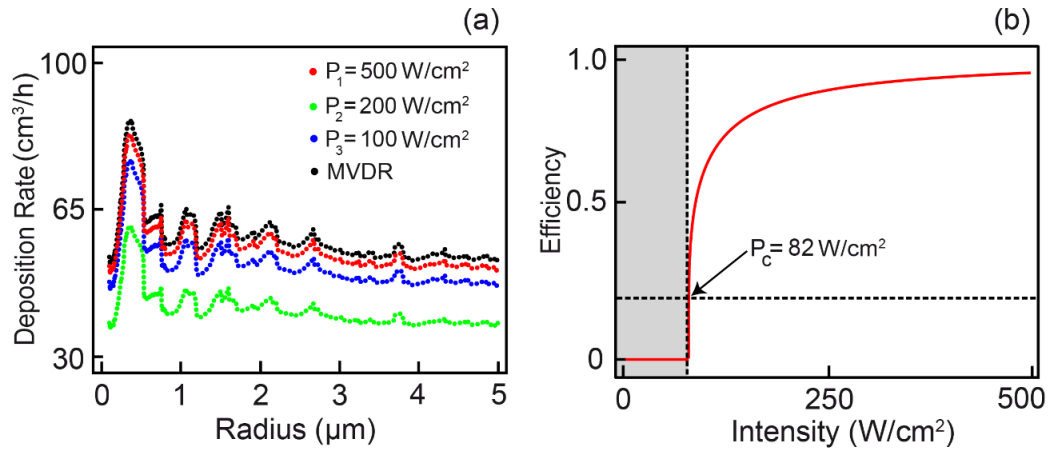


**Figure 6-6:** (a) Volumetric Deposition rate as a function of particle size and incident laser intensity. In the calculations the operational wavelength is set at  $1.070 \mu m$ , incident laser power as  $W_0 = 100 W$ . The periodic array of homogenous sized particle array is irradiated with three different laser power densities  $P_0 = (500, 200, 100) W/cm^2$ . The corresponding MVDR is depicted by black dots. (b) Efficiency as a function of incident laser intensity.

In the calculations, we have fixed the total laser power at  $W_0 = 100 W$ , typical for SLM printing machines [112] [115]. A substantial speed up could be achieved for powder beds with mean particles sizes that support excitation of SPP resonances and hence increased absorbtance. Increasing the laser power density or decreasing the laser spot size lead to an overall increase in deposition until it reaches a fundamental limit which we refer to as a maximum volumetric deposition rate (MVDR). This limit can be obtained from the rate equation **Eq. 6-3**, which is solved in the limit of high powers, rapid temperature rise and negligible radiation losses. Under these conditions the time to

melt is  $\tilde{t}_m = \rho c_p V (T_m - T_a) / 4AR^2 P_0$  and the maximum volumetric deposition rate is  $\dot{V}_{MVD R} = AW_0 / [\rho c_p (T_m - T_a)]$ , independent of the laser power density.

Apart from increasing the speed of the printing process, it is also important to study the SLM energy efficiency. The efficiency can be defined as the fraction  $\eta = U_p / U_L$  of the particle thermal energy  $U_p = \rho c_p V (T_m - T_a)$  to the laser energy  $U_L = \dot{Q} t_m$  deposited up to the onset of melting. The efficiency can also be written as the ratio between the times to melt with and without radiation losses,  $\eta = \tilde{t}_m / t_m$ , and is depicted in **Figure 6-6(b)**. The efficiency has a strong dependency on the incident laser powder density and goes to zero at the critical power. Interestingly, it is also found to be independent of the particle size and absorptance. This is due to the fact that  $U_L$  and  $U_p$  are both proportional to the particle volume, and in the case of energy losses due to radiation, only the thermal emissivity is simply proportional to the absorptance, which leads to saturation temperature independent on the absorbance and particle size.

However, at intermediate and high buffer gas pressures, the conductive heat transfer into the gas will start to play a more significant role. In this case, the efficiency will start to be sensitive to the powder bed particle size distribution. Overall, under typical SLM condition, it can be concluded that using smaller laser focus spot sizes, optimal powder density along with particle/grain sizes that support plasmonic resonances may substantially improve deposition rates and energy efficiency. Since optimization is achieved for particle size distributions tailored to the excitation of surface plasmon resonances, this points toward the need to develop powder beds consisting of particle sizes smaller than those currently used by the industry. Such a shift toward finer powder beds can also lead to higher morphological uniformity of the melt pools and hence

improved metallurgical microstructure of the printed parts, finer geometrical resolutions along with improved surface quality. However, it must be also recognized that using finer powder beds can also lead to issues related to clean up, contamination and layers deposition. If these technical issues are resolved, there is a clear path toward further improvements in the SLM technology.

# CHAPTER 7

## CONCLUSION AND FUTURE WORK

### 7.1 Concluding Remarks

In conclusion of this dissertation, we have introduced and demonstrated a novel optoelectronic switching device, i.e. surface plasmon polariton diode (SPPD), capable of operating at exceedingly high switching rates and signal modulation. The fast response of the device is achieved by active control of the propagation of surface plasmon polaritons (SPPs) along with a highly doped PN-junction. Multiphysics numerical code was developed to self-consistently model the electromagnetic, solid state, and the thermal response of the device. Using the developed Multiphysics model, we have studied the operational characteristics using three different semiconductor materials, Si, GaAs, and  $\text{In}_{0.53}\text{Ga}_{0.47}\text{As}$ . The performed steady-state and time-dependent numerical analysis suggests that an SPPD based on lattice matched  $\text{In}_{0.53}\text{Ga}_{0.47}\text{As}$  can operate at responsivities more than  $-600 \text{ dB} \cdot \text{V}^{-1}$  and data rates up to 50 Gbit/s.

Moreover, owing to the use of SPPs, the proposed optoelectronic switch can have physical dimensions substantially smaller compared to conventional optical devices. Likewise, tuning the thickness of the active drift diffusion region, doping concentrations and operational frequency suggests that SPPD can operate at signal modulation in excess of 18 dB and switching rates of up to 1 THz. Designs of the fundamental logic elements,

NAND and NOR gates, have been suggested and demonstrated. Finally, a practical design based on a set of coupling/out-coupling gratings is proposed for the experimental demonstration of the optoelectronic switch.

The experimental efforts in collaboration with UT Austin had led to Proof of Concept devices based on highly doped Silicon-on-Insulator (SOI) and lattice matched  $\text{In}_{0.53}\text{Ga}_{0.47}\text{As}$ . A step-by-step process is implemented in which the theory is matched to a set of control experiments, providing the critical data needed to refine the material parameters used in the theory. Two Figures of Merit (FOM) have been used to characterize the tradeoff between the SPP propagation losses and mode confinement for operation frequencies in the far-IR spectral range and III-V semiconducting materials and compounds consistent with the experimental capabilities. Performed comprehensive study of the SPPD steady-state and time-dependent I/O characteristics in conjunction with the experimental results that has led to in-depth understanding of the unique switching mechanism behind the SPPD, establishing a clear roadmap toward direct, electro-optical signal modulation at rates from a few kHz up to 1 THz, guide and accelerate the development of a prototype.

Furthermore, this dissertation also addressed the design and theory of all optical equivalent of an SPPD, where switching of SPPs is accomplished using a secondary control SPP modes, referred to as Surface Plasmon Polariton Diode (thermal) (SPPDt). Largely, the switching relies on the exceptionally strong thermo-optical nonlinearity present at the PN-junction. Full-scale simulations of the all-optical response of the SPPDt based on Silicon were performed demonstrating extremely fast switching for applied voltage higher than 1.1 V, and signal modulation of up to 24 dB. We have studied the

operation characteristics of the Si-device under steady-state conditions. Also, we identified the device critical temperature dependence on the acceptor doping concentration and frequency of operation. Practical designs of NAND and NOR SPPDt logic gates were proposed and studied. Possible applications of the SPPD as a high sensitivity temperature sensor were demonstrated.

Finally, for the first time, we have applied the concept of SPP to the field of SLM. For this, we have adapted the developed self-consistent Multiphysics code for SPPD and SPPDt, which simultaneously solves the Maxwell's and the heat transfer equations. The model used adaptive meshing and can be executed in parallel. The adapted model helps to understand the laser interactions with metal powder beds related to the SLM processes and studied the relevant electromagnetic and thermodynamic phenomenon. This allows full-wave calculations of spatial domains sufficiently large to model the SLM processes without the use of approximated methods such as ray tracing. The presented approach is easy to implement and provides a new direction for the simulation community for transition into exact numerical phenomena associated with SLM.

Using the developed numerical method, we have performed extensive studies of the local laser heating and temperature profiles for steady-state and transient illumination. It is observed that under typical SLM conditions, the deposited laser energy is thermalized within a time scale substantially shorter compared to the time to melt, leading to highly homogeneous temperature profiled across the powder beds. This allows the implementation of a simple analytical model to provide a qualitative and quantitative description of the volumetric temperature rise in the powder beds as a function of the various optical and thermometric parameters. Overall, our results show that metal powder

beds comprised of particle size distributions supporting surface plasmon polariton (SPP) resonances can greatly improve the absorption rate and hence the SLM volumetric deposition rate.

## 7.2 Future Work

### 7.2.1 Surface Plasmon Polariton Diode (SPPD)

One of the main goals of this dissertation is to design and assess the potential of excitation and fast optoelectronic control of SPPs at the interface of doped semiconductors. We have successfully accomplished all primary objectives related to the underlying working principle, general design assessment, parametric optimization of switching times and material characterization of SPPD. As a future work, we will focus on:

1. The transient response of the prototypes based on highly doped Silicon-on-Insulator (SOI) and lattice matched  $\text{In}_{0.53}\text{Ga}_{0.47}\text{As}$  will be further tested using a direct detection method (IR-detector) for modulation rates ranging from low (kHz) to moderate and high frequencies (few MHz up to 3 GHz).
2. A new on-chip electro-optical detection will be implemented. Experimental measurements, in conjunction with the theory, will be performed to establish the physical limitations and scaling laws governing the SPD 3dB bandwidth.
3. Experimental realization of an on-chip SPPD logic gates.

### 7.2.2 Surface Plasmon Polariton Diode (thermal) (SPPDt)

The second objective of this dissertation is to design and assess the potential of a fast all-optical analog of the SPPD, where the SPPs are controlled by a secondary electromagnetic mode at the interface of doped semiconductors. We have accomplished

objectives related to the underlying working principle, general design assessment, operation characteristics and parametric optimization under steady-state. Some of the areas of future work are:

1. SPPDt switching characteristics step and temporal response for Silicon and  $\text{In}_{0.53}\text{Ga}_{0.47}\text{As}$  using thermo-electro-optical model. Validate the results using the analytical methods.
2. Study the optical characteristics using different semiconducting materials and establish a roadmap to THz switching with transmission modulation higher than 90%.
3. Perform comprehensive Multiphysics modeling of SPPDt Logic gates (AND, NAND, OR and NOR).
4. To study a practical design based on a set of coupling/out-coupling gratings for the experimental demonstration of the SPPDt.

### 7.2.3 Multiphysics Modelling of SLM Process

The third objective of this dissertation is to perform a self-consistent thermo-optical model of the laser-matter interactions pertaining to SLM. Electromagnetic interactions and the thermal effects with the dense powder beds are investigated by means of full-wave finite difference calculations. Future work comprises of:

1. Perform analysis by considering realistic particle powder beds' configurations including (i) Compounds in the form of quasi-periodic lattices and (ii) Experimental relevant particle size distributions.
2. Perform particle shape optimization by considering spheroidal and shell configurations for improved absorption and heat transfer within the powder beds.

3. Study the requirements of the mean and standard deviation of the particle sizes in the powder bed to obtain insight towards the mechanical properties of the final manufactured part.
4. Integrate a fluid dynamics module in the code in order to understand the solid-liquid-solid phase transitions.

## BIBLIOGRAPHY

- [1] H. Sutter, “The free lunch is over: A fundamental turn toward concurrency in software,” *Dr. Dobbs J.*, pp. 1–9, 2005.
- [2] R. Zia, J. A. Schuller, A. Chandran, and M. L. Brongersma, “Plasmonics: the next chip-scale technology,” *Mater. Today*, vol. 9, no. 7–8, pp. 20–27, 2006.
- [3] S. A. Maier, M. L. Brongersma, P. G. Kik, S. Meltzer, A. A. G. Requicha, and H. A. Atwater, “Plasmonics—a route to nanoscale optical devices,” *Adv. Mater.*, vol. 13, no. 19, pp. 1501–1505, 2001.
- [4] E. Ozbay, “Plasmonics: Merging photonics and electronics at nanoscale dimensions,” *Science*, vol. 311, no. 5758, pp. 189–193, 2006.
- [5] M. L. Brongersma and V. M. Shalaev, “Applied physics. The case for plasmonics.,” *Science*, vol. 328, no. 5977, pp. 440–1, Apr. 2010.
- [6] D. A. Genov, R. F. Oulton, G. Bartal, and X. Zhang, “Anomalous spectral scaling of light emission rates in low-dimensional metallic nanostructures,” *Phys. Rev. B*, vol. 83, no. 24, p. 245312, Jun. 2011.
- [7] H. Abdeldayem, D. O. Frazier, W. K. Witherow, C. E. Banks, B. G. Penn, and M. S. Paley, “Recent advances in photonic devices for optical supercomputing,” in *Lecture Notes in Computer Science (including subseries Lecture Notes in Artificial Intelligence and Lecture Notes in Bioinformatics)*, 2008, vol. 5172 LNCS, pp. 9–32.
- [8] M. L. Brongersma and V. M. Shalaev, “The Case for Plasmonics,” *Science*, vol. 328, no. 5977, pp. 440–441, Apr. 2010.
- [9] M. L. Brongersma and V. M. Shalaev, “The case for plasmonics,” *Science*, vol. 328, no. 5977, pp. 440–441, 2010.
- [10] D. A. Genov, R. F. Oulton, G. Bartal, and X. Zhang, “Anomalous spectral scaling of light emission rates in low dimensional metallic nanostructures,” *Phys. Rev. B*, vol. 83, no. 24, pp. 1–7, 2011.

- [11] R. F. Oulton, V. J. Sorger, D. A. Genov, D. F. P. Pile, and X. Zhang, "A hybrid plasmonic waveguide for subwavelength confinement and long-range propagation," *Nat. Photonics*, vol. 2, no. 8, pp. 496–500, 2008.
- [12] K. F. MacDonald, Z. L. Sámson, M. I. Stockman, and N. I. Zheludev, "Ultrafast active plasmonics," *Nat. Photonics*, vol. 3, no. 1, pp. 55–58, 2009.
- [13] D. Pacifici, H. J. Lezec, and H. A. Atwater, "All-optical modulation by plasmonic excitation of CdSe quantum dots," *Nat. Photonics*, vol. 1, no. 7, pp. 402–406, 2007.
- [14] R. A. Pala, K. T. Shimizu, N. A. Melosh, and M. L. Brongersma, "A nonvolatile plasmonic switch employing photochromic molecules," *Nano Lett.*, vol. 8, no. 5, pp. 1506–1510, 2008.
- [15] Z. L. Sámson, K. F. MacDonald, and N. I. Zheludev, "Femtosecond active plasmonics: Ultrafast control of surface plasmon propagation," *J. Opt. Pure Appl. Opt.*, vol. 11, no. 11, 2009.
- [16] A. V. Krasavin, K. F. MacDonald, N. I. Zheludev, and A. V. Zayats, "High-contrast modulation of light with light by control of surface plasmon polariton wave coupling," *Appl. Phys. Lett.*, vol. 85, no. 16, pp. 3369–3371, 2004.
- [17] K. F. MacDonald, A. V. Krasavin, and N. I. Zheludev, "Optical modulation of surface plasmon-polariton coupling in a gallium/ aluminum composite," *Opt. Commun.*, vol. 278, no. 1, pp. 207–210, 2007.
- [18] Z. L. Sámson, S. C. Yen, K. F. MacDonald, K. Knight, S. Li, D. W. Hewak, D. Tsai, N. I. Zheludev, "Chalcogenide glasses in active plasmonics," *Phys. Status Solidi - Rapid Res. Lett.*, vol. 4, no. 10, pp. 274–276, 2010.
- [19] N. Rotenberg, M. Betz, and H. M. van Driel, "Ultrafast control of grating-assisted light coupling to surface plasmons," *Opt. Lett.*, vol. 33, no. 18, p. 2137, 2008.
- [20] X. Zhang, B. Sun, J. M. Hodgkiss, and R. H. Friend, "Tunable ultrafast optical switching via waveguided gold nanowires," *Adv. Mater.*, vol. 20, no. 23, pp. 4455–4459, 2008.
- [21] J. Dintinger, I. Robel, P. V. Kamat, C. Genet, and T. W. Ebbesen, "Terahertz all-optical molecule-plasmon modulation," *Adv. Mater.*, vol. 18, no. 13, pp. 1645–1648, 2006.
- [22] G. A. Wurtz, R. Pollard, and A. V. Zayats, "Optical bistability in nonlinear surface-plasmon polaritonic crystals," *Phys. Rev. Lett.*, vol. 97, no. 5, 2006.

- [23] M. Abb, P. Albella, J. Aizpurua, and O. L. Muskens, "All-optical control of a single plasmonic nanoantenna - ITO hybrid," *Nano Lett.*, vol. 11, no. 6, pp. 2457–2463, 2011.
- [24] J. Zhao, X. Zhang, C. R. Yonzon, A. J. Haes, and R. P. Van Duyne, "Localized surface plasmon resonance biosensors," *Nanomed.*, vol. 1, no. 2, pp. 219–228, 2006.
- [25] J. B. Pendry, "Negative refraction makes a perfect lens," *Phys. Rev. Lett.*, vol. 85, no. 18, pp. 3966–3969, 2000.
- [26] X. Zhang and Z. Liu, "Superlenses to overcome the diffraction limit," *Nat. Mater.*, vol. 7, no. 6, pp. 435–441, 2008.
- [27] S. Han, Y. Xiong, D. Genov, Z. Liu, G. Bartal, and X. Zhang, "Ray optics at a deep-subwavelength scale: A transformation optics approach," *Nano Lett.*, vol. 8, no. 12, pp. 4243–4247, 2008.
- [28] R.F. Oulton, V. J. Sorger, T. Zentgraf, R. M. Ma, C. Gladden, L. Dai, G. Bartal and X. Zhang, "Plasmon lasers at deep subwavelength scale," *Nature*, vol. 461, no. 7264, pp. 629–632, 2009.
- [29] J. Valentine, S. Zhang, T. Zentgraf, E. Ulin-Avila, D. A. Genov, G. Bartal and X. Zhang, "Three-dimensional optical metamaterial with a negative refractive index," *Nature*, vol. 455, no. 7211, pp. 376–379, 2008.
- [30] P. C. Mundru, V. Pappakrishnan, and D. A. Genov, "Material- and geometry-independent multishell cloaking device," *Phys. Rev. B - Condens. Matter Mater. Phys.*, vol. 85, no. 4, 2012.
- [31] S. Linic, P. Christopher, and D. B. Ingram, "Plasmonic-metal nanostructures for efficient conversion of solar to chemical energy," *Nat. Mater.*, vol. 10, no. 12, pp. 911–921, 2011.
- [32] H. A. Atwater and A. Polman, "Plasmonics for improved photovoltaic devices," *Nat. Mater.*, vol. 9, no. 3, pp. 205–213, 2010.
- [33] J. A. Schuller, E. S. Barnard, W. Cai, Y. C. Jun, J. S. White, and M. L. Brongersma, "Plasmonics for extreme light concentration and manipulation," *Nat. Mater.*, vol. 9, no. 3, pp. 193–204, 2010.
- [34] Y. Long, "Improving optical performance of inverted organic solar cells by microcavity effect," *Appl. Phys. Lett.*, vol. 95, no. 19, 2009.

- [35] B. P. Rand, P. Peumans, and S. R. Forrest, "Long-range absorption enhancement in organic tandem thin-film solar cells containing silver nanoclusters," *J App Phys*, vol. 96, no. 12, pp. 7519–7526, 2004.
- [36] A. Moreau, C. Ciraci, J. J. Mock, R.T. Hill, Q. Wang, B. J. Wiley, A. Chilkoti and D. R. Smith, "Controlled-reflectance surfaces with film-coupled colloidal nanoantennas," *Nature*, vol. 492, no. 7427, pp. 86–89, 2012.
- [37] M. K. Hedayati, M. Javaherirahim, B. Mozooni, R. Abdelaziz A. Tavassolizadeh, V. S. K. Chakravadhanula, V. Zaporajtchenko, T.Strunkus, F. Faupel, and M. Elbahri, "Design of a perfect black absorber at visible frequencies using plasmonic metamaterials," *Adv. Mater.*, vol. 23, no. 45, pp. 5410–5414, 2011.
- [38] D. Wang, W. Zhu, M. D. Best, J. P. Camden, and K. B. Crozier, "Wafer-scale metasurface for total power absorption, local field enhancement and single-molecule Raman spectroscopy," *Sci. Rep.*, vol. 3, 2013.
- [39] J. Grandidier, D. M. Callahan, J. N. Munday, and H. A. Atwater, "Light absorption enhancement in thin-film solar cells using whispering gallery modes in dielectric nanospheres," *Adv. Mater.*, vol. 23, no. 10, pp. 1272–1276, 2011.
- [40] G. Kang, H. Park, D. Shin, S. Baek, M. Choi, D. H. Yu, K. Kim, and W. J. Padilla, "Broadband light-trapping enhancement in an ultrathin film a-si absorber using whispering gallery modes and guided wave modes with dielectric surface-textured structures," *Adv. Mater.*, vol. 25, no. 18, pp. 2617–2623, 2013.
- [41] Z. Liu, P. Zhan, J. Chen, C. Tang, Z. Yan, Z. Chen, and Z. Wang, "Dual-broadband near-infrared perfect absorber based on a hybrid plasmonic-photonic microstructure," *Opt. Express*, vol. 21, no. 3, p. 3021, 2013.
- [42] C. Y. Yap, C. Y. Chua, C. K. Dong, Z. L. Zhang, and D. Q. Loh, "Review of selective laser melting: Materials and applications," *Appl. Phys. Rev.*, vol. 2, no. 4, 2015.
- [43] Roland Berger Strategy Consultants, "Additive manufacturing – a game changer for the manufacturing industry?," *Munich Ger.*, 2013.
- [44] I. Gibson, D. Rosen, and B. Stucker, *Additive Manufacturing Technologies*. 2015.
- [45] L. Thijs, F. Verhaeghe, T. Craeghs, J. V. Humbeeck, and J. P. Kruth, "A study of the microstructural evolution during selective laser melting of Ti-6Al-4V," *Acta Mater.*, vol. 58, no. 9, pp. 3303–3312, 2010.

- [46] M. Garibaldi, I. Ashcroft, M. Simonelli, and R. Hague, "Metallurgy of high-silicon steel parts produced using Selective Laser Melting," *Acta Mater.*, vol. 110, pp. 207–216, 2016.
- [47] C. L. Ventola, "Medical Applications for 3D Printing: Current and Projected Uses.," *P T Peer-Rev. J. Formul. Manag.*, vol. 39, no. 10, pp. 704–711, 2014.
- [48] A. V. Krasavin and A. V. Zayats, "Electro-optic switching element for dielectric-loaded surface plasmon polariton waveguides," *Appl. Phys. Lett.*, vol. 97, no. 4, 2010.
- [49] J. Chen, Z. Li, X. Zhang, J. Xiao, and Q. Gong, "Submicron bidirectional all-optical plasmonic switches," *Sci. Rep.*, vol. 3, 2013.
- [50] G. Veronis, Z. Y. Zongfu Yu, S. E. K. Sükri Ekin Kocabas, D. A. B. M. David A. B. Miller, M. L. B. Mark L. Brongersma, and S. F. Shanhui Fan, "Metal-dielectric-metal plasmonic waveguide devices for manipulating light at the nanoscale," *Chin. Opt. Lett.*, vol. 7, no. 4, pp. 302–308, 2009.
- [51] J. A. Dionne, K. Diest, L. A. Sweatlock, and H. A. Atwater, "PlasMOStor: A metal-oxide-si field effect plasmonic modulator," *Nano Lett.*, vol. 9, no. 2, pp. 897–902, 2009.
- [52] A. E. Nikolaenko, N. Papasimakis, A. Chipouline, F. De Angelis, E. Di Fabrizio, and N. I. Zheludev, "THz bandwidth optical switching with carbon nanotube metamaterial," *Opt. Express*, vol. 20, no. 6, p. 6068, 2012.
- [53] A. L. Lereu, A. Passian, J. P. Goudonnet, T. Thundat, and T. L. Ferrell, "Optical modulation processes in thin films based on thermal effects of surface plasmons," *Appl. Phys. Lett.*, vol. 86, no. 15, pp. 1–3, 2005.
- [54] A. Passian, A. L. Lereu, E. T. Arakawa, A. Wig, T. Thundat, and T. L. Ferrell, *Modulation of multiple photon energies by use of surface plasmons.*, vol. 30, 2005.
- [55] A. Passian, A. L. Lereu, E. T. Arakawa, R. H. Ritchie, T. Thundat, and T. L. Ferrell, "Opto-electronic versus electro-optic modulation," *Appl. Phys. Lett.*, vol. 85, no. 14, pp. 2703–2705, 2004.
- [56] S. Bremen, D. Buchbinder, W. Meiners, and K. Wissenbach, "Mit Selective Laser Melting auf dem Weg zur Serienproduktion?," *Rapid Manuf.*, no. 6, pp. 24–28, 2011.
- [57] D. Buchbinder, H. Schleifenbaum, S. Heidrich, W. Meiners, and J. Bültmann, "High power Selective Laser Melting (HP SLM) of aluminum parts," in *Physics Procedia*, 2011, vol. 12, no. PART 1, pp. 271–278.

- [58] “<https://3dprinting.co.uk/news/hull-core-building-strategy/>.” .
- [59] N. K. Tolochko, T. Laoui, Y. V. Khlopkov, S. E. Mozzharov, V. I. Titov, and M. B. Ignatiev, “Absorptance of powder materials suitable for laser sintering,” *Rapid Prototyp. J.*, vol. 6, no. 3, pp. 155–160, 2000.
- [60] P. Fischer, V. Romano, H. P. Weber, N. P. Karapatis, E. Boillat, and R. Glardon, “Sintering of commercially pure titanium powder with an Nd:YAG laser source,” *Acta Mater.*, vol. 51, no. 6, pp. 1651–1662, 2003.
- [61] A. V. Gusarov, I. Yadroitsev, P. Bertrand, and I. Smurov, “Model of Radiation and Heat Transfer in Laser-Powder Interaction Zone at Selective Laser Melting,” *J. Heat Transf.*, vol. 131, no. 7, p. 072101, 2009.
- [62] C. D. Boley, S. C. Mitchell, A. M. Rubenchik, and S. S. Q. Wu, “Metal powder absorptivity: modeling and experiment,” *Appl. Opt.*, vol. 55, no. 23, p. 6496, 2016.
- [63] K. Kamiuto, “Radiative transfer through a randomly-packed bed of spheres,” *J. Quant. Spectrosc. Radiat. Transf.*, vol. 41, no. 1, pp. 23–27, 1989.
- [64] C. D. Boley, S. A. Khairallah, and A. M. Rubenchik, “Calculation of laser absorption by metal powders in additive manufacturing,” *Appl. Opt.*, vol. 54, no. 9, p. 2477, 2015.
- [65] A. V. Gusarov and J. P. Kruth, “Modelling of radiation transfer in metallic powders at laser treatment,” *Int. J. Heat Mass Transf.*, vol. 48, no. 16, pp. 3423–3434, 2005.
- [66] X. C. Wang, T. Laoui, J. Bonse, J. P. Kruth, B. Lauwers, and L. Froyen, “Direct selective laser sintering of hard metal powders: Experimental study and simulation,” *Int. J. Adv. Manuf. Technol.*, vol. 19, no. 5, pp. 351–357, 2002.
- [67] C. Argento and D. Bouvard, “A ray tracing method for evaluating the radiative heat transfer in porous media,” *Int. J. Heat Mass Transf.*, vol. 39, no. 15, pp. 3175–3180, 1996.
- [68] G. Baffou and H. Rigneault, “Femtosecond-pulsed optical heating of gold nanoparticles,” *Phys. Rev. B*, vol. 84, no. 3, p. 035415, Jul. 2011.
- [69] A. V. Zayats, I. I. Smolyaninov, and A. A. Maradudin, “Nano-optics of surface plasmon polaritons,” *Phys. Rep.*, vol. 408, no. 3–4, pp. 131–314, 2005.
- [70] W. L. Barnes, A. Dereux, and T. W. Ebbesen, “Surface plasmon subwavelength optics,” *Nature*, vol. 424, no. 6950, pp. 824–830, 2003.

- [71] E. Hutter and J. H. Fendler, "Exploitation of localized surface plasmon resonance," *Adv. Mater.*, vol. 16, no. 19, pp. 1685–1706, 2004.
- [72] S. Hayashi and T. Okamoto, "Plasmonics: Visit the past to know the future," *J. Phys. Appl. Phys.*, vol. 45, no. 43, 2012.
- [73] Rayleigh L, "On the scattering of light by small particles," *Philos Mag*, vol. 41, pp. 447–454, 1871.
- [74] Mie G., "Beitra"ge zur optik tru"ber medien, speziell kolloidaler metallo"sungen," *Ann Phys*, vol. 330, pp. 377–445, 1908.
- [75] A. Sommerfeld, "Uber die Ausbreitnng der Wellen in der Drahtlosen Telegraohie," *Ann. Phys.*, vol. 333, no. 4, pp. 665–736, 1909.
- [76] S. A. Maier, *Plasmonics: Fundamentals and applications*. 2007.
- [77] R. H. Ritchie, "Plasma Losses by Fast Electrons in Thin Films," *Phys. Rev.*, vol. 106, no. 5, p. 874, 1957.
- [78] C. J. Powell and J. B. Swan, "Origin of the Characteristic Electron Energy Losses in Magnesium," *Phys. Rev.*, vol. 116, no. 1, pp. 81–83, Oct. 1959.
- [79] D. A. Genov, M. Ambati, and X. Zhang, "Surface Plasmon Amplification in Planar Metal Films," *IEEE J. Quantum Electron.*, vol. 43, no. 11, pp. 1104–1108, Nov. 2007.
- [80] "Optical Properties of Solids | Mark Fox | 9780199573370 | Oxford University Press Canada." <http://www.oupcanada.com/catalog/9780199573370.html>. [Accessed: 06-Sep-2018].
- [81] "Surface Plasmons on Smooth and Rough Surfaces and on Gratings | Heinz Raether | Springer." <https://www.springer.com/us/book/9783662151242>. [Accessed: 06-Sep-2018].
- [82] E. J. Zeman and G. C. Schatz, "An accurate electromagnetic theory study of surface enhancement factors for silver, gold, copper, lithium, sodium, aluminum, gallium, indium, zinc, and cadmium," *J. Phys. Chem.*, vol. 91, no. 3, pp. 634–643, Jan. 1987.
- [83] S. Kasap and P. Capper, *Springer Handbook of Electronic and Photonic Materials*, vol. 10. 2006.
- [84] B. V. V. Zeghbroeck, *Principles of Semiconductor Devices and Heterojunctions*, 1 edition. Upper Saddle River, N.J.; London: Prentice Hall, 2010.

- [85] R. J. Nicholas, J. C. Portal, C. Houlbert, P. Perrier, and T. P. Pearsall, "An experimental determination of the effective masses for  $Ga_xIn_{1-x}As_yP_{1-y}$  alloys grown on InP," *Appl. Phys. Lett.*, vol. 34, no. 8, pp. 492–494, Apr. 1979.
- [86] M. Sotoodeh, A. H. Khalid and A. A. Rezazadeh, "Empirical low-field mobility model for III–V compounds applicable in device simulation codes," *Journal of Applied Physics.*, vol. 87, pp. 2890, 2000.
- [87] D. M. Caughey and R. E. Thomas, "Carrier mobilities in silicon empirically related to doping and field," *Proc. IEEE*, vol. 55, no. 12, pp. 2192–2193, Dec. 1967.
- [88] S. Tiwari and S. L. Wright, "Material properties of p-type GaAs at large dopings," *Appl. Phys. Lett.*, vol. 56, no. 6, pp. 563–565, 1990.
- [89] J. A. Dionne, L. A. Sweatlock, H. A. Atwater, and A. Polman, "Plasmon slot waveguides: Towards chip-scale propagation with subwavelength scale localization," *Phys. Rev. B*, vol. 73, no. 3, p. 035407, Jan. 2006.
- [90] G. Veronis and S. Fan, "Guided subwavelength plasmonic mode supported by a slot in a thin metal film," *Opt. Lett.*, vol. 30, no. 24, pp. 3359–3361, Dec. 2005.
- [91] X. Y. He, Q. J. Wang, and S. F. Yu, "Analysis of dielectric-loaded surface plasmon waveguide structures: Transfer matrix method for plasmonic devices," *J. Appl. Phys.*, vol. 111, no. 7, p. 073108, Apr. 2012.
- [92] V. M. Shalaev, "Optical negative-index metamaterials," *Nat. Photonics*, vol. 1, no. 1, pp. 41–48, Jan. 2007.
- [93] J. B. Pendry, A. J. Holden, D. J. Robbins, and W. J. Stewart, "Magnetism from conductors and enhanced nonlinear phenomena," *IEEE Trans. Microw. Theory Tech.*, vol. 47, no. 11, pp. 2075–2084, Nov. 1999.
- [94] S. Linden, C. Enkrich, G. Dolling, M. W. Klein and J. Zhou, "Photonic Metamaterials: Magnetism at Optical Frequencies," *IEEE Journal of Selected Topics in Quantum Electronics*, vol.12, 2006.
- [95] V. G. Veselago, "The Electrodynamics of substances with simultaneously negative values of  $\epsilon$  and  $\mu$ ," *Sov. Phys. Uspekhi*, vol. 10, no. 4, p. 509, 1968.
- [96] E. Kretschmann and H. Raether, "Notizen: Radiative Decay of Non-Radiative Surface Plasmons Excited by Light," *Z. Für Naturforschung A*, vol. 23, no. 12, pp. 2135–2136, 2014.

- [97] A. Otto, "Excitation of nonradiative surface plasma waves in silver by the method of frustrated total reflection," *Z. Für Phys. Hadrons Nucl.*, vol. 216, no. 4, pp. 398–410, Aug. 1968.
- [98] W. L. Bond, B. G. Cohen, R. C. C. Leite, and A. Yariv, "Observation of the dielectric-waveguide mode of light propagation in p-n junctions," *Appl. Phys. Lett.*, vol. 2, no. 3, pp. 57–59, 1963.
- [99] S. M. Sze and K. K. Ng, *Physics of Semiconductor Devices*. 2007.
- [100] D. J. Griffiths, "Introduction to Quantum Mechanics," *Introd. Quantum Mech.*, vol. 2, pp. 147–152, 2004.
- [101] J. K. Luo, H. Thomas, D. V. Morgan, D. Westwood, and R. H. Williams, "The electrical breakdown properties of GaAs layers grown by molecular beam epitaxy at low temperature," *Semicond. Sci. Technol.*, vol. 9, no. 12, pp. 2199–2204, 1994.
- [102] B. S. Williams, "Terahertz quantum-cascade lasers," *Nat. Photonics*, vol. 1, no. 9, pp. 517–525, 2007.
- [103] T. Orzali, A. Vert, R. T. P. Lee, A. Norvilas, G. Huang, J. L. Herman, R. J. W. Hill, and S. S. PapaRao, "Heavily tellurium doped n-type InGaAs grown by MOCVD on 300 mm Si wafers," *J. Cryst. Growth*, vol. 426, pp. 234–247, 2015.
- [104] M. J. R. Heck, J. F. Bauters, M. L. Davenport, J. K. Doylend, S. Jain, G. Kurczveil, S. Srinivasan, Y. Tang, and J. E. Bowers., "Hybrid Silicon Photonic Integrated Circuit Technology," *IEEE J. Sel. Top. Quantum Electron.*, vol. 19, no. 4, pp. 6100117–6100117, Jul. 2013.
- [105] Q. Xu and R. Soref, "Reconfigurable optical directed-logic circuits using microresonator-based optical switches," *Opt. Express*, vol. 19, no. 6, p. 5244, 2011.
- [106] L. Zhang, J. Ding, Y. Tian, R. Ji, L. Yang, H. Chen, P. Zhou, Y. Lu, W. Zhu, and R. Min, "Electro-optic directed logic circuit based on microring resonators for XOR/XNOR operations," *Opt. Express*, vol. 20, no. 11, p. 11605, 2012.
- [107] R. F. Oulton, V. J. Sorger, T. Zentgraf, R. M. Ma, C. Gladden, L. Dai, G. Bartal and X. Zhang, "Plasmon lasers at deep subwavelength scale," *Nature*, vol. 461, no. 7264, pp. 629–632, 2009.
- [108] B. Lahiri, R. Dylewicz, R. M. De La Rue, and N. P. Johnson, "Impact of titanium adhesion layers on the response of arrays of metallic split-ring resonators (SRRs).," *Opt. Express*, vol. 18, no. 11, pp. 11202–11208, 2010.

- [109] W. Zhang, Q. Li, and M. Qiu, “A plasmon ruler based on nanoscale photothermal effect,” *Opt. Express*, vol. 21, no. 1, p. 172, 2013.
- [110] A. Hatef and M. Meunier, “Plasma-mediated photothermal effects in ultrafast laser irradiation of gold nanoparticle dimers in water,” *Opt. Express*, vol. 23, no. 3, p. 1967, 2015.
- [111] C. F. Bohren and D. R. Huffman, *Absorption and Scattering of Light by Small Particles*. 1998.
- [112] “<https://www.concept-laser.de/en/products/machines/mlab-cusing.html>.” .
- [113] P. Johnson and R. Christy, “Optical constants of transition metals: Ti, V, Cr, Mn, Fe, Co, Ni, and Pd,” *Phys. Rev. B*, vol. 9, no. 12, pp. 5056–5070, 1974.
- [114] P. Johnson and R. Christy, “<http://www.rsc.org/periodic-table/element/22/titanium>.”
- [115] “<http://imprimalia3d.com/services/slm-50>.”
- [116] E. S. Harmon, M. L. Lovejoy, M. R. Melloch, M. S. Lundstrom, D. Ritter, and R. a. Hamm, “Minority-carrier mobility enhancement in p+ InGaAs lattice matched to InP,” *Appl. Phys. Lett.*, vol. 63, no. 5, pp. 636–638, 1993.
- [117] S. E. Swirhun, Y.-Kwark, and R. M. Swanson, “Measurement of electron lifetime, electron mobility and band-gap narrowing in heavily doped p-type silicon,” in *1986 International Electron Devices Meeting*, 1986, pp. 24–27.
- [118] X. Liu, Q. Tang, T. I. Kamins, and J. S. Harris, “Heavy arsenic doping of silicon by molecular beam epitaxy,” in *MBE 2002 - 2002 12th International Conference on Molecular Beam Epitaxy*, 2002, pp. 49–50.
- [119] T. Orzali, A. Vert, R.T.P. Lee, A. Norvilas, G. Huang, J. L. Herman, R. J. W. Hill, and S. S. PapaRao., “Heavily tellurium doped n-type InGaAs grown by MOCVD on 300 mm Si wafers,” *J. Cryst. Growth*, vol. 426, pp. 234–247, 2015.f
- [120] R. K. Vinnakota and D. A. Genov, “Terahertz optoelectronics with surface plasmon polariton diode,” *Sci. Rep.*, vol. 4, 2014.
- [121] R. K. Vinnakota and D. A. Genov, “Terahertz Optoelectronic Switching with Surface Plasmon Polariton Diode,” in *Conference on Lasers and Electro-Optics (2016), paper FTh1B.4*, 2016, p. FTh1B.4.
- [122] R. K. Vinnakota and D. A. Genov, “Self-consistent modeling of laser-matter interactions in the laser-based 3D printing of metals & alloys,” in *Conference on Lasers and Electro-Optics (2017), paper STh3J.5*, 2017, p. STh3J.5.

- [123] M. H. Alsaleh, R. K. Vinnakota, and D. A. Genov, "Saturation of Diamagnetic Response at THz Frequencies for Parallel Slabs Metamaterials," in *Advanced Photonics 2017 (IPR, NOMA, Sensors, Networks, SPPCom, PS) (2017)*, paper NoM2C.6, 2017, p. NoM2C.6.
- [124] R. K. Vinnakota, M. H. Alsaleh, and D. A. Genov, "Self-consistent electro-optical Modeling of light-matter interactions at the interface of InAs PN+-junction," in *Advanced Photonics 2017 (IPR, NOMA, Sensors, Networks, SPPCom, PS) (2017)*, paper ITh2C.2, 2017, p. ITh2C.2.
- [125] "Magnetic response of parallel slabs metamaterials at THz frequencies." [Online]. Available: <https://www.spiedigitallibrary.org/conference-proceedings-of-spie/10345/2272938/Magnetic-responsse-of-parallel-slabs-metamaterials-at-THz-frequencies/10.1117/12.2272938.short?SSO=1>. [Accessed: 13-Sep-2018].
- [126] R. K. Vinnakota and D. A. Genov, "Active Control of Charge Density Waves at Degenerate Semiconductor Interfaces," *Sci. Rep.*, vol. 7, no. 1, 2017.
- [127] R. K. Vinnakota, Liam Springer, & D. A. Genov, "Model of radiation and heat transfer in laser-matter interactions pertaining to Selective Laser Melting" Proceedings of Louisiana EPSCoR RII CIMM 2017.
- [128] R. K. Vinnakota, C. E. Maher, & D. A. Genov, "Self-consistent modeling of laser-matter interactions pertaining to laser-based 3D printing of metals & alloys". Proceedings of Louisiana EPSCoR RII CIMM 2016.